Failure of impulsively loaded thin-walled pipes and plates

Dario Schiano Moriello

A dissertation submitted in partial fulfillment

of the requirements for the degree of

Doctor of Philosophy

of

University College London.

Department of Mechanical Engineering

University College London

July 11, 2021

The Investigation which is the subject of this Thesis was carried out under the terms of QinetiQ Agreement No: 1804.

I, Dario Schiano Moriello, confirm that the work presented in this thesis is my own. Where information has been derived from other sources, I confirm that this has been indicated in the work.

Abstract

The capability to predict the modes of deformation of thin-walled structures is a paramount safety concern in military, civil and industrial environments. Finite element analysis offers a valid, cost-effective alternative to experimental programs when performing preliminary safety studies. This thesis investigates numerical procedures to study two typical safety-related problems of impulsively loaded thin-walled structures.

When a pressurised pipe experiences a guillotine break, the sudden fluid release causes a rapid whip-like motion, with possible damage to nearby structures. An element code is here developed to predict the pipe flexural and torsional behaviour, which adopts a corotational kinematic formulation for delivering reliable results at a fraction of the computational cost of conventional FEA techniques. The validated code, implemented with commercial FEA software, is employed in parametric studies leading to the discovery of new dimensionless groups that completely characterise the flexural behaviour of pipes. With the newfound understanding, simple empirical laws are established that predict the pipe response and the hazard conditions.

A shell element numerical model is built to study the rupture mechanisms of steel plates subjected to impulsive blast loadings. Tensile and shear experiments on steel specimens were performed to characterise the parameters of a triaxiality-dependent failure criterion, obtaining a mesh-size independent fracture model. The numerical predictions allowed to establish a novel phenomenological criterion, providing an answer to the previously unsolved question on the transition between different types of failure modes. Dimensionless failure maps are developed that

elucidate the influence of plate topology and boundary conditions on the rupture mechanisms. The study highlights the similarities in the response between simply-supported plates, and fully-clamped plates exposed to localised blast loadings. A new failure mode is discovered for simply-supported rectangular plates, where, under certain loading conditions, rupture propagates in the central area of the plate, rather than along the support.

Impact Statement

Thin-walled plates and pipes are ubiquitous structural elements. Thanks to their workability and light weight they offer manifold fields of applications, from simple containers to large scale structures, both in stationary and moving components. However, the high degree of deformability renders plates and pipes particularly susceptible to failure. Safety studies are therefore necessary to assess the conditions that can lead systems employing thin-walled elements to fail, or to ensure that the system is capable to withstand failure without catastrophic consequences.

Finite Element Analyses (FEA) are a fundamental tool for the safety assessment of thin-walled structures, thanks to their ease of implementation and relatively low cost, often replacing early experimental investigations, especially in the case of studies involving explosive or impulsive loadings, which could be particularly difficult to control and pose noteworthy safety concerns even in a controlled environment. However, conventional FE analyses often employ oversimplified constitutive models, severely limiting their reliability. Furthermore, leading-edge computing technologies, like recently developed real-time simulation engines, are often translated slowly to industrial level FEA, which usually requires noticeable computational costs, depending on the desired level of precision and the complexity of the system analysed. In light of these observations, FEA offers a great margin of improvement in terms of computing efficiency and modelling accuracy.

The scope of our work is to tackle the aforementioned issues, whilst solving two safety-related problems that are of interest to our industrial sponsor, working in the defence field, and that can benefit many engineering sectors: (i) the dynamic deformation of pipe whips, and (ii) the prediction of failure in metal plates hit by

explosive blasts. Following a literature survey of state-of-the-art modelling techniques, a beam element model was developed for the simulation of pipe whips, based on the corotational kinematic formulation, which is currently used in parallel research fields accomplishing fast-converging or even real-time numerical models. Comparing the results of pipe simulations employing 80 corotational beam elements to those obtained with a conventional FEA model employing up to 27360 shell elements, the corotational model proves to be up to 88 times faster than conventional FEA techniques whilst giving satisfactory results (in terms of displacement of the free end and localisation of cross-sectional collapse), and thanks to its ease of implementation it is readily applicable to industrial use. Studies employing the developed model have also shed new light on the flexural behaviour of pipes, identifying new dimensionless groups that completely characterise the physics of the problem. These discoveries have led to the establishment of simple empirical laws that successfully predict the pipe whip response and the hazard conditions, thus providing effective tools for the design of pipe systems.

Regarding the second problem of interest, fracture models that are independent of the characteristic element length are needed for the correct modelling of the fragmentation of plates exposed to blast loadings. This need has led to the establishment of a detailed yet straightforward procedure for the calibration of the model parameters which simultaneously minimises the demand for experimental testing. The plate model was used to develop a novel phenomenological criterion, based on the crack propagation velocity, to identify the transition between different failure modes. This study has also led to the discovery of new failure modes for simply-supported rectangular plates where, for high intensity blasts, the fracture mechanisms deviate from the preferred path along the supports, propagating towards the plate centre.

Notwithstanding the advancement made in this work and its importance in the investigation of thin-walled structures deforming dynamically, our research leaves many aspects worthy of further improvements, laying the foundations for future research. The models developed for pipes and plates have highlighted the areas wor-

thy of additional investigation, and further developments can be made to improve the predicting capability and reduce the computational cost.

Acknowledgements

I wish to acknowledge my supervisors, Dr Federico Bosi, Dr Ryo Torii and Dr P.J. Tan, for their unwearying support, constant presence and critical advice.This project would have not been possible without their contribution, both academic and financial. I also wish to acknowledge QinetiQ-UK and Mr Robert Balls for sponsoring my research.

Federico, despite joining our team on its last stage, your efforts have left the greatest mark of all, bringing true excellence to this research project. Under your wings, I have found new determination and proudly presented the results of my efforts to the world. Our lengthy conversations, in front of bright monitors or Italian pastries, will accompany me through all my future endeavours. I am thankful to Dr Simon Banks for hearing my call and for putting me in the right direction to complete this amazing journey.

To my colleagues, my friends. I wish I could thank all of you on these pages, one by one. But please rest assured, if you can't find your name here, it sits in a very special place in my heart of hearts. Anna (!), you have been there from the very beginning and held my hand through every step. Many friends come and go, but you are here to stay and I can't wait to see what our future holds. Jeremy, the little angel and devil that stand on my shoulders now and forever bear your face and wit and charme. John and Kae, conversing with the two of you has brought me so much joy. Thank you for introducing me to the glorious world of fine tea! Gaia, Francesca, Annamaria, Giorgia, my heartfelt thanks for being such great examples of strength and grace. Gaetano, you may have been my first true disciple, but your determination has made you so much more. To all the others, thank you

for believing in me.

Dear V, you have lend me your strength on the darkest day; Simon R, you have shown me that, after the night, a new sun shall rise.

Annalisa, my mirror, my sword and shield, words cannot describe my love and affection for you. I would not dare tread one more step without you by my side. Simone, Luca, Ilaria, destiny has bought us together, nothing will tear us apart.

Lastly, I want to thank my Parents and my Brother for their encouragement and for always being there, fighting the distance.

Vous, qui cherchez l'étoile...
Emmenez-moi loin d'ici.
Vous, les nouveaus poètes...
Ne partez pas sans moi.

Contents

List of Figures

List of Tables

Chapter 1

Background

1.1 Introduction

Accidents happen. Engineers follow safety measures in many steps of the structural design process, from concept design to the actual construction, to take into consideration the likelihood of accidents and their effect on the safety of the structure itself and of any neighbouring personnel or apparatus. Following established guidelines, preventive measures are introduced to control the operating conditions of a system, ensuring they fall within safe limits, but also to reduce the extent of damage when accidents occur.

Nevertheless, it is not always possible to prevent all form of accidents. For this reason, part of the design process involves detailed testing aimed at investigating the structural behaviour once failure has occurred. The most straightforward method of investigation consists of experimental studies attempting to reproduce accidental dynamics in a controlled environment. However, experimental investigations are generally time consuming and expensive, posing a limit to their practical application. Furthermore, even the experiment itself is susceptible to accidents, despite its careful planning, and for this reason, precise guidelines must be adopted to ensure the safety of the operators. A particularly hazardous experimental field is the investigation of impulsively loaded structures. Some of the aspects that are a common cause of concern for this type of experiments are: high-intensity loading, large deformations, component failure and fragmentation, and accidental impacts.

In the last two decades, recent advancements in computing technologies have led to the development of numerical techniques capable of modelling physical problems with incredible accuracy and continuously increasing processing speed. Thanks to the numerical advancement, FE analyses have become a valid alternative to elaborate and time consuming experiments, upon proper validation of the numerical model. Nowadays, many industries employ FEA in tandem with experimental testing in every phase of design, from early test plan to the final system certification.

FEA are particularly useful for the modelling of thin-walled structural elements. Characterised by their relatively light weight and high degree of deformability, thin-walled structures are employed in a wide range of engineering fields, their applications ranging from pressure vessels, vehicles, ships and pipelines to bridges, industrial building and offshore platforms. The present research work deals with the numerical analysis of two safety-related problems, usually encountered in the fields of defence, nuclear and industrial production, involving thin-walled structural components loaded impulsively: the inelastic deformation of pipe whips, and the failure mechanisms of metal plates loaded impulsively.

In the first problem of interest, an initially intact pipe that transports pressurised fluids starts to deform at high speed under the influence of an intense loading caused by the accidental release of the internal fluid. The pipe whip motion constitutes a serious hazard concern due to the likelihood of impact with nearby structures. A novel finite element code is here developed to predict the deformation of the pipe and its area of influence. The code consists of a beam element employing an opportunely developed constitutive law for the pipe flexural behaviour to correctly capture the cross-sectional collapse typical of pipes in bending. The element incorporates a corotational kinematic formulation to help reduce the computational cost. The model, validated against experimental data for thick and thin pipe whips available from the literature, is employed in parametric studies investigating the effect of the pipe dimensions and of the loading intensity on the deformation mechanism, predicting the extent of the area of influence in a wide range of geometrical and loading conditions. The study highlights the limitations of the currently available numeri-

cal and analytical models that are commonly used for predicting the behaviour of pipe whips, whilst demonstrating the applicability of the newly developed code for industrial applications.

In the second problem of interest, a monolithic plate made of steel undergoes large deformation and fragmentation due to the interaction with an intense blast loading generated by a nearby explosion. A shell-element model is here developed to analyse the modes of deformation of the plate and the evolution of fracture mechanisms when failure occurs. The model employs comprehensive triaxiality-dependent failure criteria to characterise the synergetic effect of ductile damage (due to void nucleation, growth and coalescence) and shear damage mechanisms (due to shear band localisation). Experimental tensile and shear tests are performed on mild steel specimens to calibrate the damage parameters and ensure mesh insensitivity of fracture. The shell-element model successfully predicts the failure mechanisms observed experimentally and is later employed in parametric studies investigating the influence of the plate topology, loading intensity and boundary conditions on the modes of failure. The data collected are used to establish dimensionless failure maps that offer an effective engineering tool for the prediction of the failure modes using readily available system parameters. Furthermore, the model identifies previously unobserved failure modes in the case of simply-supported rectangular plates, where cracks propagate in the central area of the plate, rather than along the support, laying the foundation of new experimental investigations.

The two case studies are closely linked by the following aspects: the physical processes involved, characterised by the large inelastic deformation of ductile thin-walled structural elements, the application in industrial, military and civil environments, the numerical solving methodologies adopted, and the production of dimensionless diagrams for the analysis of the numerical results. In both problems, finite element solution procedures are employed to investigate the deformation mechanisms. Special emphasis is put in implementing comprehensive material and structural models, validated against experimental evidence. When multiple approaches were available, the study opted for those that would be of greater interest

to the industry, researching a balance between accuracy, ease of implementation and reduced computational costs.

Despite the many similarities, the two studies present some differences. The analysis of pipe whips is interested in the post-failure deformation of pipes that have suffered a guillotine break. Our research work successfully delivers a finite element code that can be readily implemented into commercial FE software and applied in a variety of engineering applications of pipes. On the other side, the second study investigated the initiation and growth of fracture mechanisms in initially intact plates. The study concludes with the production of failure maps that, through the use of simple dimensionless numbers, provide a visual aid for the prediction of the modes of failure of plate elements by knowing its dimension and loading conditions.

1.2 Literature review

1.2.1 The flexural behaviour of pipe whips

The failure of pipes transporting high pressure fluids is a common safety issue encountered in chemical, nuclear and power plants. Although pipes are designed to withstand normal operating conditions, pipe failure may result from several factors, like pressure fluctuations, accidental damage or creep. In order to satisfy the safety requirement set by regulatory authorities, the safety-compliant design of a piping system must demonstrate the capability of the structure to withstand failure without catastrophic consequences.

The failure of a pipe due to a guillotine break is schematised in Figure 1.1. The sudden release of high pressure fluids from a broken section induces an intense blow-down force on the pipe, causing a rapid whip-like motion that constitutes potential hazard to nearby equipment [1]. To increase the safety of the system, pipe whip restraint devices are installed, which absorb the kinetic energy of the pipe before it damages neighbouring structures. Despite the improved safety, the installation of restraints can severely reduce the access to the system, thus compromising the performance of maintenance operations.

Aiming at optimising the number of restraints, the designers of piping systems have studied the pipe whip motion in detail [2, 3]. In the past, the R3 Impact Assessment Procedure [4, 5] and the code ANSI/ANS 58.8 [6] have been used to assess the hazards of pipe rupture. Baum [7] conducted an experimental investi-

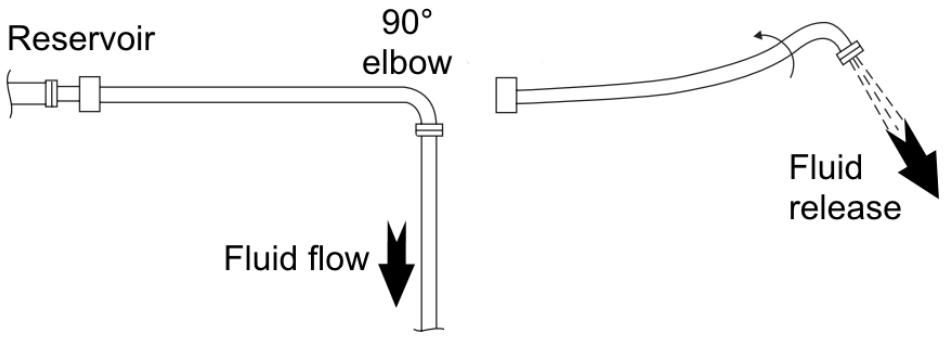

Figure 1.1: Guillotine break of pressurised pipes. Adapted from Lu and Yu [1].

gation on steel pipes to understand the influence of pipeline geometry and fluid pressure on in-plane pipe whips. The geometries investigated, illustrated in Figure 1.2, were initially straight cantilever pipes with an elbow bend at the free end (where the fluid escapes) and cantilever pipes with multiple bends. Baum [7] found that the maximum deformation is obtained when the bend at the free end has a 90° angle, and that the pipe behaviour is determined by a single dimensionless group, $\phi = PAL/M_P$ (where P is the fluid pressure, A the cross-sectional area, and M_P the plastic moment). In the case of straight pipes, L corresponds to the length of the pipe, whereas, for a bent pipe, $L = \sum_{i=1}^{n} L_i$ is a function of time, with L_i being the length of the members of the pipe involved in the motion (see Figure 1.2). For each experiment, the study measured the hazard zone Z, which is the extent of the area of influence of the pipe. It was found that when $\phi \leq 4.6$, the centre of the pipe rotation lies at the fixed end, and the hazard zone reaches its maximum extent, $Z = L$. Otherwise, when $\phi > 4.6$, collapse mechanisms affect the pipe, and the centre of rotation moves to a point along the pipe, reducing the extent hazard zone ($Z < L$).

Stronge and Yu [8] developed a theoretical model for predicting the point of collapse of slender structures in bending, later applied to the analysis of in-plane pipe whips [9, 10]. The study, based on the theory of rigid-perfectly plastic structures, treats the pipe as a rigid beam rotating about a plastic hinge. Solving the equation of motion of the beam, the theoretical model identifies a lower limit value

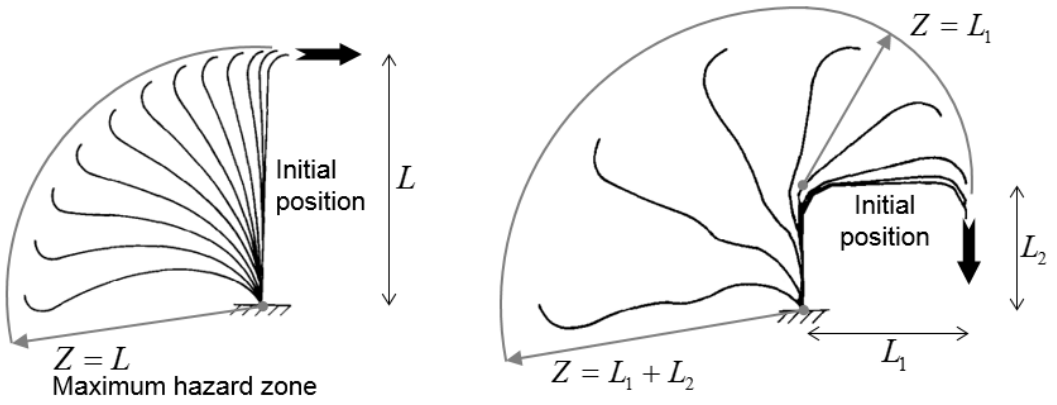

Figure 1.2: Deformation mechanisms of pipe whips and maximum extent of the hazard zone, Z. Geometries of an initially straight pipe (left) and of a pipe with multiple bends (right). Adapted from [7].

for the dimensionless group, $\phi = 3$ [8], below which the pipe is stationary. Additionally, the model predicts with satisfying accuracy the hazard zone of pipe whips when the mass of the bend is negligible. However, when the mass is significant, the model grossly underestimates the hinge position and does not predict the pipe motion with accuracy. Subsequent upgrades to the model were made to include elastic and strain-hardening effects, improving the prediction of the pipe motion [2].

Following the advancements of computing technology in the last two decades, numerical models have been developed to analyse the deformation of pipe whips. Reid et al. [2] developed a finite difference model for in-plane pipe whips, employing non-linear constitutive laws that simulate metal plasticity and the bending behaviour of pipes. The model predicted with accuracy the deformation mechanism and the development of plastic hinges in the case of relatively thick pipes, but was less successful in the case of thin pipes, when the deformation is dominated by the collapse of the cross-section.

Finite element analyses offer a valid alternative for the simulation of pipe whips [11, 12]. Reid et al. [11, 13] employed a shell element model to assess the deformation of out-of-plane pipe whips. In the case studied, an initially bent pipe undergoes large deformation, rotation and twisting in space under the influence of an out-of-plane force. Employing shell elements constitutes a straightforward approach to the analysis of pipe whips. Discretising the cross-section with shells allows to model the collapse and predict the hazard zone with satisfying accuracy [13], at the expense of long computational times, due to the need of a sufficiently refined mesh. Micheli and Zanaboni [12] employed simulations of pipe whips using pipe elements to obtain conservative predictions of the whip motion. Although the makes several simplifying assumptions, neglecting cross-sectional ovalization and assuming a bilinear kinematic hardening material behaviour, calculations of the kinetic energy based on the numerical predictions are useful for the design of restraint devices.

Theoretical models have been proposed to analyse three-dimensional pipe whips [14, 15]. Based on the same rigid, perfectly plastic approach of the 2D case

[9, 10], the study determined new limit values for the dimensionless group ϕ that delimit several deformation mechanisms. Depending on the loading intensity and the length of each member of the pipe, torsion and bending concur in the development of multiple plastic hinges along the pipes or at the bend. However, the theoretical model requires numerical solutions to evaluate the hinge position.

Recently, commercial finite element software have developed special structural elements suitable for the simulation of pipe whips. For example, pipe elements (sometimes referred to as elbow elements [16]) are capable of modelling the collapse of pipes subjected to internal and external pressures [17], and beam-general-section elements can reproduce the non-linear moment-curvature relation of pipes in bending [16]. The two element types have limited applicabilities; the former can only be used for the prediction of pipe collapse in static analyses, and have demonstrated little reliability [17], showing significant discrepancies in terms of ovalization modes and stress distribution around the pipe section compared to results obtained with shell elements, while the latter element type gives unrealistic results when modelling the collapse of thin pipes [16], displaying excessive collapse.

Inspired by the aforementioned research, and to overcome the limitations of the currently available elements, a novel beam element is here developed for modelling thin pipes undergoing in-plane and out-of-plane deformations. Similarly to the method presented by Reid et al. [2], the element employs an elastoplastic hardening-softening constitutive model for bending, predicting with great accuracy the pipe deformation, the hazard zone and the development of plastic hinges. The model has a significantly reduced computational cost, compared to shell element analyses, thanks to the use of the corotational formulation.

Reid et al. [2, 18] and Jialing and Reid [19] performed several bending experiments to characterise the flexural behaviour of steel pipes with varying thickness. When a cylindrical tube undergoes large bending, the large plastic deformation of the tubes causes the ovalization of the initially circular cross-section, eventually leading to structural collapse, in a phenomenon named Brazier effect [20]. The

typical structural response, expressed in the form of a moment-curvature relation, is illustrated in Figure 1.3. Following an initial linear-elastic stage, relatively thick tubes display a hardening-softening relation. The behaviour derives from the combination of two opposing mechanisms of strain and ovalization, which increase or reduce the load-carrying capacity of the member, respectively. Comparing the moment-curvature relations obtained experimentally for several pipes of varying thickness, Reid et al. [18] observed that the critical value of curvature at the onset of the softening stage is determined by the wall-thickness, H, and the mean cross-sectional radius, R, through the formula

$$k_c = C\frac{H}{R^2} \tag{1.1}$$

where $C = 0.2$–0.5 is a constant that depends on the material and the R/H ratio. Following the experimental observation, a theoretical analysis was proposed, based on the plastic shell theory [2, 21], to predict the moment-curvature behaviour. It was observed that the theoretical model could only be solved approximately with a numerical approach, concluding that experimental tests or numerical simulations must be carried out case-by-case to obtain the moment-curvature relationship for

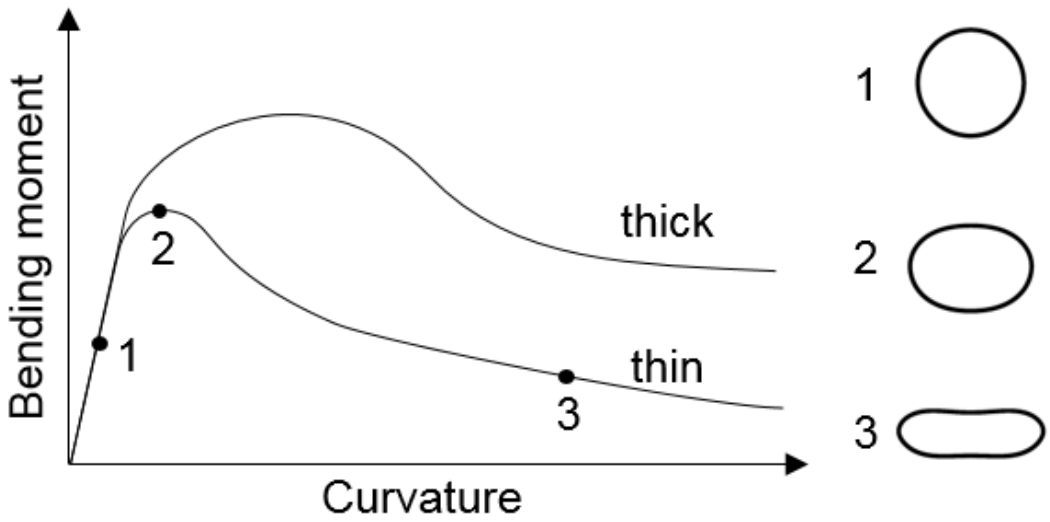

Figure 1.3: Typical flexural behaviour of pipes obtained from bending tests. Different moment-curvature relations observed for thick and thin pipes (left). Progressive collapse of the cross-section in bending (right).

specific combinations of R and H.

In the present work, moment-curvature relations for thick and thin pipe were generated using finite element analysis. The curves, validated against the experimental data from [2] were applied as constitutive models in the corotational element code here developed for the simulation of pipe whips. Comparing the relations obtained from pipes with different combination of R and H, three dimensionless group were identified that characterise the values of curvature and moment at the onset of softening and allow to completely characterise the moment-curvature relations of thick and thin pipes.

1.2.2 The corotational framework

There exists a significant body of literature on the theory of the corotational (CR) formulation, the term being first introduced in 1960 (often spelled co-rotational) in the field of continuum mechanics. The concept of the decomposition of motion into a rigid-body and a pure deformational parts can be traced back to Cauchy and Biot in the years 1827 and 1930, respectively, in the theory of continuum mechanics, but only after World War II the idea received its first technological application, in the field of aerospace industry, for the kinematic analysis of an entire aeroplane structure [22].

The application of the CR framework to the kinematic description of finite element is illustrated in Figure 1.4, where the separation of rigid body motion and deformation is obtained through the introduction of a reference frame that follows the rigid rotation of each element. Therefore, in the CR formulation there are three reference frames, or configurations [22]:

1. The *base configuration*, C^0, fixed at the beginning of the analysis and shared by all the elements in the model. It serves as the basis for the definition of the nodal coordinates and as the origin of all displacements. It takes the name *initial* configuration when it coincides with the original position, and *undeformed* when the body is at rest in its initial state;

2. The *corotated configuration*, C^R, that is unique for each element, obtained

through the rigid body motion of the element from its initial position;

3. The *deformed configurations*, C^D, one for each element node, used to compute the deformation of the element.

One of the first CR finite element models is attributed to Belytschko and Hsieh [23], who developed beam and triangular shell elements for transient small-strain analyses, employing a bi-linear elastoplastic material model. They noted that evaluating the strains in the deformed frame greatly simplified the governing equations for the computation of local forces, resulting in a significant advantage in computational speed [23]. Later on, Belytschko and Glaum [24] developed a higher order CR element for analyses with moderate rotations. The new formulation required only a slightly larger computational cost for each element, but was capable of converging to the exact solution more rapidly, as the mesh is refined, compared to its lower order equivalent. However, the authors commented that, in instances where a large number of elements is required, the difference in results between the two formulations becomes less significant, thus reducing the advantage of using higher order elements [24].

Crisfield [25] observed that most of the previously-developed CR elements

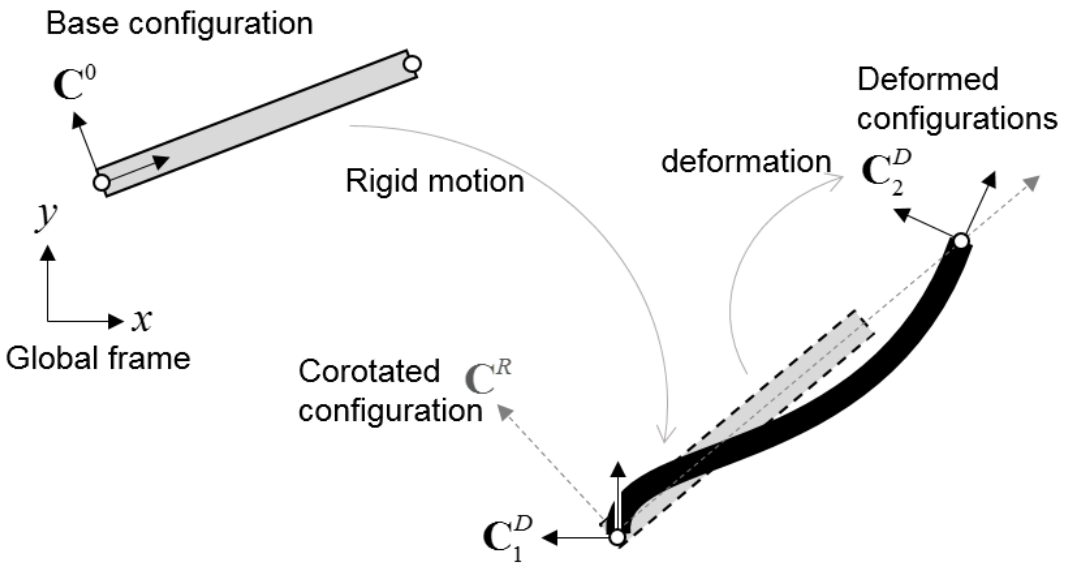

Figure 1.4: Application of the corotational framework to finite elements.

applied the correct transformation to the force vector whilst making simplifying assumptions in the rotation of the stiffness matrix, leading to convergence issues, especially in the case of buckling analysis. He then proceeded to develop a consistent CR formulation for beam [25], shell and solid elements [26], where the stiffness matrix transformation is consistent with that applied to the force vector. Battini [27] and Battini and Pacoste [28] have expanded the work of Crisfield and Moita [26] developing consistent elastic [27] and elastoplastic [28] beam elements with warping effects for the analysis of beams with open cross-sections in instability problems.

Felippa and Haugen [22] framed a unified small-strain theory for CR elements in static analyses, noting that, depending on its exact expression, a consistent stiffness matrix might also be equilibrated —a fundamental requirement for identifying the correct equilibrium path in incremental iterative solution procedures— and symmetrisable, thus allowing the use of Newton solvers without loss of quadratic convergence.

The works mentioned thus far, with the notable exception of [23, 24] dealt with static analyses. Crisfield et al. [29] discussed different types of implicit time-integration algorithms for the dynamic analysis of spatial elastic beams undergoing large rotations and translations, but small strains. Two main integration algorithms are presented, namely the end-point algorithm (see Simo [30]), solved with the Newmark and α-methods, and the mid-point algorithm first developed in Crisfield and Shi [31] and Galvanetto and Crisfield [32], where the inertia force vector is evaluated through the solution of the equation of motion and the introduction of a constant mass matrix. It is shown that stability of the algorithms depends on the time-step size, and even introducing numerical damping and dynamic time-stepping, instability may occur with uncontrolled energy growth.

Le et al. [33, 34, 35] made further advancements framing the theory for elasto-plastic CR beam elements in the 2D [33] and 3D [34, 35] dynamic analyses, studying the effects that the approximations in the evaluation of the mass matrix have on the solution. Employing a consistent mass matrix, they obtained higher levels of accuracy and stability even with a coarse mesh, compared to the less accurate results

obtained employing a constant mass matrix. Their extensive work has spawned a considerable amount of 3D CR elements for the analysis of beams with open cross-sections [36, 37, 38, 39, 40].

Other examples of corotational applications can be found in Areias et al. [41], where triangular shell elements are applied to the fracture modelling of ductile structures. Longva [42] has employed linear elastic CR beam elements for the dynamic analysis of multilayered subsea pipelines. Yaw et al. [43, 44] have used the corotational framework for the development of a non-linear mesh-free model. Parker and O'Brien [45] successfully employed tetrahedral CR elements for real-time simulations in a videogame environment, were solid fracture was modelled through the propagation of partially pre-rendered fracture surfaces. Courtecuisse et al. [46] employed a corotational model for the real-time simulation of soft tissue biomechanics. The model took advantage of Graphic Processing Units (GPU) acceleration to solve an implicit solution algorithm in real time.

Figure 1.5 illustrates, as an example, the application of the corotational framework to the kinematic description of a planar beam with two nodes. In the Total Lagrangian framework, the element deformation vector, **u**, is defined by the displacement and rotation of each node, with respect to the global reference frame, for a total 6 degrees of freedom (as shown on the left-hand side of Figure 1.5).

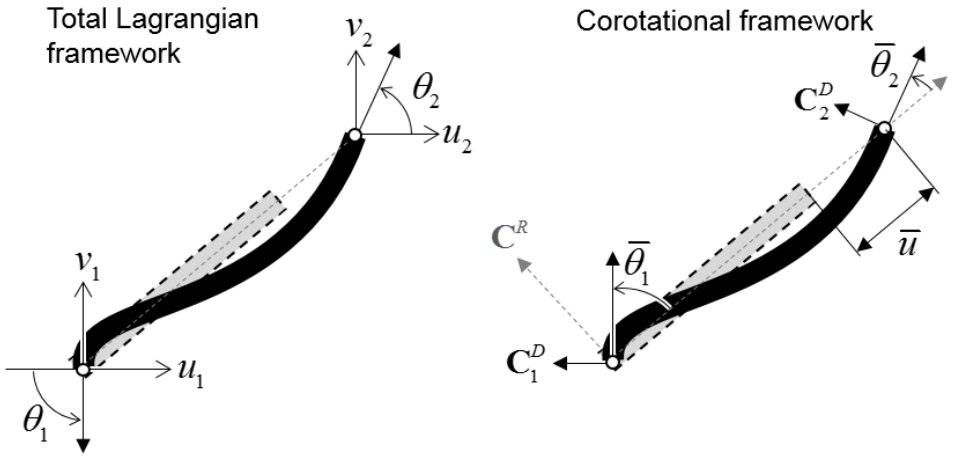

Figure 1.5: Comparison of two kinematic descriptions for planar beams: Total Lagrangian framework (left) and Corotational framework (right).

In the CR framework, the rigid motion of the beam is evaluated through the displacements of the C^R frame, whilst its deformation is defined by just the two nodal rotations (with respect to C^R), and the element elongation. Therefore, the local deformation vector, $\bar{\mathbf{u}}$, has only 3 degrees of freedom. The differentiation of $\bar{\mathbf{u}}$ with respect to $\mathbf{u}$ gives the transformation matrix $\mathbf{B}$

$$\mathbf{B} = \frac{\partial \bar{\mathbf{u}}}{\partial \mathbf{u}}. \tag{1.2}$$

that allows to transform any tensor from the base to the deformed configuration. The expression of the force vector, $\mathbf{f}$, is then recovered by noting that the element internal energy is independent of the reference frame. Equating the virtual work in the two configurations leads to

$$U = \delta \bar{\mathbf{u}}^{\mathrm{T}} \bar{\mathbf{f}} = \delta \mathbf{u}^{\mathrm{T}} \mathbf{f}. \tag{1.3}$$

which gives

$$\mathbf{f} = \mathbf{B}^{\mathrm{T}} \bar{\mathbf{f}}. \tag{1.4}$$

In the expression above, $\bar{\mathbf{f}}$ is the local force vector and $[\ ]^{\mathrm{T}}$ indicates the transpose operator.

The implementation of the CR framework to finite element static analyses requires the definition of a stiffness matrix $\mathbf{K}$ [22] or, in the case of dynamic analysis, a mass matrix $\mathbf{M}$ [34, 16]. In general, the stiffness matrix is obtained in the global reference frame by differentiating the force vector with respect to $\mathbf{u}$:

$$\mathbf{K} = \frac{\partial \mathbf{f}}{\partial \mathbf{u}}. \tag{1.5}$$

Taking into account equation (1.4) a consistent expression of $\mathbf{K}$ is obtained

$$\mathbf{K} = \mathbf{B}^{\mathrm{T}} \bar{\mathbf{K}} \mathbf{B} + \left. \frac{\partial \mathbf{B}^{\mathrm{T}} \bar{\mathbf{f}}}{\partial \mathbf{u}} \right|_{\bar{\mathbf{f}}}. \tag{1.6}$$

The kinematic formulation for dynamic analysis requires the definition of a mass

matrix. Most FEA solvers commonly use a constant mass matrix, evaluated once at the beginning of the analysis, to reduce the computational cost [16]. A consistent expression for $\mathbf{M}$ can be obtained from the evaluation of the kinetic energy, K, [33, 34]:

$$K = \frac{1}{2}\dot{\mathbf{u}}^{\mathrm{T}}\mathbf{M}\dot{\mathbf{u}}\,, \tag{1.7a}$$

$$\mathbf{M} = \mathbf{T}^{\mathrm{T}}\bar{\mathbf{M}}\mathbf{T}\,, \tag{1.7b}$$

where $\mathbf{T}$ is a rotation matrix. Le et al. [34] have investigated the effect of using different approximations for the mass matrix on the solution, comparing the results obtained using an approximated expression for the mass matrix, calculated at the beginning of the analysis (namely the constant lumped mass matrix or the Timoshenko mass matrix, [34]), to those obtained with a consistent mass matrix calculated at each increment using the non-constant expression equation (1.7). The study has shown with multiple examples that the consistent formulation requires more computational time, but is able to capture the displacement history of beams with satisfaction even with a significantly small number of elements. Nevertheless, as originally noted in [26], the computational advantage is lost when performing analyses that require a refined mesh, due to the computational cost added by solving equation (1.7) for every element at every increment.

Following the approach of Felippa and Haugen [22] and Le et al. [34], a corotational beam element is developed in this thesis for the numerical dynamic analysis of pipe whips. The kinematic formulation here employed omits the calculation of the stiffness matrix $\mathbf{K}$ and employs a constant lumped mass matrix $\mathbf{M}$, which was chosen in favour of a consistent mass matrix, with the objective or reducing the computational cost. The present work presents significant advancement to [22, 34] through the adoption of elasto-plastic hardening-softening constitutive model that capture the change in bending moment when collapse occurs, eliminating the need to perform computationally expensive integration of the cross-sectional stresses to calculate the plastic moment during large deformations.

1.2.3 Impulsive response of metal plates

Metal plates, usually made of steel or aluminium alloys, constitute common components in civil, industrial and military structures, with a range of applications varying from pressure vessels [47, 48] to ship superstructures [49, 50]. Structures must be tested under a variety of loading conditions to assess the mechanical response and the consequences of hazardous incidents. The analysis of their failure mechanisms, especially under explosive loadings, is a topic of ongoing study [51, 52], which is of fundamental importance to many fields, in particular to the defence sector, due to its inherent complexity, owing to its short time scale, the occurrence of fracture and the possibility of fragmentation.

The experimental investigations of Teeling-Smith and Nurick [51], Nurick et al. [53, 54, 55] and Olson et al. [56] observed that metal plates subjected to uniformly distributed blast loadings, generated by the detonation of an explosive charge, have three typical responses. Ordered by increasing loading intensity, they are classified as:

Failure mode I — characterised by large inelastic deformation, without fracture;

Failure mode II — where large inelastic deformation is accompanied by material rupturing along the support due to tensile failure;

Failure mode III — where rupturing occurs along the support due to transverse shear failure, with negligible deformation.

When modes II or III occur, the propagation of the fracture surface leads to the detachment of part of the plate from its support, generating high speed fragments that can impact on nearby bodies, causing safety concerns for the integrity of equipment and personnel. Some studies [55, 57] have occasionally observed an additional failure mode, in a range of loading intensity between mode I and II, characterised by large inelastic deformation and partial rupturing along the support, but without complete detachment, classified as **failure mode II***. The sequence of failure modes observed in the case of impulsively loaded quadrangular plates is illustrated in Figure 1.6.

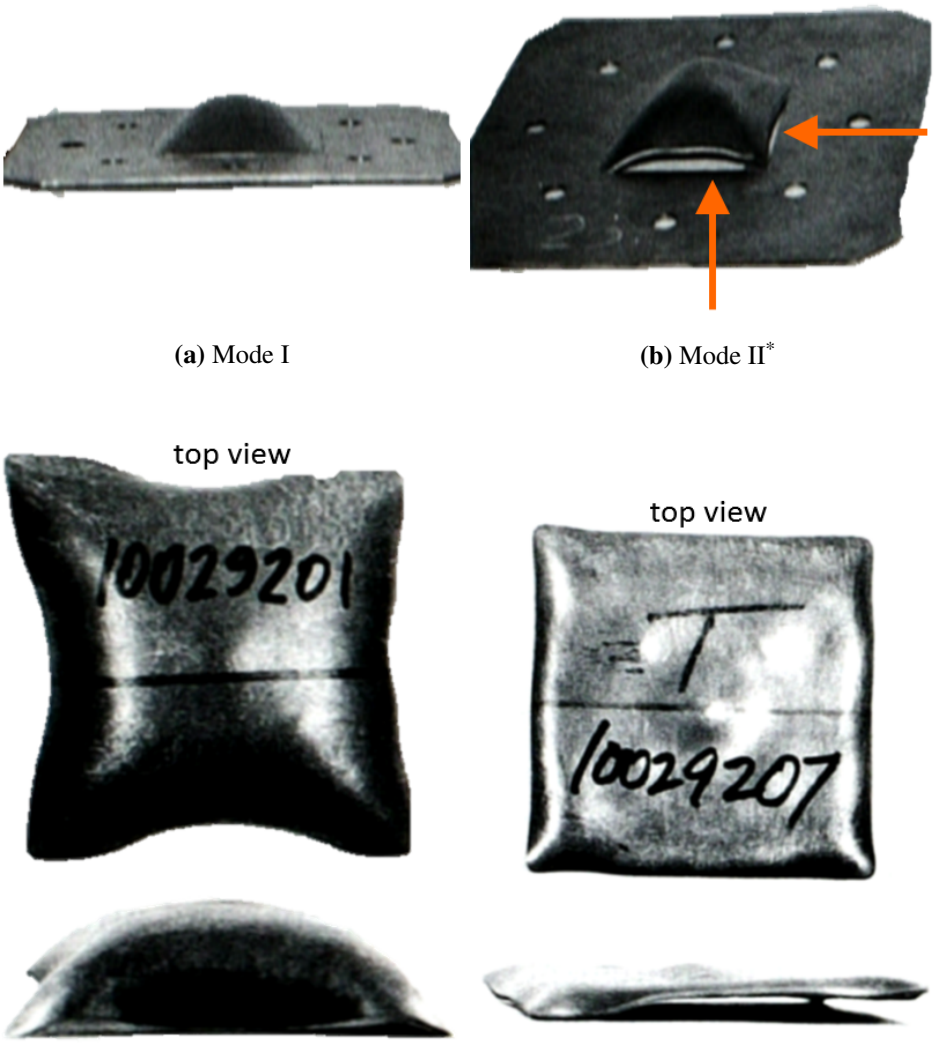

(a) Mode I **(b)** Mode II* **(c)** Mode II **(d)** Mode III

Figure 1.6: Failure modes of clamped square steel plates subjected to impulsive blast loadings. Adapted from [56].

Yuen et al. [52] reported a comprehensive review of numerous experimental studies that investigated the impulsive behaviour of plates with various geometries (i.e. circular [51, 58], square [56, 54, 55] or rectangular plates [57, 59, 50]), boundary conditions [60, 57, 52], stiffener configuration [61, 62] and loading distributions [61, 58, 63]. In the first investigation, Teeling-Smith and Nurick [51] studied the deformation of circular clamped mild steel plates subjected to uniform blast loading, giving the classification of the three main failure modes. They analysed the change in permanent central deflection, W, with the blast intensity, I, observing that

W initially increases with I in mode I, and that the maximum deflection is obtained in mode II, when rupture occurs along the support. Further increasing the intensity leads to the decrease of W, until it becomes negligible in mode III. The study also noted that, whilst the mode I-II transition is clearly marked by the initiation of rupturing at the support, it was not possible to identify with certainty a threshold separating mode II and III.

Olson et al. [56] drew very similar conclusions when testing square plates under the same loading conditions; the only difference was noted in the initiation of the rupture mechanism which, in the case of a square plate, begins at the midpoint of each side. Four cracks are formed that rapidly propagated along the supports. As the cracks converge on the corners, they deviate towards each other and eventually merge, causing the separation of the plate from its support. Following the detachment, the deviated crack path takes the shape illustrated in Figure 1.7 (a). Nurick and Shave [55] repeated the study on square plates for additional values of impulse intensity, observing for the first time the occurrence of mode II*, at the transition between mode I and II. In mode II*, rupture initiates at the midpoint of one or more sides, but stops before it reaches the corner, without causing detachment. It was also observed that, for the same value of I, different plates could display partial rupturing

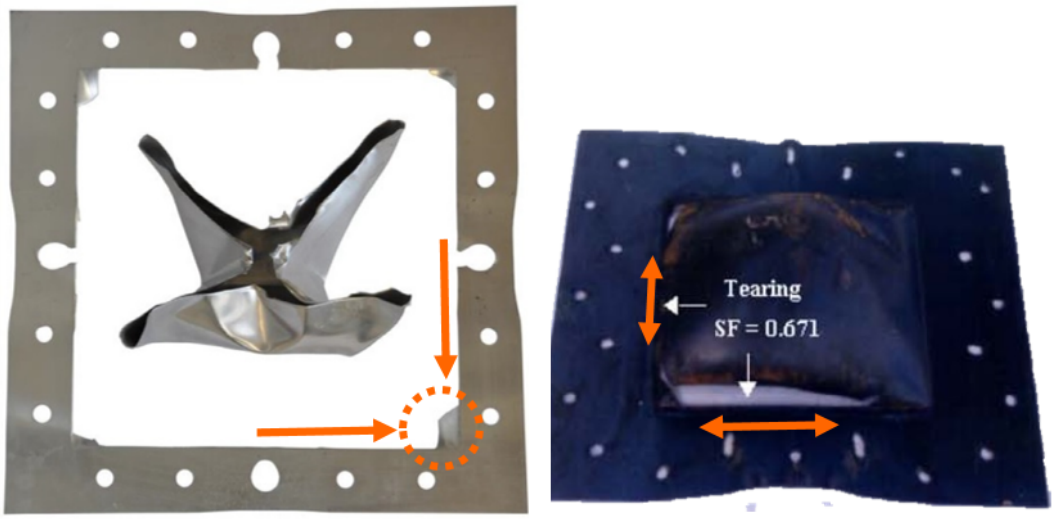

(a) Mode II - detachment path **(b)** Mode II* - partial rupturing

Figure 1.7: (a) Crack path deviation, adapted from [64]. (b) Partial rupturing on two sides, adapted from [55].

on one or more sides due to the presence of material imperfections or the uneven tightening of the clamping bolts, as depicted in Figure 1.7 (b). Furthermore, it was noted that failure mode II could be separated in two regimes: an initial mode IIa, where the central deflection increases with I, followed by mode IIb, where the deflection decreases with I. Finally, Nurick and Shave [55] remarked that rupture is determined by the two concurring mechanisms of tensile failure, which prevails at low impulse intensity, and shear failure, which becomes predominant as the loading intensity increases.

More recently, Jacob et al. [58] have studied the effect of the stand-off distance of the explosive charge on the failure mode of clamped circular plates, whilst keeping a constant explosive charge. When the stand-off distance is larger than the plate radius, the plate is hit by a uniformly-distributed blast; the deformation profile assumes a dome shape, with a maximum central deflection that rapidly decreases as the stand-off distance increases. When the stand-off distance is smaller than the radius, the plate is hit by a localised blast at its centre, causing a complex deformation profile, composed by a central dome superimposed on a global dome (see Figure 1.8 (a)). If the loading intensity is increased at a small stand-off distance, the central portion of the plate undergoes complete detachment under the effect of the localised load, in a failure mode named capping (or mode IIc). If the impulse is increased further, multiple crack paths propagate radially from the central portion

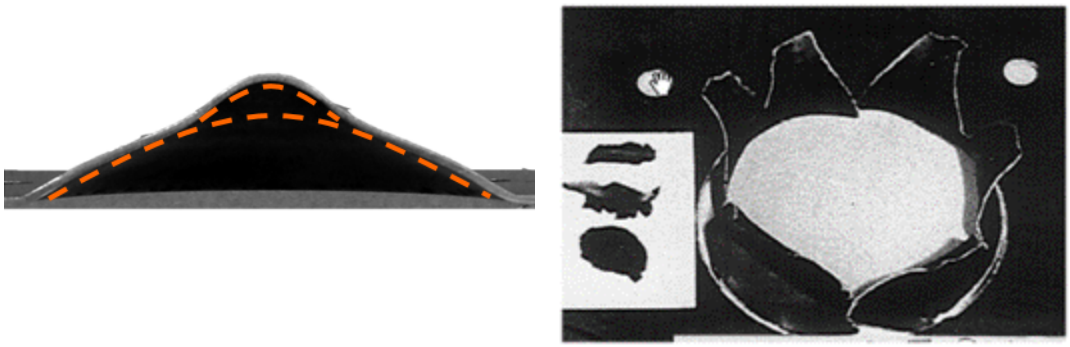

(a) Mode I - (localised dome) **(b)** Petalling

Figure 1.8: Plates failure modes due to localised blasts: (a) double dome profile and (b) petalling. Adapted from [58].

in a fashion named petalling [58], as depicted in Figure 1.8 (b). A similar response was observed by Langdon et al. [61] in the study of locally loaded quadrangular plates.

The discussion of the experimental findings discussed here, along with the observations on welded and stiffened plates presented in [52], can be summarised as follows:

- The principal failure modes of impulsively loaded metal plates are, ordered by loading intensity: mode I, mode II*, mode II (a and b), mode III;
- Under the same loading conditions, quadrangular and circular plates display similar responses;
- The sole exception is the fracture propagation observed in mode II and III for quadrangular plates, which initiates at the lateral midpoints and deviates at the plate corners before detachment;
- Reducing the stand-off distance causes the localisation of the blast;
- The deformation profile of locally loaded plates has the shape of a central dome sitting atop a global dome;
- In locally loaded plates, mode II and III are replaced by capping (mode IIc) and petalling, respectively;
- Increasing the stiffness of the boundary (e.g. welded or machined supports) increases the resistance to tearing, i.e. rupture initiates at higher loading intensity;
- Ordered by increasing stiffness, possible type of supports are: clamped, welded, machined supports;
- The welding of stiffeners reduces the amount of deformation;
- Rupturing and fracture initiate at lower impulse in the regions where the stiffener is welded.

Jones [65] presented an extended survey of theoretical studies aimed at predicting the deformation profiles of plates subjected to uniform impulsive blasts in mode I. With the hypothesis of rigid-perfectly plastic material, the models reported in [65] are capable of predicting the permanent transverse deflection of circular and

quadrangular plates with various boundary conditions. In particular, the maximum transverse deflection at the centre of the plate, W, is completely determined by the initial blast velocity v_0, the surface area A, the plate thickness H, the material density ρ and the yield stress σ_Y,

$$W = f(v_0, A, H, \rho, \sigma_Y) . \tag{1.8}$$

For example, in the case of fully clamped square plates, the dimensionless central deflection is evaluated as [65, equation 24 A]

$$\frac{W}{H} = \left(1 + \frac{2\lambda}{3}\right)^{1/2} - 1 \tag{1.9}$$

with

$$\lambda = \frac{\rho A}{\sigma_Y} \left(\frac{v_0}{H}\right)^2 . \tag{1.10}$$

More comprehensive models that take into account material strain-rate dependence were also reported [65]. More recent models have been developed to successfully predict the permanent deflection profile of plates subjected to centrally localised blasts [66, 67].

The theoretical models are only capable of predicting the plate response in the absence of fracture, and are therefore limited to the assessment of failure mode I. However, finite element analyses employing constitutive models of material failure and fracture mechanics are capable of predicting the permanent deformation when rupture occurs, and also of analysing the propagation of the fracture surface.

A review of FE models of the failure of quadrangular steel plates is presented by the author in [68]. A model incorporating material and geometrical nonlinearities and material strain-rate sensitivity was employed by Rudrapatna et al. [69, 62] to predict the post-failure response of a blast-loaded stiffened square plate deforming in mode II and III. In their work, the plate was discretised using plate elements, and the compliance of the clamped supports was modelled using spring elements. The pressure loading from the explosive charge was assumed as a rectan-

gular pulse uniformly distributed over the plate surface. The progression of fracture along the boundaries was modelled with a node-release algorithm, and an interactive failure criterion between membrane and transverse shear stress was proposed to predict the transition between the two failure modes. The numerical results were compared against a small number of experimental data, showing limited agreement.

Yuan and Tan [70] used a solid elements model to predict the through-the-thickness propagation of the fracture surface in square and rectangular plates. The model employed a strain-rate dependent material model with simplified damage criteria that neglected the dependence of the failure parameters on the element size; fictitious boundary conditions were used to guarantee stress convergence at the support, where failure occurs.

More recently, Aune et al. [71] used a shell elements model to reproduce the experiments on plates with pre-formed holes subjected to a pressure wave in water generated in a shock tube facility. The simulations assumed a constant value for the initiation of damage, and crack propagation was modelled through element deletion and mesh refinement. The study investigated the influence of the boundary compliance on the dynamic response, noting that an excessive boundary mobility leads to an overestimation of the central deflection, and that using fully-clamped boundary conditions leads to predictions that are closer to the experimental data.

Aune et al. [64] used a temperature-dependent material model to analyse the deformation of steel and aluminium plates exposed to airblast loading. The simulation modelled the propagation of cracks using an energy-based failure criterion with element deletion. The results provided good agreement on the prior-to-failure transient deformation profiles, compared with experimental data obtained from 3D-DIC imaging [63], and on the effect of stand-off distance on the central deflection. However, a less satisfying agreement was obtained when comparing the crack path deviation at the plate corners when detachment occurs.

It must be noted that most of the numerical works here reported employed oversimplified strain-based damage criteria that neglect the dependence of the failure parameters on the element size. In the present work, FE simulations are carried

out with a shell element model implementing more comprehensive damage criteria [72, 73], with the aim of examining the crack propagation (modelled through element deletion) and the influence of impulse intensity and boundary compliance on the failure modes of quadrangular plates. The damage parameters are extracted from experimental tensile and shear tests performed on mild steel specimens; the parameters are opportunely calibrated to ensure the mesh insensitivity of the failure mechanisms [68].

It is worth mentioning here alternative approaches for the modelling of fracture, in addition to the aforementioned damage mechanics approach with element deletion. For instance, Imachi et al. [74] introduced a peridynamic model (i.e. a non-local continuum mechanics formulation) employing dynamic stress intensity factors to analyse crack propagation in brittle materials. Nguyen et al. [75] analysed the fracture mechanisms of quasi-brittle materials implementing an FE damage model based on non-local strain gradient theory, coupled with elastic and progressive softening constitutive laws. Wu et al. [76] proposed to simulate metal grinding processes using a mesh-free particle Galerkin method. The model implements a strain-based law and a bond-based failure criterion where fracture is simulated through the disconnection of neighbouring particles upon reaching a critical strain value.

1.3 Motivation of work and objectives

Notwithstanding recent computational advancements, commonly employed FE simulations for the failure analysis of thin-walled structures, due to structural collapse or material fracture, implement oversimplified models that fail to address with sufficient accuracy some fundamental phenomena. For example, FE simulations aimed at modelling the behaviour of pipe whips are either computationally inefficient, as in the case of shell-element models [11, 13], which require extremely refined mesh throughout the model to predict the cross-sectional ovalization, or are not capable of capturing successfully the intrinsic cross-sectional collapse mechanism (i.e. beam-element models, rigid-perfectly plastic finite difference models [2]. Pipe and elbow elements exist that are able to model the pipe collapse only in static analyses, and with limited accuracy regarding the stress distribution and ovalization mode, compared to shell elements [17]. On a similar note, FE models used in the failure analysis of impulsively loaded plates employ failure models that neglect the sensitivity of damage on the characteristic element length [70, 71, 64]. The modelling of damage depends on the element size for geometrical and mathematical reasons: (i) when portraying the propagation of damage through element deletion, the mesh must be sufficiently refined to simulate the formation of small cracks [70], and (ii) the model parameters used in the calculation of the energy required for the element deletion depend on the characteristic element length [64]. The damage criteria employed in [70] and in [71, 64] neglect this second aspect by calibrating the damage parameters on a single element size and are therefore not suitable for an accurate study of the modes of deformation that are influenced by the propagation of fracture. The scope of this thesis is to investigate the limitation of currently used numerical models for thin-walled structures and research effective methods to improve their predicting capabilities.

In the modelling of pipe whips, the approach chosen was to develop a computationally efficient element code, employing ad-hoc constitutive models obtained through the numerical testing of pipe collapse in bending. In the modelling of impulsively loaded plates, a combination of experimental and numerical procedures

was applied to the calibration of the damage parameters, leading to the establishment of a procedure that is phenomenologically comprehensive yet easily implemented. In the process of developing the aforementioned models, the main objectives of this research work are:

1. To develop a computationally efficient beam element code to model the flexural behaviours of pipe whips accurately.

2. To assess the influence of pipe geometry and loading conditions on the hazard zone.

3. To derive empirical laws that predict the pipe response, useful for the design of pipe systems.

4. To develop a mesh-size independent fracture model for shell elements.

5. To test the validity of the model by investigating the influence of plate topology and boundary conditions on the failure modes of blast loaded plates.

6. To establish a criterion for identifying the impulse threshold between failure modes II and III.

1.4 Outline of the thesis

The thesis is organised as follows. In Chapter 2, a two-dimensional element (VUEL BM2D) is developed for the simulation of in-plane pipe whips. The element employs a corotational description of the beam kinematic, based on the works of Felippa and Haugen [22] and Le et al. [34], commonly used in fast-converging algorithms, to reduce the computational costs. FE simulations of bending tests on thick and thin pipes are performed to build a moment-curvature constitutive model capable of capturing the cross-sectional collapse of pipes.

In Chapter 3, simulations implementing the VUEL BM2D code and the moment-curvature model are used for the analysis of thick and thin in-plane pipe whips, validated against the experimental data by Reid et al. [2]. The validated model is then employed in parametric studies aimed at identifying the dependence

of the deformation mechanisms of pipe whips on the structural geometry and loading conditions. The hazard zone observed numerically is compared to analytical predictions obtained with a rigid-perfectly plastic beam model developed by Stronge and Yu [8]. Finally, the VUEL BM2D model is benchmarked against shell element simulations performed in Abaqus/explicit to assess the computational efficiency of the code.

Chapter 4 presents the development of a three-dimensional element (VUEL BM3D) for the simulation of out-of-plane pipe whips. The element employs the 3D corotational formulation of Battini [27] and Le [33] and the moment-curvature law developed in Chapter 2, together with a constitutive law for torsion. The VUEL BM3D code is then benchmarked against numerical simulations of out-of-plane pipe whips performed in Abaqus/explicit using traditional shell and beam elements, analysing its computational cost and the capability to capture collapse mechanisms when bending and twisting of the pipe occur simultaneously.

In Chapter 5, a shell-element model is developed for simulating the large deformation and fracture of steel plates loaded impulsively. The simulation employs two constitutive models to describe material failure under tensile and shear conditions, based on the triaxiality-dependent Modified Mohr-Coulomb criterion [72]. Experimental tests on un-notched and pre-notched steel S235 dog-bone specimens were performed to measure the material response in a wide range of loading conditions, from pure shear to biaxial tension, and to calibrate the damage initiation parameters. Numerical simulations reproducing the uniaxial tensile and pure shear experiments were performed to calibrate the damage evolution parameters and ensure mesh insensitivity of damage. The calibrated shell-element model was then employed in simulations reproducing impulsive experiments on steel plates by Olson et al. [56] and Nurick and Shave [55] and successfully validated. The simulations were used to derive a phenomenological model for the prediction of the mode II-III impulse threshold, based on the measurement of the crack propagation velocity.

In Chapter 6, the plate model is used to analyse the deviation of the crack path observed experimentally. Parametric studies are then performed to investigate the

effect of plate topology, loading intensity and boundary conditions on the failure modes of square and rectangular plates. In particular, a novel failure mode was numerically discovered for simply-supported rectangular plates where the crack path deviation occurs in the central region of the plate, rather than close to the corners.

Chapter 7 presents a summary of the principal conclusions of this work and future research topics.

1.5 Contribution to existing literature

Part of the research work reported in this thesis has appeared in the journal article:

> D. Schiano Moriello, F. Bosi, R. Torii, P.J. Tan. Failure and detachment path of impulsively loaded plates. *Thin-Walled Structures*, 155:106871, oct 2020.

Chapter 2

Modelling of plastic deformation of thin-walled pipes

2.1 Introduction

This chapter presents the development of a two-dimensional corotational element, named VUEL BM2D, for the dynamic FE analysis of pipes undergoing large deformations. The element, based on the corotational formulations of beams developed by Felippa and Haugen [22] and Le et al. [34], present an improvement in the currently available simulation techniques by implementing two separate constitutive models that describe the behaviour of metal pipes under tensile and bending loadings. The application of the VUEL BM2D element for the simulation of in-plane pipe whips is discussed in Chapter 3; the development of a three-dimensional element, named VUEL BM3D and its application for modelling out-of-plane pipe whips is the subject of Chapter 4.

A schematisation of the solution scheme employed in FEA to model dynamic analyses is illustrated in Figure 2.1 (a). At the beginning of the simulation, the prescribed initial and boundary conditions are applied to the elements that constitute the discretisation of the body. At any increment, the nodal displacements computed from the previous time step are used to evaluate the nodal forces, according to selected material models.

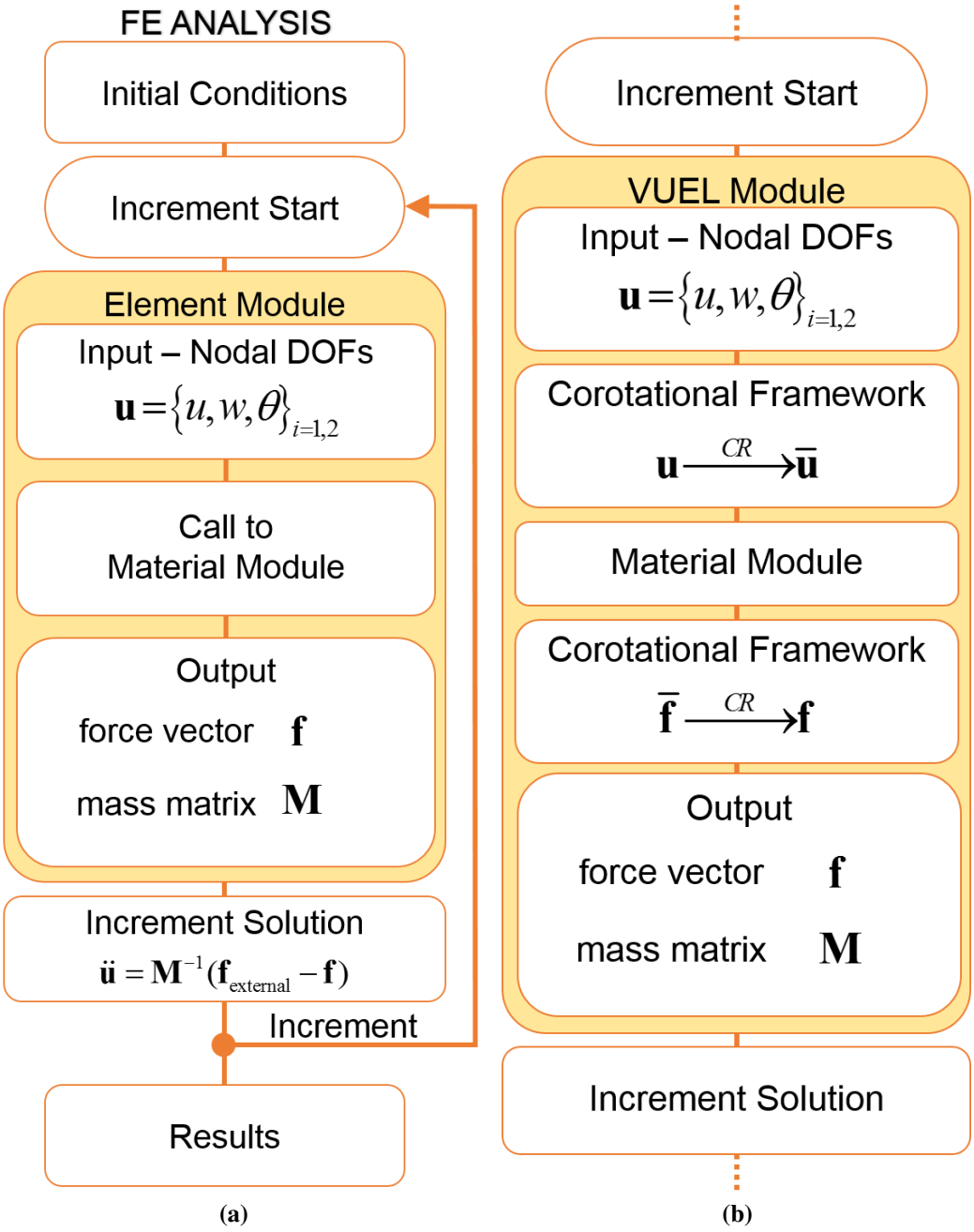

Figure 2.1: (a) Schematisation of a dynamic FEA solution algorithm. (b) Schematisation of a corotational element, VUEL, replacing the element module in the algorithm.

At the end of the increment, the nodal displacements $\mathbf{u}$ and accelerations $\ddot{\mathbf{u}}$ induced by the forces $\mathbf{f}$ are calculated by solving Newton's law, $\mathbf{f}=\mathbf{M}\ddot{\mathbf{u}}$, where $\mathbf{M}$ is the mass matrix. The procedure here described is *explicit* in the sense that the solution at any increment is obtained via direct inversion of Newton's law, with-

out the use of an iterative algorithm, whereas *implicit* procedures employ Newton's method to obtain the solution as a series of increments, performing iterations to obtain equilibrium within each increment. The advantage of the explicit scheme consists in the simplicity and robustness of the solution procedure and the relatively inexpensive cost of each increment compared to the increments in an implicit scheme [16]. At each increment during the calculation of the body motion, geometrical non-linearities may arise as a consequence of large rotations and translations, which are taken into account in the derivation of displacements, velocities and accelerations in the equation of motion, whilst material non-linearities may occur with the development large deformations, which are taken into account with non-linear material models.

Figure 2.1 (b) illustrates a corotational element, VUEL, replacing the element module in the solution algorithm. The corotational framework is used at the beginning of the element module to separate the deformation from the displacement, and to transform the displacement vector from the global to the local reference frame, $\mathbf{u} \rightarrow \bar{\mathbf{u}}$. The material module is called to evaluate the components of the local force vector, $\bar{\mathbf{f}}$, then the corotational framework converts the forces back to the global reference frame, $\bar{\mathbf{f}} \rightarrow \mathbf{f}$. Using the corotational framework enforces material-frame indifference and consents to use non-linear constitutive models for the relation between local rotations and cross-sectional moments based on experimental observations from bending tests performed on pipes [77]. Furthermore, the method involves a reduction of the number of degrees of freedom when operating in the local frame, which contributes to the model simplicity and has the potential to reduce the computational cost. In the present work, non-linear material models are used for the calculation of local forces. In particular, a non-linear constitutive model is developed that correlates the moment in bending to the beam curvature.

2.2 Bernoulli 2D corotational beam element

This section deals with the derivation of a two-dimensional beam element within the corotational framework. The element code is developed in the language Fortran 75

as a subroutine, suitable for the implementation within the dynamic solution scheme of the commercial FE software Abaqus/explicit [16]. The formulation follows the approach of Felippa and Haugen [22] in the definition of the local strains, and that of Le et al. [34] in the definition of the mass matrix and a transformation matrix that is not limited to small rotations. The novelty of the approach consists in the application of constitutive models for metal plasticity and the flexural behaviour of hollow beams, used for evaluating the local forces. The corotational element will be used for the simulation of pipes with high slenderness ratios $L/D \approx 50 >> 15$. Under these conditions, transverse shear is negligible and it is possible to use the Bernoulli beam theory for the formulation of the local kinematics, rather than the more complex Timoshenko bean theory.

The derivation of an element subroutine for the explicit solution scheme is achieved with the definition of just two quantities: the internal force vector $\mathbf{f}$, which depends on the definition of the degrees of freedom and appropriate constitutive relations, and the mass matrix $\mathbf{M}$, which is independent of the constitutive relations.

2.2.1 Corotational kinematics of 2D beams

The corotational framework for a planar beam with two nodes is presented visually in Figure 2.2. Each node is identified in the global reference frame by the coordinates $(x_i, y_i)_{i=1,2}$ and is assigned with three degrees of freedom: the two displacements, u_i and w_i, and the rotation θ_i. The deformation vector is therefore

$$\mathbf{u} = \{u_1, v_1, \theta_1, u_2, v_2, \theta_2\}^{\mathrm{T}}, \tag{2.1}$$

to which corresponds the internal force vector

$$\mathbf{f} = \left\{F_{x,1}, F_{y,1}, M_1, F_{x,2}, F_{y,2}, M_2\right\}^{\mathrm{T}}. \tag{2.2}$$

The initial configuration of the beam is defined by the rotation angle β_0 and the element length L. After the initial state, the beam can move and deform in the xy-plane due to the force applied. At any time increment, a corotated frame $\mathbf{C}^R$

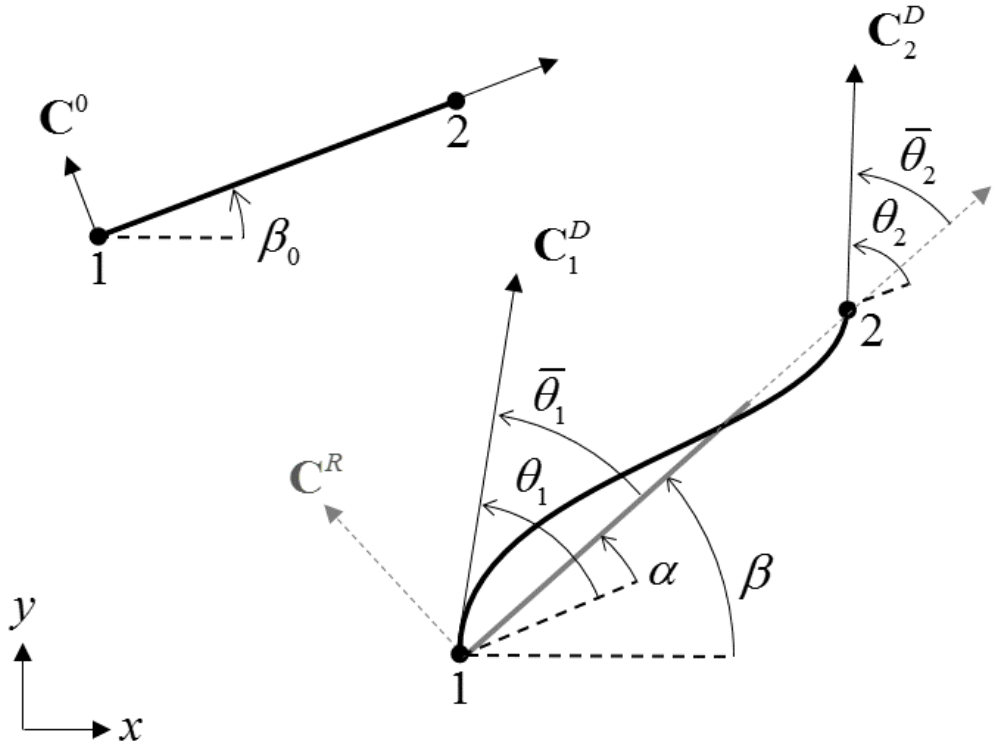

Figure 2.2: Reference frames for a planar beam element with two nodes. The Cartesian coordinates (x,y) define the global reference frame, and $\mathbf{C}^0$ is the initial configuration of the element. At any time increment, $\mathbf{C}^R$ identifies the current (corotated) reference frame, whereas $\mathbf{C}_1^D$ and $\mathbf{C}_2^D$ the deformed configuration at each node.

is defined that moves rigidly with the element; its orientation β is identified by a straight line connecting the two nodes.

To separate the pure deformational and rigid components of motion, the local frames $\mathbf{C}_1^D$ and $\mathbf{C}_2^D$ are introduced that follow the rotation of each node, with local orientation $\bar{\theta}_1$ and $\bar{\theta}_2$ with respect to the frame $\mathbf{C}^R$. The decomposition of motion into its rigid and deformational components allows for arbitrarily large rotations at each end, independent of the stress state, provided that a sufficiently small number of elements is employed [34]. Based on the local frames, the local deformation vector can then be defined as

$$\bar{\mathbf{u}} = \left\{\bar{u}, \bar{\theta}_1, \bar{\theta}_2\right\}^{\mathrm{T}}. \tag{2.3}$$

The first component of $\bar{\mathbf{u}}$ is the variation of the element length, calulated as

follows:

$$\bar{u} = L_n - L\,, \tag{2.4a}$$

$$L = \sqrt{(x_2 - x_1)^2 + (y_2 - y_1)^2}\,, \tag{2.4b}$$

$$L_n = \sqrt{(x_2 + u_2 - x_1 - u_1)^2 + (y_2 + v_2 - y_1 - v_1)^2}\,. \tag{2.4c}$$

The remaining components are the local rotation angles $\bar{\theta}_i$, obtained from the components of $\mathbf{u}$ through the rigid rotation $\alpha = \beta - \beta_0$, so that

$$\bar{\theta}_i = \theta_i - \alpha = \theta_i - \beta + \beta_0\,, \quad i = 1,2\,. \tag{2.5}$$

The orientation of $\mathbf{C}^0$ and $\mathbf{C}^R$ are evaluated from the nodal coordinates,

$$\cos\beta_0 = \frac{x_2 - x_1}{L}, \quad \sin\beta_0 = \frac{y_2 - y_1}{L} \tag{2.6a}$$

$$\cos\beta = \frac{x_2 + u_2 - x_1 - u_1}{L_n}, \quad \sin\beta = \frac{y_2 + v_2 - y_1 - v_1}{L_n}\,, \tag{2.6b}$$

which leads to

$$\cos\alpha = \cos\beta\cos\beta_0 + \sin\beta\sin\beta_0 \tag{2.7a}$$

$$\sin\alpha = \sin\beta\cos\beta_0 - \cos\beta\sin\beta_0 \tag{2.7b}$$

and

$$\cos\bar{\theta}_i = \cos\theta_i\cos\alpha + \sin\theta_i\sin\alpha \tag{2.8a}$$

$$\sin\bar{\theta}_i = \sin\theta_i\cos\alpha - \cos\theta_i\sin\alpha\,. \tag{2.8b}$$

The following procedure is employed to obtain expressions of the local angles that

are not limited in magnitude [34],

$$\begin{cases} \bar{\theta}_i = \sin^{-1}\left(\sin\bar{\theta}_i\right) & \text{if } \sin\bar{\theta}_i \geq 0, \quad \cos\bar{\theta}_i \geq 0 \\ \bar{\theta}_i = \cos^{-1}\left(\cos\bar{\theta}_i\right) & \text{if } \sin\bar{\theta}_i \geq 0, \quad \cos\bar{\theta}_i < 0 \\ \bar{\theta}_i = \sin^{-1}\left(\sin\bar{\theta}_i\right) & \text{if } \sin\bar{\theta}_i < 0, \quad \cos\bar{\theta}_i \geq 0 \\ \bar{\theta}_i = -\cos^{-1}\left(\cos\bar{\theta}_i\right) & \text{if } \sin\bar{\theta}_i < 0, \quad \cos\bar{\theta}_i < 0\,. \end{cases} \tag{2.9}$$

which is required for analyses where large rotations occur. The vector $\bar{\mathbf{u}}$ corresponds to a local force vector of the same length,

$$\bar{\mathbf{f}} = \{\bar{N}, \bar{M}_1, \bar{M}_2\}^{\mathrm{T}} \tag{2.10}$$

where $\bar{N}$ is the axial force, determined by the element elongation, and $\bar{M}_i$ are the bending moment associated with the angles $\bar{\theta}_i$. By differentiating vector $\bar{\mathbf{u}}$ with respect to $\mathbf{u}$ the transformation matrix $\mathbf{B}$ is obtained,

$$\mathbf{B} = \frac{\partial\,\bar{\mathbf{u}}}{\partial\,\mathbf{u}} = \begin{bmatrix} -c & -s & 0 & c & s & 0 \\ s/L_n & -c/L_n & -1 & -s/L_n & c/L_n & 0 \\ -s/L_n & c/L_n & 0 & s/L_n & -c/L_n & 1 \end{bmatrix}, \tag{2.11}$$

where $c = \cos\beta$ and $s = \sin\beta$, that gives the expression of the internal force vector in the global reference frame

$$\mathbf{f} = \mathbf{B}^{\mathrm{T}}\bar{\mathbf{f}}. \tag{2.12}$$

2.2.2 Local element formulation

Once the local deformation vector $\bar{\mathbf{u}}$ is defined, the components of the local force vector $\bar{\mathbf{f}}$ can then be evaluated, based on the definition of the local strains. The nominal strain is simply defined as

$$\varepsilon = \frac{\bar{u}}{L}. \tag{2.13}$$

from which the axial force can be evaluated as

$$\bar{N} = \sigma A_n \tag{2.14}$$

where $\sigma = \sigma(\varepsilon)$ is the stress acting on the cross-section along the longitudinal direction, which depends on the opportune choice of a constitutive model, and A_n is the current cross-sectional area which, with the hypothesis of element incompressibility, is calculated from the initial area A as

$$A_n = A\frac{L}{L_n}. \tag{2.15}$$

The corotational element employs the Euler-Bernoulli beam theory to evaluate the curvature in the local reference frame, with the Hermitian shape functions [27, 34]

$$N_1 = \bar{x}\left(1 - \frac{\bar{x}}{L}\right)^2, \tag{2.16a}$$

$$N_2 = -\left(1 - \frac{\bar{x}}{L}\right)\frac{\bar{x}^2}{L}, \tag{2.16b}$$

where $\bar{x}$ is the local coordinate along the longitudinal axis. The curvature is then expressed as a function of $\bar{x}$ with

$$k(\bar{x}) = \frac{\partial^2}{\partial \bar{x}^2}\left[N_1\bar{\theta}_1 + N_2\bar{\theta}_2\right]. \tag{2.17}$$

Substituting $\bar{x} = 0$, $\bar{x} = L$ and $\bar{x} = L/2$ in the equation above leads to the curvature values at the nodal positions and at the longitudinal midpoint [22, 27], respectively:

$$k(\bar{x} = 0) = \frac{-2}{L}\left(\bar{\theta}_2 + 2\bar{\theta}_1\right) = k_1, \tag{2.18a}$$

$$k(\bar{x} = L) = \frac{2}{L}\left(2\bar{\theta}_2 + \bar{\theta}_1\right) = k_2, \tag{2.18b}$$

$$k\left(\bar{x} = \frac{L}{2}\right) = \frac{1}{L}\left(\bar{\theta}_2 - \bar{\theta}_1\right). \tag{2.18c}$$

The element formulation is completed by the specification of a constitutive law relating the bending moment at the nodes, $\bar{M}_1$ and $\bar{M}_2$ to the curvature, as described in Section 2.5.

2.2.3 Element mass matrix and stable time increment

The explicit solution algorithm employed in this work for dynamic analyses requires the definition of a lumped mass matrix [16, 34]:

$$\mathbf{M} = \frac{\rho AL}{2} \begin{bmatrix} 1 & 0 & 0 & 0 & 0 & 0 \\ 0 & 1 & 0 & 0 & 0 & 0 \\ 0 & 0 & L^2/12 & 0 & 0 & 0 \\ 0 & 0 & 0 & 1 & 0 & 0 \\ 0 & 0 & 0 & 0 & 1 & 0 \\ 0 & 0 & 0 & 0 & 0 & L^2/12 \end{bmatrix} . \tag{2.19}$$

The matrix $\mathbf{M}$ is a constant diagonal mass matrix; the first two terms on the diagonal, corresponding to the displacement degrees of freedom, are obtained by dividing the total mass of the element between the two end nodes, whereas the third term, which corresponds to the rotational degree of freedom, is equal to the inertia of a rigid rod that is rotating about its middle point.

Finally, the coding of the user elements requires the specification of a stable time increment, that is, the upper limit to the time increment in the solution procedure. When employing an explicit time-integration algorithm, the numerical solution is only conditionally stable and a sufficiently small time increment must be selected to achieve stability [78]. Courant et al. [79] defined what is called the Courant-Friendrichs-Lewy (CFL) condition for the stability of any explicit algorithm. According to the CFL condition, a coefficient is defined,

$$C_{\mathrm{CFL}} = \frac{v\Delta t}{\Delta x} , \tag{2.20}$$

where v is the local wave speed, Δx a characteristic length, and Δt the time increment. The algorithm is then stable and converges to the correct solution only if

$C_{\mathrm{CFL}} \leq 1$ [79]. The CFL condition imposes an upper limit on the minimum stable time increment, expressed as [78]

$$\Delta t \leq C_{\mathrm{CFL}} \frac{\Delta x}{v}. \tag{2.21}$$

When applying the CFL condition to one-dimensional elements, the wave propagation speed can be defined as $v = \sqrt{E/\rho}$, leading to

$$\Delta t \leq C_{\mathrm{CFL}} \Delta x \sqrt{\frac{\rho}{E}}, \tag{2.22}$$

where the characteristic length can be written as a function of the element length, L. In the case of truss or beam elements, the stable time increment can be estimated as [16]

$$\Delta t = f \sqrt{\frac{\rho L L_n}{E}}, \tag{2.23}$$

where f is a small multiplicative factor that ensures the satisfaction of the CFL condition. In our simulations, the value of f that allows for stability is identified through an iterative process when modelling the deformation of pipe whips. When f is too high, the algorithm becomes unstable, which is evidenced by the element distorting excessively with respect to the applied load. On the other side, when f is too low, the algorithm is stable but the time to obtain the solution becomes unfeasible for an explicit analysis. Therefore, an optimum range for f must be found that ensures stability whilst maintaining a short solution time. It was found that the algorithm was stable for values in the range of $f = 0.2$–0.01, whilst keeping the solution time shorter than 2 min.

2.3 Constitutive models

The remaining step in the development of the element code is the evaluation of the axial force and the bending moments that compose local force vector $\bar{\mathbf{f}}$. The work here presented employs two constitutive laws to model the mechanical behaviour of metal pipes. At the current stage, the model neglects the effect of the strain rate on the material response and the effect of the interaction between tensile and flexural

components of the stress tensor on yield surface; the inclusion of these two effects being planned for future studies.

2.3.1 Strain hardening

The typical response of a ductile metal specimen under tensile loading is displayed in Figure 2.3, where the nominal stress-strain relation is divided into three stages. The material response is initially linear elastic (point from a to b), followed by yielding (point b), and a strain-hardening stage (from b to c). Beyond point c, the material undergoes a strain-softening stage characterised by a marked reduction of load-carrying capacity until fracture (d). During this last stage, localisation and necking occur.

In the present work, the material response is modelled through a piece-wise linear approximation of the plastic stress-strain curve obtained from a uniaxial tensile test. This simple approach, commonly employed in commercial FE software, allows to model the mechanical response with great accuracy, provided that enough material points are selected [16]. In the discretisation of the curve, the linear elastic stage is modelled as

$$\sigma = E\varepsilon\,, \quad \varepsilon \leq \varepsilon_Y \tag{2.24}$$

where E is the elastic modulus, $\varepsilon_Y = \sigma_Y/E$ the yield strain, and σ_Y the yield stress. Beyond the yield point, the definitions of true stress and true plastic strain must be

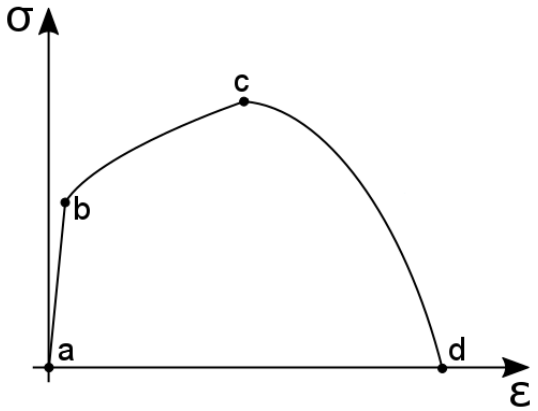

Figure 2.3: Schematics of a typical tensile response of a metal specimen.

introduced,

$$\bar{\sigma} = \sigma(1+\varepsilon)\,, \tag{2.25}$$

$$\bar{\varepsilon} = \ln(1+\varepsilon) - \varepsilon_Y\,. \tag{2.26}$$

The piece-wise linear approximation of the strain-hardening and softening stages, illustrated in Figure 2.4, is expressed in the $\bar{\sigma}$-$\bar{\varepsilon}$ space as

$$\bar{\sigma} = \bar{\sigma}^H(\bar{\varepsilon}) = \begin{cases} \bar{\sigma}_i + \dfrac{\bar{\sigma}_{i+1} - \bar{\sigma}_i}{\bar{\varepsilon}_{i+1} - \bar{\varepsilon}_i}\bar{\varepsilon}\,, & \bar{\varepsilon} \geq 0\,, \quad \bar{\varepsilon} < \bar{\varepsilon}_U\,. \\ \bar{\sigma}_U\,, & \bar{\varepsilon} \geq \varepsilon_U\,. \end{cases} \tag{2.27}$$

In the previous equation, the index i denotes the i-th point of the curve discretisation, $\bar{\sigma}_U$ is the ultimate stress reached at necking, and $\bar{\varepsilon}_U$ the corresponding strain. In the study of pipewhips, the loading is constituted by a concentrated follower force that is applied at the pipe's free end, acting orthogonally to the longitudinal axis. Under these conditions, each element is subjected to bending and the intensity of the stresses acting in the axial direction is always smaller than the ultimate stress, $\bar{\sigma}_U$. For this reason, the phenomenon of strain softening can be neglected and the softening stage can be substituted by a horizontal segment [2].

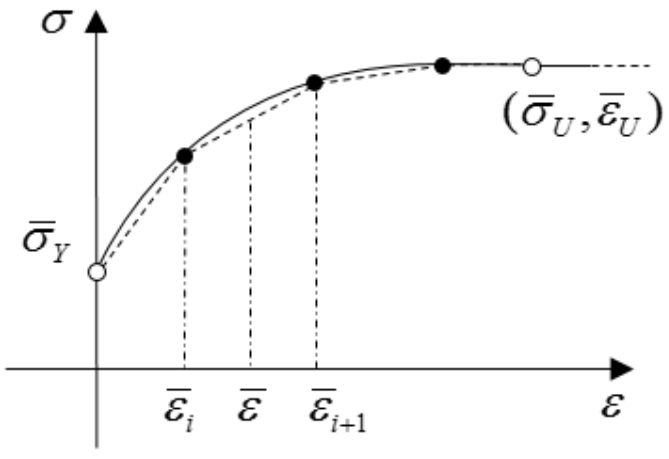

(a)

Figure 2.4: Piece-wise linear approximation of the strain-hardening stage of the tensile curve.

To successfully model situations with dynamic loading conditions, the plastic model of (2.27) must be modified to include the possibility of elastic unloading and kinematic hardening, that is, the possibility to undergo secondary hardening due to load reversal. The complete constitutive model, illustrated in Figure 2.5, is reported in Appendix A.

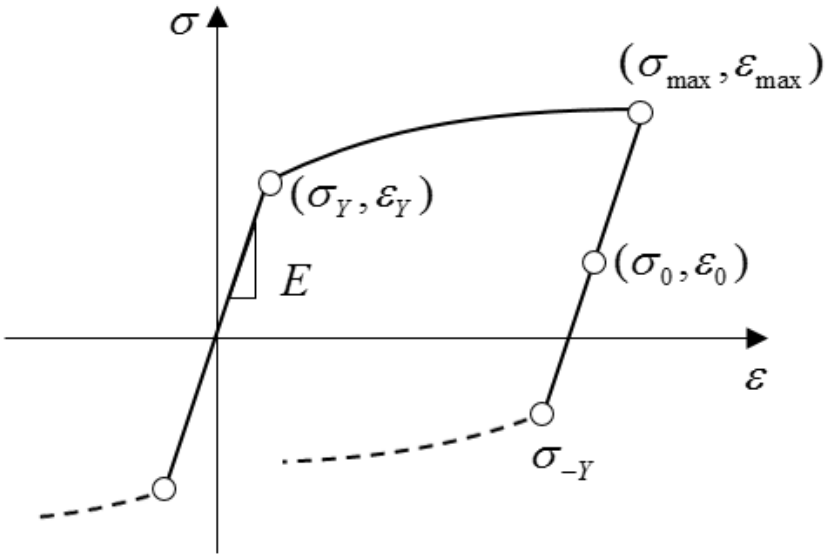

Figure 2.5: Kinematic hardening constitutive model, as described in Listing A.

2.3.2 Moment-curvature relation

The response of beams and pipes in bending is usually measured performing three-point or four-point bending tests, from which it is possible to obtain a curve correlating the bending moment to the change in curvature. The typical flexural behaviour of circular pipes, and its approximation with a piece-wise linear model, are illustrated in Figure 2.6.

As in the case of the tensile response, the moment-curvature curve is characterised by an initially linear elastic stage up to the yield point (M_Y, k_Y), followed by a hardening stage up to the maximum point (M_C, k_C) and a softening stage up to failure (M_F, k_F). A piece wise linear approximation of the response is expressed as

follows,

$$M(k) = \begin{cases} M^*(k) = EIk, & |k| < k_Y \\ M^{HS}(k) = \text{sign}(k)\left(M_i + \dfrac{M_{i+1} - M_i}{k_{i+1} - k_i}|k - k_Y|\right), & |k| \geq k_Y, |k| < k_F \\ M^F(k) = \text{sign}(k) M_F, & |k| \geq k_F \end{cases} \tag{2.28}$$

where I indicates the second moment of area of the pipe cross-section and the index i denotes the points of the curve discretisation. Following the point of failure, the model assumes that the bending moment is constant for increasing values of curvature. The complete flexural model, obtained combining the constitutive relation (2.28) with a kinematic hardening law, is reported in Appendix B.

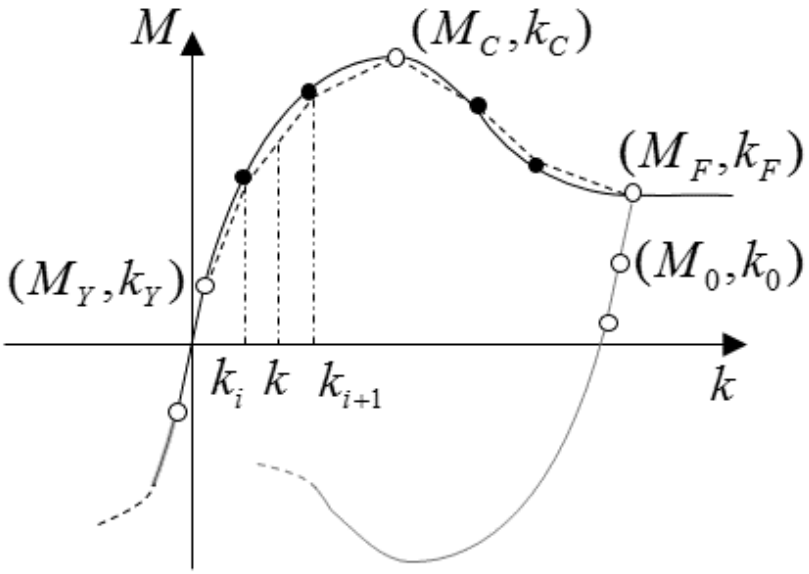

Figure 2.6: Schematics of the flexural constitutive model for the VUEL BM3D element code, as described in Listing B. The linear elastic region has been shortened for illustrative purposes.

2.4 VUEL BM2D architecture

The sequence of operations that compose the coding of the VUEL BM2D corotational user element for the in-plane bending of hollow beams is here presented.

At any increment, for each finite element, the explicit solution algorithm provides the current nodal coordinates (x_i, y_i), and the translational and rotational de-

grees of freedom associated with each node, u_i, v_i, θ_i, $i = 1,2$. The scope of the code is then to evaluate the internal force vector $\mathbf{f}$ and the mass matrix $\mathbf{M}$ necessary to solve Newton's equation and evaluate the state of the element at the end of the increment. The list of operations to be executed is summarised as follows:

1. Evaluate the initial and current element length, L, L_n, equation (2.4).
2. Evaluate the orientation β of the corotational frame, equation (2.6).
3. Compute the transformation matrix $\mathbf{B}$, equation (2.11).
4. Evaluate the local rotation angles, $\bar{\theta}_i$, equation (2.9).
5. Compute the local strains, equations (2.13), (2.18).
6. Apply the constitutive models, Section 2.3.
7. Assemble the local force vector $\bar{\mathbf{f}}$.
8. Obtain the global force vector $\mathbf{f} = \mathbf{B}^{\mathrm{T}}\bar{\mathbf{f}}$.
9. Build the mass matrix $\mathbf{M}$, equation (2.19).
10. Estimate the stable time increment, Δt, equation (2.23).

2.5 Numerical testing of circular pipes in bending

A series of numerical tests was performed in Abaqus/standard to simulate the bending of mild steel pipes, aimed at obtaining moment-curvature relations for a variety of cross-sectional dimensions. As previously discussed in Section 1.2.1, the deformation of a pipe in bending is a strongly non-linear problem due to the ovalization and eventual collapse of the cross section as the rotation increases. The Riks solution procedure [16] was chosen for its ability to simulate simultaneously geometric and material non-linearities. The Riks method assumes that the loading is quasi-static and proportional (that is, that the load magnitude and the displacement depend on a single scalar parameter, the arc length) and that the structural response

is reasonably smooth, without bifurcations. Under these conditions, finding the solution corresponds to finding the static equilibrium path in the load-displacement space as a function of the arc length. The Riks procedure, as it is implemented in Abaqus [16], employs the basic iterative Newton algorithm. The increment size is regulated by increments in the arc length, and is limited by moving a given distance on the load-displacement space along the line that is tangent to the current solution point and then searching for equilibrium in the plane that passes through the current point and is orthogonal to the tangent line.

Under the hypothesis of pure bending and the assumption that plane sections remain plane, the static collapse of a pipe in bending can be studied using a generalised plane strain model. The model asssumes that the strain is constant in the third direction, which is suitable for the analysis of the cross-section of slender structures that are subjected to axial loading [16].

Figure 2.7 (a) illustrates a unit length of a pipe bounded by two rigid walls. In the initial configuration, the bounding walls are parallel to each other and the pipe has no curvature. The prescription of a rotation between the two walls causes strain in the direction normal to the planes that varies linearly with respect to the in-plane position, which corresponds to a constant curvature. The pipe cross-section is

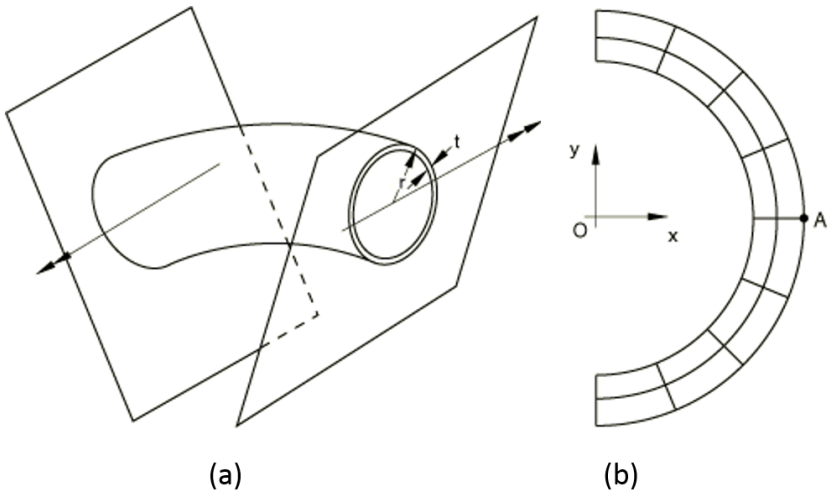

Figure 2.7: Simulation setup used for the numerical bending tests. (a) Boundary conditions and (b) example of discretisation of the cross-section with generalised plane-strain elements [16].

discretised using 4-nodes generalised plain strain elements with reduced integration (type CPEG4R) as in Figure 2.7 (b). The elements are allowed to distort in plane, and have an additional degree of freedom in the out-of-plane direction tied to the relative rotation of the walls with respect to the reference point A. Bending loading is obtained applying a prescribed rotation about the x-axis in point A, and symmetry conditions are prescribed along the y-axis. The motion of point A in the y-direction is fixed remove the possibility of rigid body motion in plane. The elements have aspect ratio 1, and a minimum of 6 elements is used along the thickness to correctly model the deformation of the cross-section.

The cross-sectional geometries considered are reported in Table 2.1. Several combinations of external diameter D and wall thickness H were analysed, based on the standards ASTM A312M, ASME B36.19M-2004, ASTM A106M and ASME B36.10M-2004. Mariotte's formula for cylinders under pressure allows to distinguish between thick and thin pipes through the ratio

$$\pi_C = \left.\frac{D}{H}\right|_C = 20\,. \tag{2.29}$$

When $D/H \leq 20$, a pipe is considered relatively thick, and an overall uniform ovalization in bending is expected. On the contrary, when $D/H > 20$ the pipe is considered thin, and it is expected to display a pronounced cross-sectional collapse. Of

Table 2.1: Typical values of outside diameter D and wall thickness H for stainless steel and carbon steel pipes, based on the standards ASTM A312M, ASME B36.19M-2004, ASTM A106M and ASME B36.10M-2004.

Pipe	Schedule	D (mm)	H (mm)	D/H
P1	Sch10	48.3	2.77	17.4
P2	Sch40	48.3	3.68	13.1
P3	Sch80	48.3	5.08	9.5
P4	Sch10	42.2	2.77	15.2
P5	Sch10	33.4	2.77	12.1
P6	Sch30	48.3	3.18	15.1
TP1	Sch5	48.3	1.65	29.3
TP2	Sch5	42.2	1.65	25.5

Table 2.2: Material properties used in the numerical bending tests on mild steel pipes [2].

ρ (kg/m^3)	E (GPa)	ν -	σ_Y (MPa)	a (MPa)	b (MPa)	n -
7850	200	0.33	295	266.1	530.5	0.5608

the pipes analysed, those labelled Pi, $i = 1,6$ in Table 2.1 are therefore considered thick, and those labelled TPi, $i = 1,2$ are considered thin.

The material considered was mild steel, following the experimental investigation of Reid et al. [2, 18], with the material properties reported in Table 2.2. Metal plasticity was modelled using the Johnson-Cook power law model

$$\bar{\sigma} = a + b\bar{\varepsilon}^n . \tag{2.30}$$

The disadvantage of the Riks method is its inability to model strain-rate dependent material behaviours; any numerical results can only be compared to static or quasi-static experimental data. Future studies, aimed at obtaining rate dependent moment-curvature relations, must therefore use a dynamic solution procedure.

The results of a mesh convergence study for the numerical bending test of a thick pipe (P1) using the Riks method are shown in Figure 2.8, where the curvature and the bending moment calculated on the cross-section are plotted against the number of elements in the direction of the thickness.

The cross-sectional deformation of the pipes P1 and TP1 is shown in Figure 2.9. Despite the small difference in wall thickness, the pipes display completely different behaviours when subjected to the same loading, with the geometry TP1 exhibiting a noticeable collapse.

2.5.1 Moment-curvature master curve

The moment-curvature relations extracted from the simulation of bending tests are displayed in Figure 2.10. The moment was extracted by integrating the stresses acting in the third direction on the cross-section, whereas the curvature is obtained from the relative rotation of the bounding planes. The differences between the several curves are dictated by the position of the yield and maximum points, which

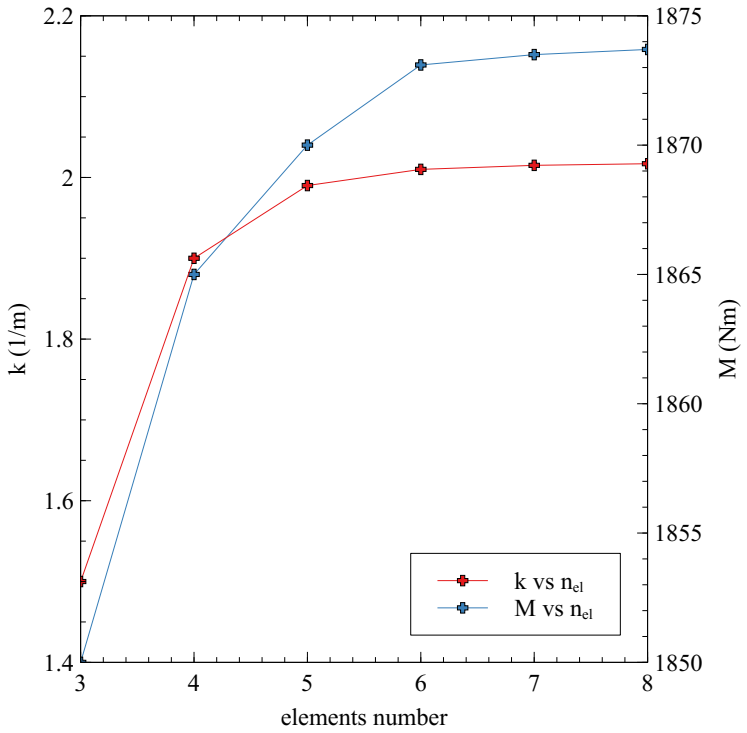

Figure 2.8: Mesh convergence study of a thick pipe (P1) in bending using the Riks procedure. Plots of curvature k (left axis) and bending moment M (right axis) against the number of element along the thickness.

determine the length of the hardening region. The curves obtained from thick pipes, labelled Pi, are characterised by an extended hardening region, followed by negligible softening, whereas the curves for thin pipes, labelled TPi, are distinguished by a short hardening region, followed by a lengthy softening branch.

The curves in Figure 2.10 show that the moment-curvature curve is not monotonically related to the ratio D/H. The curves P4 and P6, despite having similar values of the ratio, have very different values of yielding and maximum bending moment. The curves P5 and TP2, with $D/H = 12.1$ and 25.5, respectively, have almost overlapping hardening regions. Therefore, a dimensional analysis using Buckingham's theorem was performed to identify the parameters affecting the shape of the moment-curvature curves. It was found that the flexural behaviour of the pipes

Figure 2.9: Numerical predictions of cross-sectional collapse for a thick pipe (a) and a thin pipe (b), corresponding respectively to the cases P1 and TP1 reported in Table 2.1. The initial undeformed cross-sections are shown on top, and deformed cross-section at the bottom.

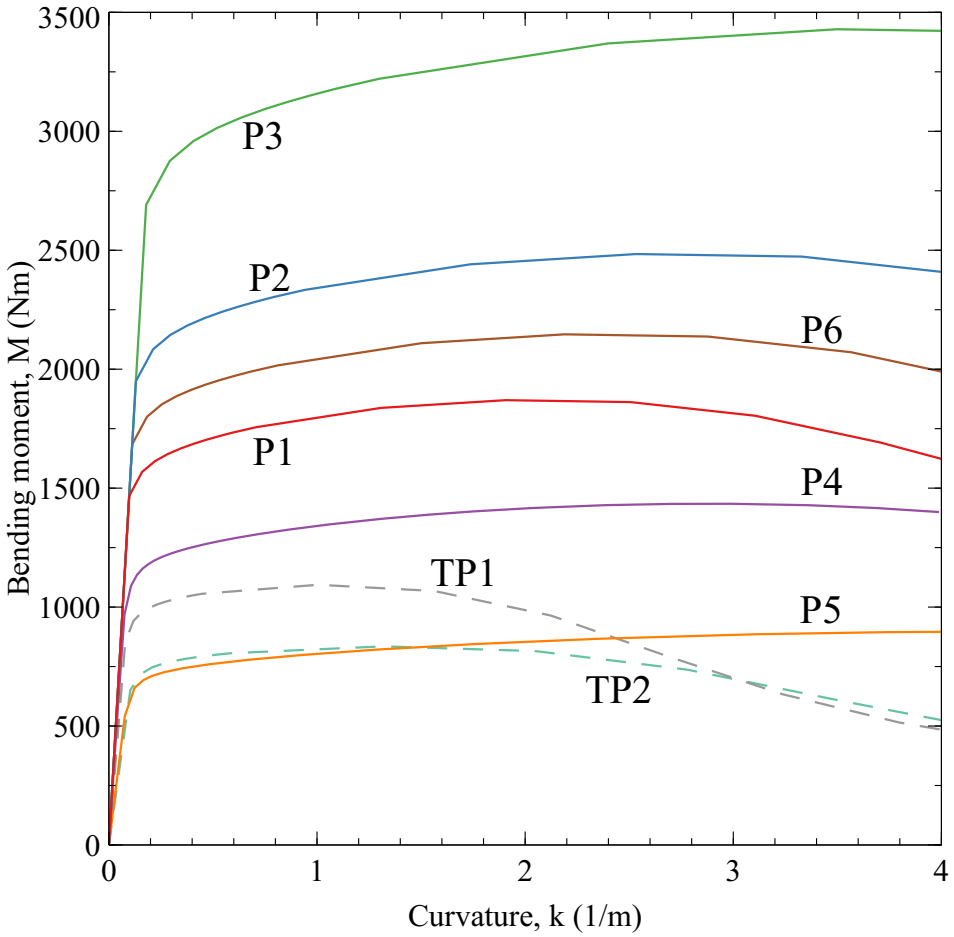

Figure 2.10: Bending moment-curvature relations from the numerical bending tests on mild steel pipes. Solid lines indicate thick pipes (labelled P*i*) and dashed lines indicate thin pipes (labelled TP*i*). The cross-sectional geometries are reported in Table 2.1.

is completely identified by three dimensionless groups

$$\pi_1 = \frac{D}{H}, \tag{2.31a}$$

$$\pi_2 = \frac{M_c}{\sigma_Y H D^2}, \tag{2.31b}$$

$$\pi_3 = \frac{k_c D^2}{H} \tag{2.31c}$$

where the parameters M_c and k_c identify the maximum point in the M-k curves. By inverting the relations (2.31), the two parameters can be expressed as a function of

just one material constant and two dimensions:

$$M_c = M_c\left(\sigma_Y, D, H\right), \tag{2.32a}$$

$$k_c = k_c\left(\sigma_Y, D, H\right). \tag{2.32b}$$

Manipulating the M-k curves of Figure 2.10 with the dimensional groups π_2 and π_3, it is possible to obtain relations of dimensionless moment, $M/(\sigma_Y H D^2)$, versus dimensionless curvature, kD^2/H, as shown in Figure 2.11. It can be seen that the dimensionless curves tend to overlap in the elastic and hardening phase, up to the maximum point. Beyond this point, two different behaviours can be distin-

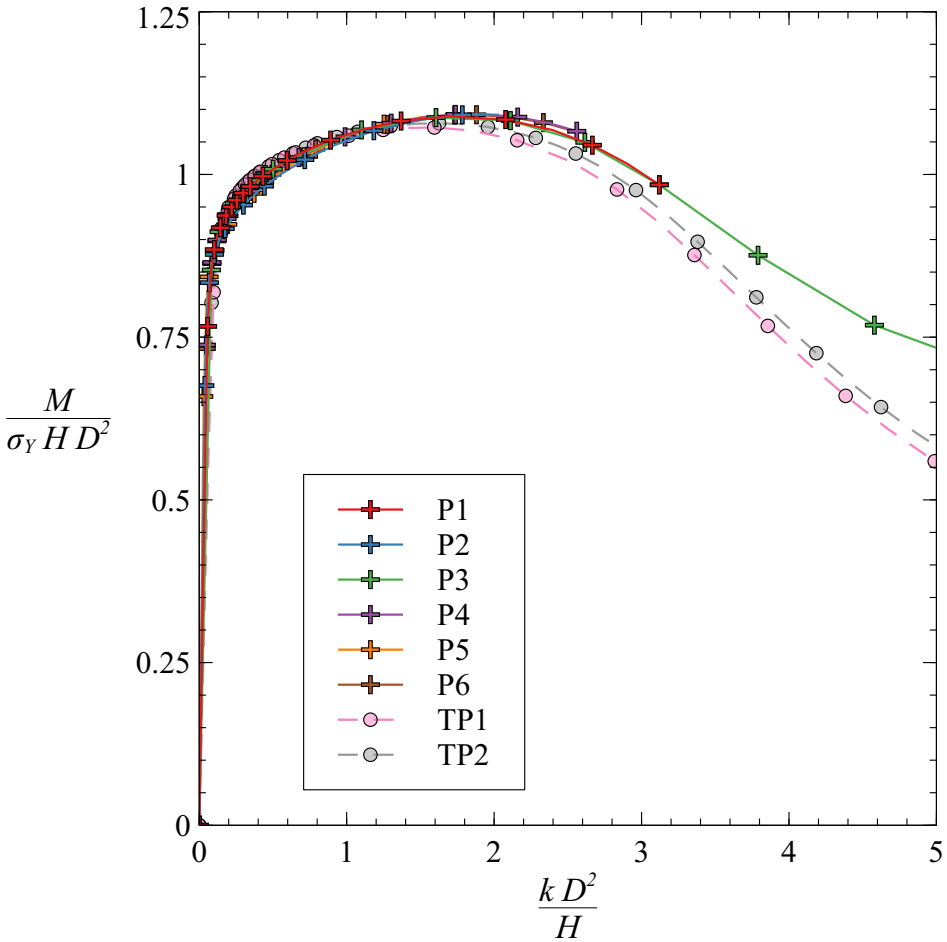

Figure 2.11: Dimensionless moment-curvature relations from the numerical bending tests on mild steel pipes. Solid lines indicate thick pipes (labelled P*i*) and dashed lines indicate thin pipes (labelled TP*i*). The cross-sectional geometries are reported in Table 2.1.

guished, where thin pipes exhibit a more pronounced softening phase compared to thick pipes. Based on these observations, two characteristic curves are defined, here named master curves, illustrated in Figure 2.12. Being defined in dimensionless units, the master curves do not depend on the yield strength or the cross-sectional dimensions, and can be used to univocally represent the response of think and thin pipes in the dimensionless space of $M/(\sigma_Y HD^2)$ versus kD^2/H.

To the best of the author's knowledge, the definition of the dimensionless groups π_2 and π_3 and of the master curves for describing the behaviour of pipes in bending have no precedents in the literature. The experimental investigation of Reid et al. [18] and Jialing and Reid [19] had confirmed that k_c is related to the

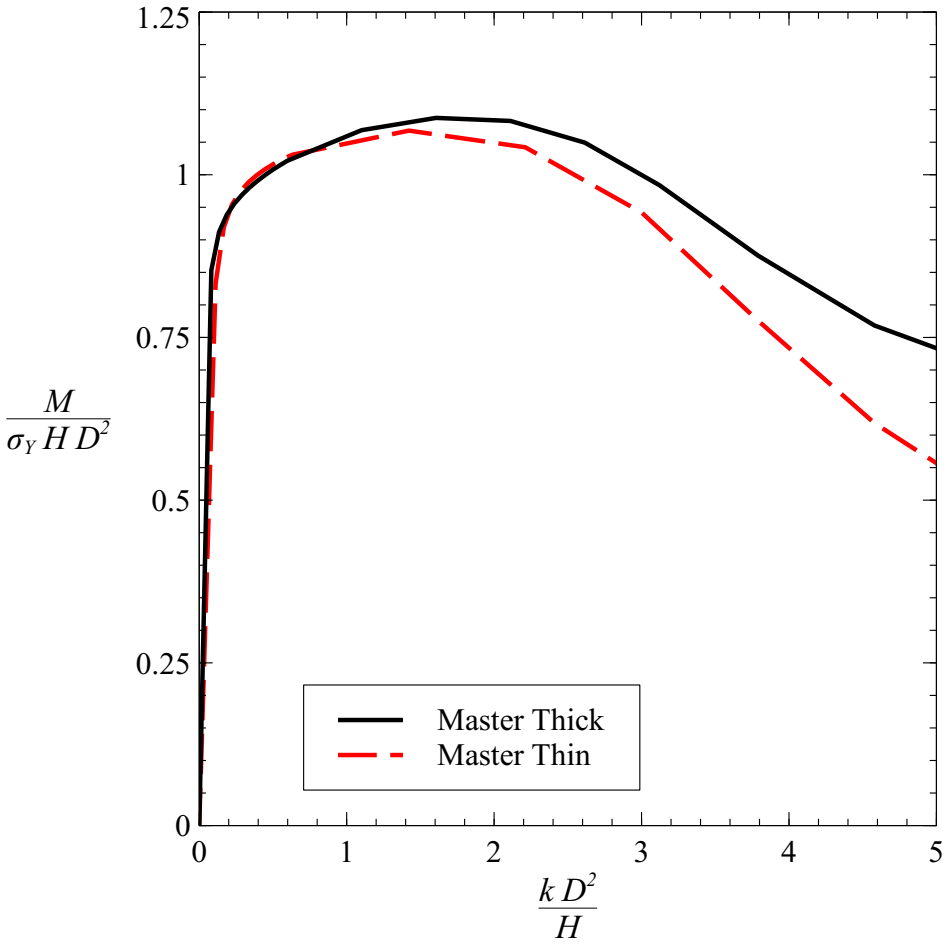

Figure 2.12: Dimensionless bending moment-curvature master curves for thick (—) and thin (– -) pipes obtained from numerical testing.

cross-sectional dimensions through the formula

$$k_c = 0.2\text{–}0.5\frac{H}{R^2} \tag{2.33}$$

where R is the mean radius. Further experiments [2] had evidenced the difference in behaviour between thick and thin pipes, and considerable effort was spent trying to predict the moment-curvature relations trough analytical [18] or numerical means [21, 80]. However, the studies concluded that, for each combination of D and H, ad hoc experimental or numerical bending tests needed to be carried out to obtain a moment-curvature relationship. The dimensional analysis here presented contests the aforementioned claim, showing that the behaviour of thick and thin pipes in bending can by described using the two characteristic master curves defined in the dimensionless moment-curvature space.

From the master curves, the M-k curves necessary for the use of the VUEL BM2D element can be obtained multiplying the dimensionless moment and curvature by the appropriate values of σ_Y, D and H. In Figure 2.13, the M-k curves obtained for mild steel pipes with the dimensions reported in Table 2.3 are compared with the experimental curves obtained from four-point bending tests by Reid et al. [2]. In the case of the thickest pipe ($D/H = 20$), the curves obtained numerically (– –) and experimentally (—) display overlapping elastic regions; however, there is a considerable difference in the value of yield moment (45%) and maximum moment (10%). It must be noted that the experimental test reports a noticeably small yield moment which is 21% smaller than that predicted theoretically

$$M_Y = \frac{\sigma_Y \pi}{4R_{\text{ext}}}\left(R_{\text{ext}}^4 - R_{\text{int}}^4\right) = 1332 \text{ MPa} \tag{2.34}$$

where R_{ext} and R_{int} are the external and internal pipe radius, respectively. In a subsequent study [21], Reid and Yang reported that the yield moment should coincide with that predicted by equation (2.34), and that the maximum bending moment, M_c, should only be slightly smaller than the fully plastic moment. No explanation was given in [2] and [21] for the significant deviation from the theory they observed for

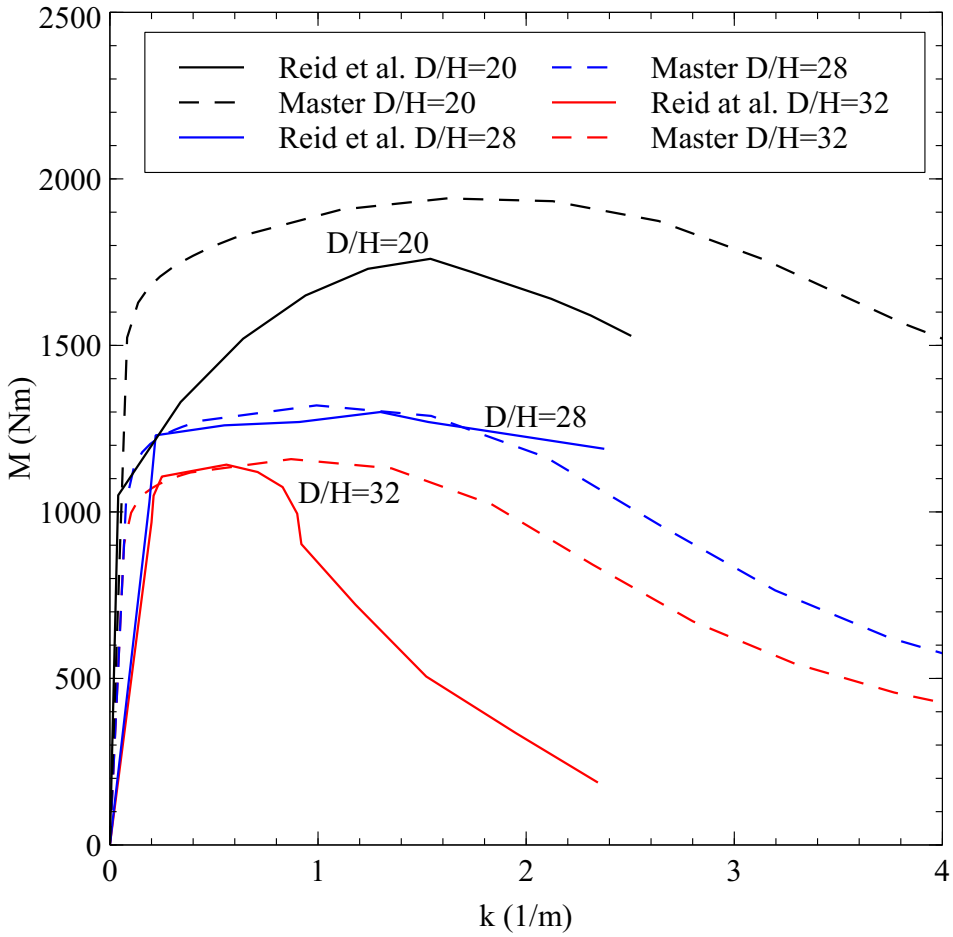

Figure 2.13: Comparison of the numerical *M*-*k* curves for mild steel (– –) with those obtained from four-point bending tests (—) by Reid et al. [2].

the thick pipe ($D/H = 20$).

On a different note, in the case of the thin pipes ($D/H = 28$ and 32) the experiments observed a much lower slope in the elastic region compared to that predicted numerically, which instead coincides with that predicted theoretically, given by

$$EI = E\frac{\pi}{4}\left(R_{\text{ext}}^4 - R_{\text{int}}^4\right) . \tag{2.35}$$

Reid et al. [2] did not give an explanation for this discrepancy. It must be noted from Reid et al. [18] that four-point bending test was altered to ensure that cross-sectional collapse would occur only at the mid-length. Two solid blocks were inserted in the tubes from the free ends up to the cross-sections where the external loads were applied. This approach ensured that collapse would not occur between the free ends

Table 2.3: Cross-sectional dimensions of the mild steel pipes investigated by Reid et al. [2].

D/H	D (mm)	H (mm)
20	50.8	2.60
28	50.8	1.80
32	50.8	1.58

and the loading points [18], but undoubtedly altered the rigidity of the system in the elastic phase. Beyond the elastic region, a good agreement is observed between the predicted and measured values of maximum bending moment, with an error of less than 1.5% for both geometries.

In light of the comparison with the experimental measurements, it is advisable to perform additional bending experiments on pipes to better characterise the flexural behaviour. In the next chapter, where the VUEL BM2D code will be used in the simulation of pipe whips, the experimental curve obtained by Reid et al. [2] for thick pipes ($D/H = 20$) will be adopted when modelling a pipe of the same dimensions, whereas numerical curves obtained for the master curves here developed will be adopted in the modelling of thin pipes.

2.6 Summary

This chapter has presented the development of a corotational beam element, VUEL BM2D, for the numerical analysis of in-plane pipe whips. The VUEL BM2D element employs a constitutive model for the description of the flexural behaviour of thin-walled pipes in bending, implemented as a moment-curvature relation. The element code is based on a corotational kinematic description, to ensure the algorithm has a reduced computational cost.

Numerical experiments of pipes in bending were performed to collect the data necessary for building the flexural constitutive model. A parametric analysis helped to define three dimensionless groups, equation (2.31), that completely identify the flexural behaviour, leading to the definition of dimensionless master M-k curves for thick and thin pipes. To the best of the author's knowledge, the dimensionless groups found and the master curves have no prior mention in the literature; these

novel findings allow to effectively describe the flexural behaviour of steel pipes with few commonly available parameters and, offering an approach that is readily implementable for industrial applications.

Chapter 3

Simulation of in-plane pipe whips

3.1 Introduction

Numerical analyses reproducing the pipe whip experiments performed by Reid et al. [2] are used herein for the validation of the VUEL BM2D code developed in Section 2.4. The validated code is then employed in parametric studies investigating the effect of the pipe geometry and blow-out force intensity on the deformation mechanisms of pipe whips. The results are compared against a theoretical model proposed by Stronge and Yu [8] for the prediction of the formation of plastic hinges, and against numerical prediction obtained from simulations performed in Abaqus/-explicit using shell elements.

3.2 Validation of the VUEL BM2D code

A schematisation of the experimental apparatus used by Reid et al. [2] for testing the flexural behaviour of in-plane pipe whips, presented in Section 1.2.1, is illustrated in Figure 3.1. A straight pipe is connected at one end to a pressure reservoir, and its free end terminates with a 90° elbow flange. The flange is initially occluded by a membrane which is suddenly ruptured by an explosive charge. The release of the high-pressure fluid induces an intense force that acts orthogonally to the longitudinal axis, causing it to deform in a vertical plane.

The initial intensity of the force is determined by the internal cross-section of the pipe and the fluid pressure. The intensity then gradually decreases during the motion of the pipe due to its progressive collapse.

In the numerical model aimed at reproduce the experimental apparatus, the pipe is discretised as a cantilever beam with a concentrated mass at its tip that approximates that of the flange. The connection to the pressure reservoir is modelled with fully constrained boundary conditions, and the blow-down force exerted by the escaping fluid is reproduced as a follower force concentrated on the free end of the beam. The loading intensity varies over time following the force pulse shown in Figure 3.2 that reproduces the experimental observations measured from pressure transducers [2].

The simulations were carried out in Abaqus/explicit using VUEL BM2D elements. Mesh convergence study were performed, based on measurements of the maximum displacement of the free end, demonstrating that a discretisation of the pipe with 20 elements was sufficient to capture the deformation of the pipes with a maximum error of 2% with respect to the reference solution obtained with 100 elements.

The model was used in the simulations of two pipe geometries, as reported in Table 3.1, where D is the external diameter, H the wall thickness, L the pipe length, F_0 the initial force intensity, and m the mass of the flange. The pipes were made of mild steel, with the material properties reported in Table 3.2, where ρ is the density,

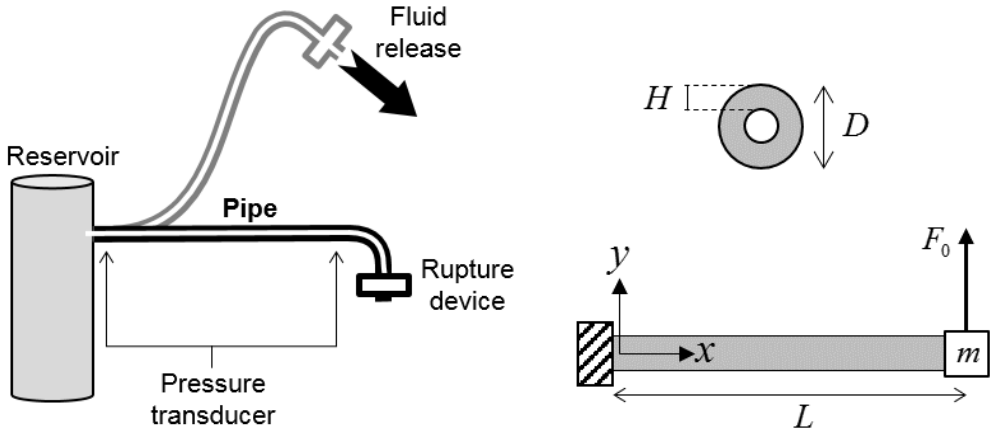

Figure 3.1: Schematisation of the experimental apparatus used by Reid et al. [2] for testing in-plane pipe whips (left), and simulation setup of the FE model reproducing the experiment (right).

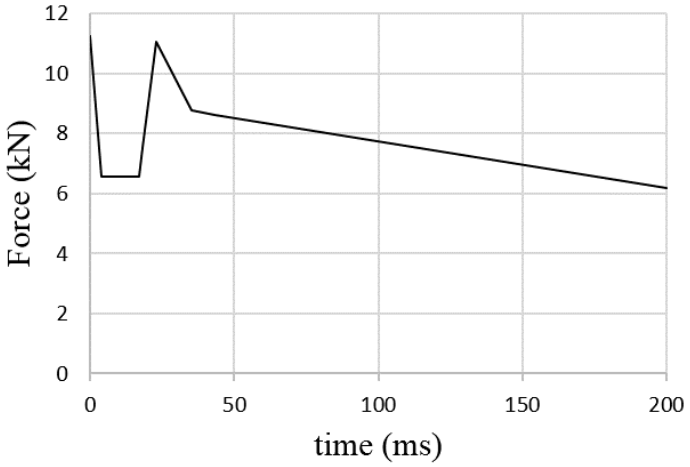

Figure 3.2: Blow-down force pulse measured by Reid et al. [2] in the test of in-plane pipe whips.

Table 3.1: Values of pipe dimensions, initial force intensity and flange mass used in the experimental tests on in-plane pipe whips performed by Reid et al. [2].

Test case	D (mm)	H (mm)	D/H -	L (m)	F_0 (kN)	m (kg)
$V1$	50.8	2.60	19.5	3.00	11.25	1.80
$V2$	50.8	1.58	32.2	2.73	11.25	1.04

Table 3.2: Material properties for mild steel, as reported by Reid et al. [2], used in the modelling of in-plane pipe whips.

ρ (kg/m^3)	E (GPa)	ν -	σ_Y^{nom} (MPa)	σ_U^{nom} (MPa)	$\varepsilon_U^{\text{nom}}$ -
7850	200	0.33	279	393	0.17

E the elastic modulus, ν is Poisson's ratio, σ_Y^{nom} the nominal yield stress, σ_U^{nom} the ultimate stress and $\varepsilon_U^{\text{nom}}$ the corresponding strain.

Metal plasticity is modelled in the simulation following the approach described in Section 2.3.1; the strain-hardening behaviour is included in the analysis as tabular data discretising the plastic stress-strain curve of the material reported in Figure 3.3. Similarly, the constitutive relation between bending moment and curvature, which depends on the cross-sectional dimensions of each pipe, is included as tabular data discretising the M-k curves shown in Figure 3.4, following the approach presented in Section 2.3.2.

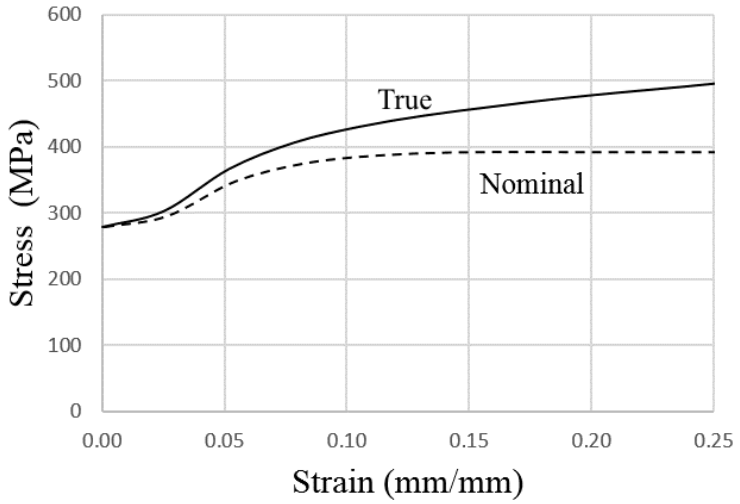

Figure 3.3: True plastic and nominal stress-strain curves from uniaxial tensile tests on mild steel [2] used in the simulation of pipe whips.

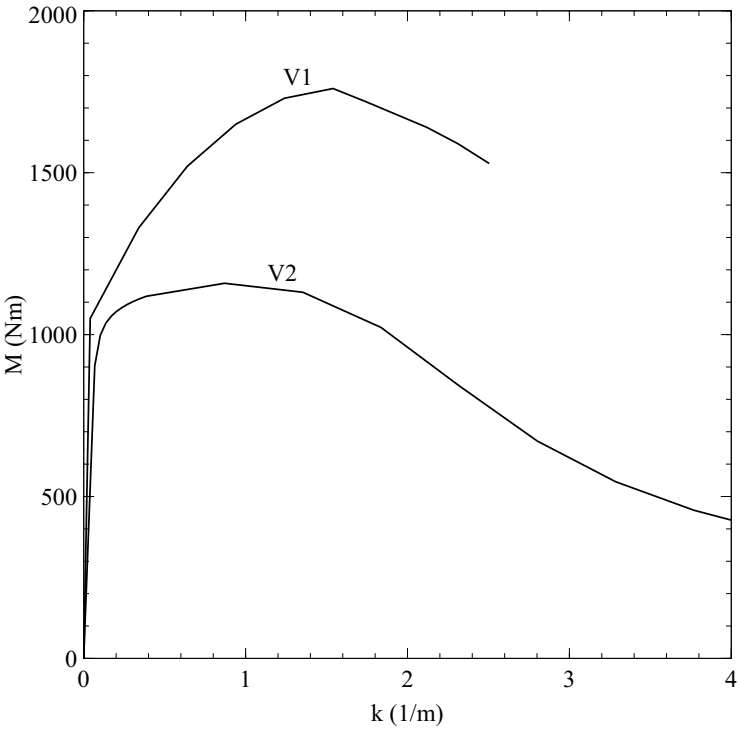

Figure 3.4: Moment-curvature curves used in the simulation of in-plane pipe whips. The cross-sectional dimensions are reported in Table 3.1.

Reid et al. [2] have observed that the axial stress due to bending developed during the deformation of the pipe was negligible with respect to the yield stress; therefore, the simulations can safely neglect the effect of strain-softening and the interaction between axial forces and bending moment. In the numerical study in [2], the effect of material strain-rate dependence was originally neglected; the same approximation is considered here, and the inclusion of the effect is programmed for future studies.

3.2.1 Thick pipe case

Figure 3.5 shows the deformation history of the relatively thick pipe of the test case $V1$ ($D/H = 19.5 < 20$) as predicted by the simulation using VUEL BM2D elements. The results are compared with the experimental (label Exp) and numerical (label Num) results of Reid et al. [2]. In the experiment, a high-speed camera was used to capture the instantaneous deflection of the pipe. Once the rupture device was activated, the pipe started bending instantaneously, with a motion that can be approximated with a rotation of part of the pipe about a point located at a distance of 1.5 m from the fixed end. Afterwards, the bending process progresses and the rotation point moves forward toward the fixed end. As stated in the experimental observations [2], the pipe undergoes continuous bending, and there is no discernible kinking of the pipe (i.e. localised cross-sectional collapse). Both numerical models predict well the instantaneous deformation profile of the pipe.

The maximum relative error for the position of the free end, between our simulation and the experimental data, is observed at the 60 ms time frame and is smaller than 3.5%. The agreement with the experimental data confirms that both numerical models are suitable for the simulation of large plastic deformation of thick-walled pipes. The VUEL BM2D simulation employs the same pulse defined in the original study [2] with which good agreement is observed. The small discrepancy in the deformation profiles between both numerical solutions and the experimental results at early time frames might be attributed to the approximation of the initial part of the force pulse.

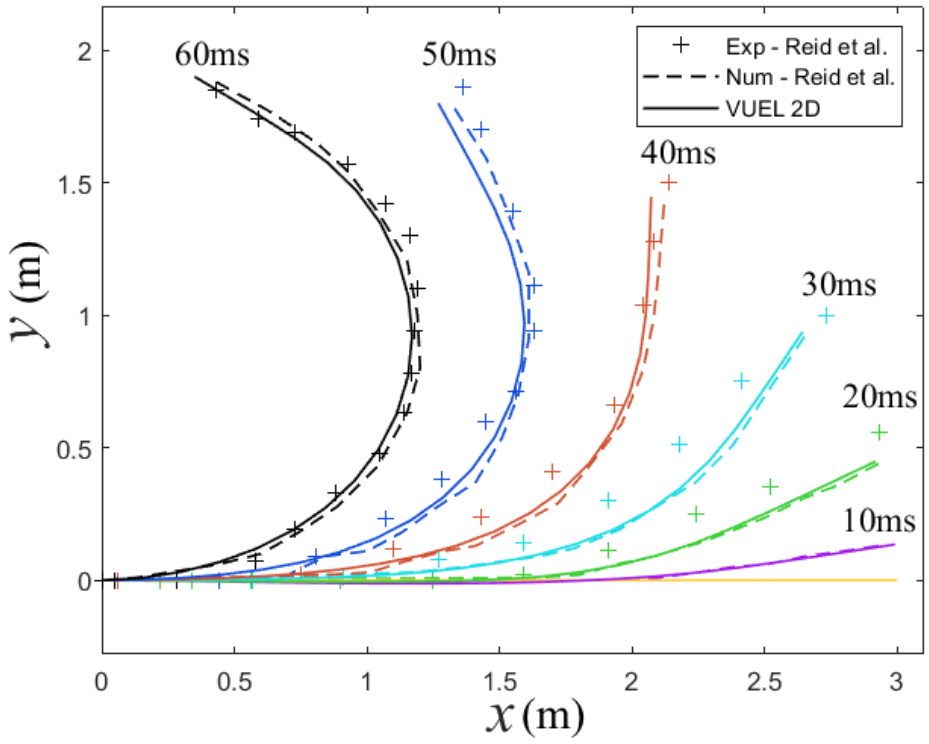

Figure 3.5: Deformed shapes of the pipe whip from the test case $V1$ at several time frames. The simulations results obtained with the VUEL BM2D element code are compared with the experimental results (Exp) and numerical predictions (Num) from Reid et al. [2].

3.2.2 Thin pipe case

The results of the study on the thin pipe of the test case $V2$ ($D/H = 32$) are presented in Figure 3.6. According to the experimental observations, this pipe demonstrated greater flexibility than the previous case. Most of the deformation was localised in a small region at $x \approx 1.7$ m, where complete cross-sectional collapse was observed starting at 30 ms. Subsequently, the deformation progresses with the rotation of the pipe about the fixed end.

A very similar behaviour was observed with the VUEL BM2D simulation. In the first 20 ms the pipe starts bending, with the centre of rotation located at $x \approx 1.7$ m. In the following time frames, the pipe continues to bend around this point, while a second centre of rotation forms at $x = 0$. In the last time frame, the pipe appears divided into an almost straight region, going from the free end to the first centre of rotation, a small curved region with an angle of about 90°, and a

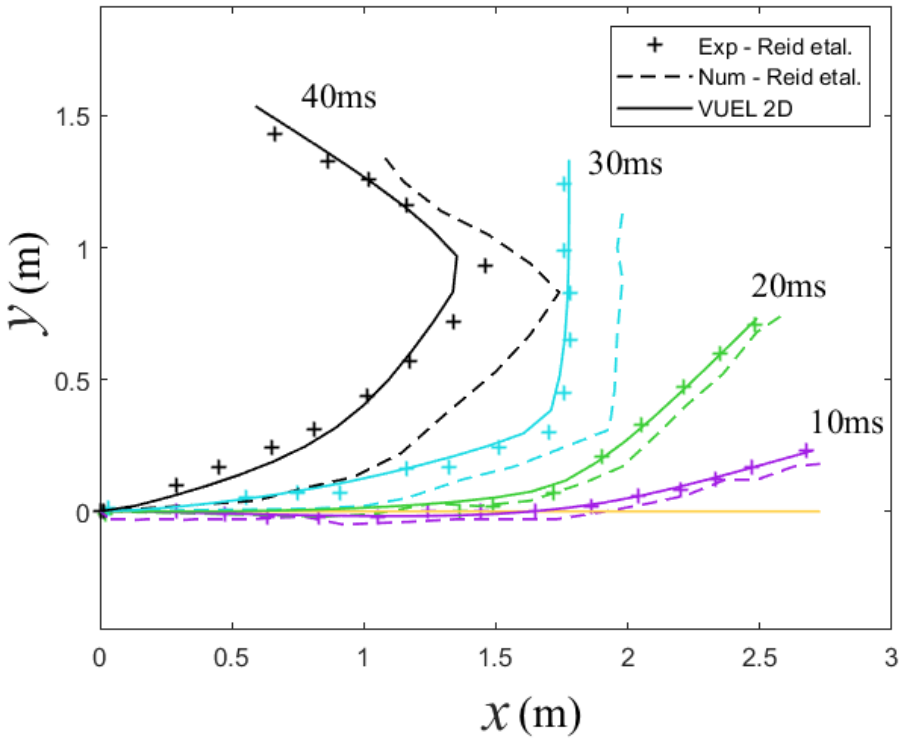

Figure 3.6: Deformed shapes of the pipe whip from the test case $V2$ at various time frames. The simulations results obtained with the VUEL BM2D element code are compared with the experimental results (Exp) and numerical predictions (Num) from Reid et al. [2].

final region of negligible curvature up to the fixed end. The comparison with the experimental measurements in Figure 3.6 shows that the VUEL BM2D simulation captures successfully the time point and the position where the localisation of the collapse mechanism occurs, and maximum relative error for the position of the free end measured the 40 ms time frame is smaller than 5%.

It must be noted that the numerical study by Reid et al. [2] predicts with less accuracy the evolution of the deformation profile. The localisation of the collapse mechanism is still predicted after 20 ms, but in a position that is much closer to the free end and the profile starts deviating significantly from that observed experimentally in the following time frames.

As previously mentioned, the current version of the element codes makes simplifying assumptions on the constitutive behaviour, neglecting the interaction between axial forces and bending moment, the hardening effect of strain-rate. An im-

provement on the model's predictive capabilities might be possible through the assumption of more comprehensive constitutive relations and an interactive yield surface. Nevertheless, small discrepancies between numerical and experimental results must be expected, remembering that, whilst experimental measurements taken from high-speed photograph encompass the whole pipe section, the numerical model is only capable of predicting the deformation of the pipe central axis.

3.2.3 Discussion

The agreement with the experimental data currently available confirms that the user element VUEL BM2D here developed is suitable for the large deformation analysis of thin-walled pipes.

The code is capable of accurately predicting the deformation profile of the pipes and the points of maximum curvature that correspond to localised mechanisms of cross-sectional collapse observed experimentally. In the following sections, the VUEL BM2D code will then be used in parametric studies aimed at analysing the effect of the pipe dimensions, the load intensity and the flange mass on the collapse mechanisms.

Currently, the element library of the FEA software Abaqus does not offer an equivalent element capable of modelling the pipe collapse in a dynamic analysis. An alternative strategy aimed at reach the same level of accuracy in Abaqus would require the use of shell of solid elements to discretise the whole geometry.

FE analyses that reproduced the pipe whip experiments employing the VUEL BM2D code, modelling the pipe with 20 elements, required a computation time of less than 1 minute, similar to that of analyses employing the standard beam elements available in Abaqus (Timoshenko element with two nodes), depending on the time increment chosen. In our simulations, a relatively small time increment was employed (0.02 times smaller than the stable time increment of a rigid rod, following equation (2.23)), to ensure stability of the solution even when softening in the moment-curvature relation occurs.

Two factors must be taken into account when considering in detail the computational cost of the user element. Firstly, at any increment the program's solver

calls an external subroutine, rather than an internal subroutine, and secondly, the code requires the writing of the requested element outputs in a dedicated comma-separated file for post processing. The first factor has a negligible effect on the overall computational cost, not directly dependent on the number of elements used, but that could increase significantly when reducing the time increment or when increasing the number of iterations. The latter factor has a predominant effect, due to the inherent cost of executing the Fortran input/output commands and the opening/closing commands directed to the results file at any increment. Despite these factors, the VUEL BM2D performs well compared to traditional beam elements, and even increasing the number of elements, the simulation time was of approximately 1 minute (computational cost of a simulation with 80 elements, and a total step time of 0.2 s).

3.3 Analytical plastic beam model

Stronge and Yu [8] proposed an analytical model for predicting the deformation mechanism of a rigid-perfectly plastic (RPP) cantilever beam with a concentrated force applied at its tip. The model is presented graphically in Figure 3.7, with a force that is initially oriented orthogonally to the beam's longitudinal axis and follows its rotation. Depending on the force intensity F, the beam exhibits three behaviours:

$$\begin{cases} F < F_C\,, & \text{stationary beam} \\ F \in [F_C, 3F_C]\,, & \text{Rotation about the fixed end} \\ F \geq 3F_C\,, & \text{Rotation about a plastic hinge}\,. \end{cases} \tag{3.1}$$

In the previous relations, $F_C = M_P/L$ is the plastic collapse force of a beam, which is determined by the beam length L and the plastic moment M_P of the cross-section. A dimensionless force can thus be defined as

$$f = \frac{F}{F_C}\,, \tag{3.2}$$

and the relations reduce respectively to $f < 1$, $f \in [1,3]$ and $f > 3$.

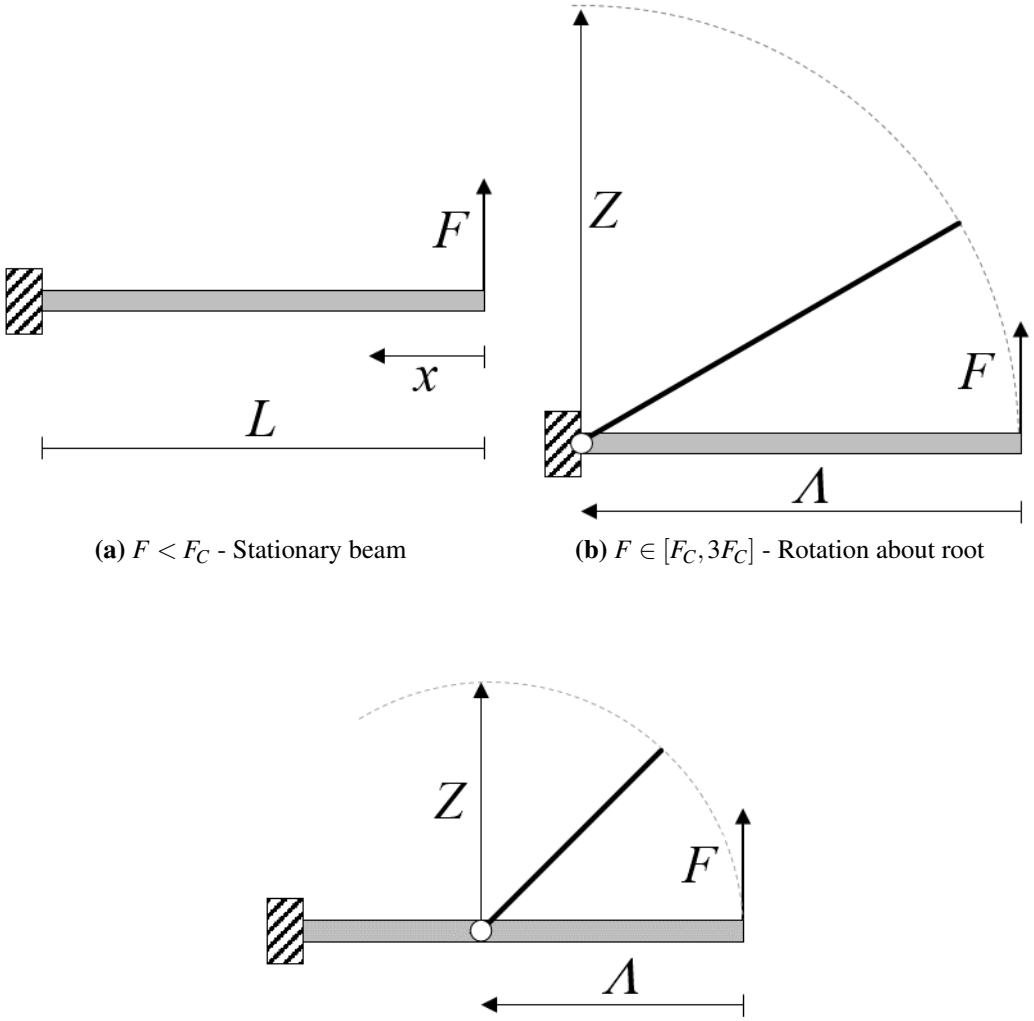

(a) $F < F_C$ - Stationary beam

(b) $F \in [F_C, 3F_C]$ - Rotation about root

(c) $F > 3F_C$ - Rotation about plastic hinge

Figure 3.7: Deformation mechanisms for plastic beams featured by the RPP model. Different mechanisms are predicted depending on the force intensity F. The hinge position Λ and the hazard zone Z are highlighted.

When $f > 1$ the beam deforms dynamically with a mechanism that is influenced by the loading intensity and pulse shape. By solving the translational and rotational equations of motion for the system of Figure 3.7, assuming that the force has constant intensity $F = F_0$, Stronge and Yu [8] demonstrated that a plastic hinge forms at a distance Λ from the beam free end that only depends on the loading

intensity

$$\Lambda = \frac{3}{F_0} F_C L, \tag{3.3}$$

or, in a dimensionless form

$$\lambda = \frac{\Lambda}{L} = \frac{3}{f_0}, \tag{3.4}$$

where $f_0 = F_0/F_C$. The simplicity of equation (3.3) stems from the approximation of the beam to a rigid-perfectly plastic body (thus neglecting elastic effect), and the reduction of the geometry to the longitudinal axis. Equation (3.4) implies that the plastic hinge develops at the fixed end ($\lambda = 1$) when $f_0 \leq 3$. Using the rigid-perfectly plastic model, the beam's hazard zone (i.e. the maximum extent of the area of influence of the pipe, indicated with Z in Figure 3.7) is completely determined by the hinge position Λ. When the beam rotates about the fixed end, the free end describes a circular arc of radius L. When a plastic hinge forms, the hazard zone has a smaller radius, which is approximated by the length Λ or, in dimensionless form

$$\zeta = \frac{Z}{L} \approx \lambda\,. \tag{3.5}$$

Solving the equations of motion for the case of a loading intensity that changes over time, $f = f(t)$, leads to [8]

$$\lambda = \frac{3\tau}{p(\tau)}, \tag{3.6}$$

where $\tau = t/t_0$ is the dimensionless time, t the time in seconds, $t_0 = L\sqrt{\rho/F_C}$ a characteristic time and $p(\tau)$ the pulse intensity

$$p = \int_0^\tau f(\tilde{\tau})\mathrm{d}\tilde{\tau}\,. \tag{3.7}$$

From equation (3.7) it can be deduced that, once formed, a plastic hinge will move towards either end of the beam with velocity

$$\dot{\lambda} = \frac{\mathrm{d}\lambda}{\mathrm{d}\tau} = \frac{3}{p(\tau)^2}[p(\tau) - \tau f(\tau)]\,. \tag{3.8}$$

The evolution of the tip force $f(\tau)$ determines the sign of $\dot{\lambda}$. The hinge will be stationary for $\dot{\lambda} = 0$, it will move towards the free end for $\dot{\lambda} < 0$ — when the loading decreases over time — and will move towards the fixed end for $\dot{\lambda} > 0$ — when the loading is increasing.

Stronge and Yu [8] further studied the RPP model in the case of a cantilever beam hit by a falling object of mass m. The study assumed the coefficient of restitution is null, that is, the mass would stay attached to the beam after the impact. Indicating with $\gamma = m/(\rho AL)$ its weight in dimensionless form, ρ the material density of the beam, A the cross-sectional area and v_0 its initial dimensionless velocity, solving the equation of motions leads to [8]

$$\lambda = \frac{1}{2\gamma v_0}\left(3\tau + \sqrt{9\tau^2 + 24\gamma^2 v_0 \tau}\right). \tag{3.9}$$

Stronge and Yu [8] did not investigate the case of beams that are loaded with a concentrated tip force and simultaneously hit by a travelling mass at the free end. The expansion of the RPP model to analyse this particular case is obtained below through the incorporation both effect into the equilibrium equations of the system. The translational and rotational equations of motion, in dimensionless form, of the system composed by a cantilever beam loaded ad its tip and and a mass travelling at speed v are

$$\begin{cases} \dfrac{1}{2}\lambda v = \gamma(v - v_0) + p\,, \\[2ex] \dfrac{1}{6}\lambda^2 v = \tau\,. \end{cases} \tag{3.10}$$

Solving the system of equations gives the hinge position $\lambda = (\tau, \gamma, v_0)$ as a function of time, the relative mass and initial velocity,

$$\lambda = \frac{1}{2(\gamma v_0 + p)}\left(3\tau + \sqrt{9\tau^2 + 24\gamma^2 v_0 \tau + 24\gamma p \tau}\right). \tag{3.11}$$

Substituting $v_0 = 0$ gives the hinge position for a cantilever beam loaded with a

concentrated force and an initially static mass at its tip

$$\lambda = \frac{1}{2p}\left(3\tau + \sqrt{9\tau^2 + 24\gamma p\tau}\right). \tag{3.12}$$

In the limit of $\tau \to 0$, equation (3.12) gives the initial hinge position

$$\lambda_0 = \frac{1}{2f_0}\left(3 + \sqrt{9 + 24\gamma f_0}\right). \tag{3.13}$$

The formulas above were here obtained for a generic pulse shape $p(\tau)$. The RPP model can be applied to the case of pipe whips, where the loading is generated by the sudden release of a jet of high pressure fluid. The intensity of the blow-out force is initially determined by the reservoir's pressure, and gradually decays over time as the pipe deforms. According to the experimental observations from [2], the force is extinguished when cross-sectional collapse causes the obstruction of the fluid flow, otherwise, the force decays to a stationary value. The works [2] and [8] suggest that in the case of pipe whips the force pulse can be substituted with a linearly decaying pulse of the type

$$f = \begin{cases} f_0\left(1 - \dfrac{\tau}{\tau_D}\right) & \tau < \tau_D, \\ 0 & \tau \geq \tau_D \end{cases} \tag{3.14}$$

where τ_D is the pulse duration in dimensionless unit. The pulse intensity then becomes

$$p = \begin{cases} f_0\tau\left(1 - \dfrac{\tau}{2\tau_D}\right) & \tau < \tau_D, \\ f_0\tau_D/2 & \tau \geq \tau_D. \end{cases} \tag{3.15}$$

Substituting the relations above in the formulas (3.6) and (3.12), it is possible to obtain an explicit expression for the variation of the hinge position over time in pipe whips

$$\lambda(\tau) = \frac{3}{f_0(1 - \tau/2\tau_D)}, \tag{3.16}$$

and in the case of a pipe with a concentrated tip mass

$$\lambda(\tau,\gamma) = \frac{3+\sqrt{9+24\gamma f_0(1-\tau/2\tau_D)}}{2f_0(1-\tau/2\tau_D)}. \tag{3.17}$$

The curves predicted by the models (3.16) and (3.17) are plotted in Figure 3.8 for a linearly decaying pulse. A pulse duration of $t_D = 0.68$ s ($\tau_D = 3.97$) was chosen to reflect the typical pulse duration observed in the experimental studies on pipe whips, as reported in [2]. In the figure, solid lines represent the hinge location predicted at $\tau = 0$, whereas dashed lines indicate the hinge position at $t = 0.2$ s ($\tau = 1.17$). The concentrated mass of $\gamma = 0.2$ was used, which corresponds to that of the pipe whip experiments from Reid et al. [2].

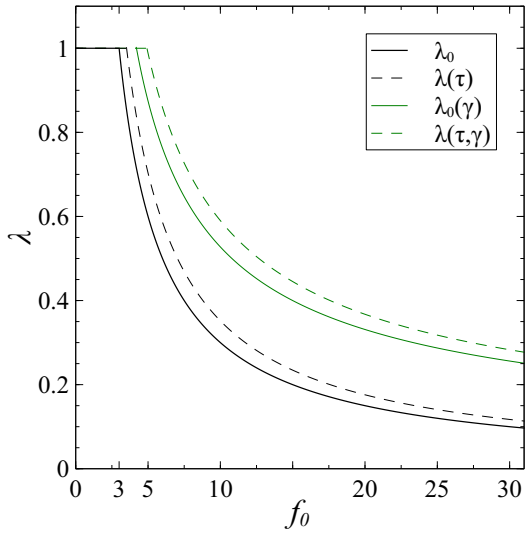

Figure 3.8: Theoretical predicitons of plastic hinge position, λ, for pipe whips subjected to a linearly decaying force pulse of initial intensity f_0. The black lines labelled λ_0 and $\lambda(\tau)$ indicate the hinge position at the time $t = 0.0$ s and 0.2 s, respectively. The green lines $\lambda_0(\gamma)$ and $\lambda(\tau,\gamma)$ indicate the response predicted at the same instants for pipe whips with a concentrated mass at the tip ($\gamma = 0.2$).

3.4 Parametric studies on pipe whips

The VUEL BM2D code is here employed to investigate the effect of the pipe geometry and load intensity on the dynamic response. The analytical RPP model shows that the dimensionless hazard zone, ζ, and plastic hinge location, λ, are expected to depend on two dimensionless groups: the loading intensity $f_0 = F_0 L/M_P$ and the

mass ratio $\gamma = m/(\rho AL)$. Assuming a linearly decaying pulse shape with $\tau_D = 3.97$, parametric studies were here conducted to analyse individually the effect exerted by the parameters F_0, L, m and M_P. In the simulations presented hereafter, the loading pulse is modelled with a linearly decaying force, as expressed by equation (3.14).

It was shown in Section 3.2 that a mesh of 20 beam elements is sufficient to capture successfully the free-end displacement of the pipe whips. However, a finer mesh of 80 elements is employed hereafter to analyse in more detail the location and extension of plastic hinges. As in the previous sections, the simulations were performed in Abaqus/explicit employing the VUEL BM2D elements. The elements employ the bending moment-curvature relationships obtained in Section 2.5 and validated in Section 3.2, and the same material properties there described.

The pipes have fully-constrained boundary conditions at the fixed end, referred to as the pipe's root, and are loaded at the opposite end, or tip, with a concentrated follower force that is initially orthogonal to the pipe's longitudinal axis, as previously depicted in Figure 3.7.

Hereafter, D will indicate the external diameter and H the wall thickness. For each cross-section, the plastic moment M_P is defined as [13, 7]

$$M_P = \frac{4}{3}\left[\left(\frac{D}{2}\right)^3 - \left(\frac{D}{2} - H\right)^3\right]\sigma_Y \alpha\,, \tag{3.18}$$

with

$$\alpha = \left(1 - \frac{\sigma_U}{\sigma_Y}\right)\frac{D}{80H} + \frac{\sigma_U}{\sigma_Y} \tag{3.19}$$

where α is a strain-hardening factor depending on the yield stress $\sigma_Y = 279$ MPa and the ultimate stress $\sigma_U = 392$ MPa.

3.4.1 Effect of load intensity and cross-sectional geometry

The first parametric study analyses the deformation of pipes with different combinations of cross-sectional dimensions subjected to linearly-decaying force pulses. The initial force intensity falls within the range $f_0 \in [3, 30]$. Three sets of cross-sectional dimensions were chosen, as reported in Table 3.3, to investigate the differ-

Table 3.3: Values of pipe dimensions, plastic moment and collapse force for the first parametric study on pipe whips, in which the load intensity varies in the range $f_0 \in [3, 30]$.

Test case	D (mm)	H (mm)	D/H	L (m)	M_P (kNm)	F_C (kN)
#1	50.8	2.60	20	3.00	0.220	0.733
#2	50.8	1.58	32	2.73	0.133	0.486
#3	508.0	12.70	40	10.0	1046	104.6

ent responses of thick and thin pipes. The first two sets of dimensions correspond to those of the pipe whips from the experimental investigation reported in [2]. The set of dimensions of the test case #3 corresponds to the typical dimensions of a pipeline employed for petrochemical applications [81].

The deformation profiles of the pipe whips, and their time history, are presented in Figure 3.9 and Figure 3.10. The dimensionless plots on the left-hand side correspond to thick pipes (test case #1), and on the right-hand side to thin pipes. Similar behaviours were observed between the test cases #2 and #3, therefore only the plots belonging to case #2 are reported. The reference frame is positioned on the initial position of the tip, which is located on the right-hand side of each plot.

As predicted by the RPP model, when $f_0 = 3$, the pipes rotate about the root and the hazard zone reaches the maximum range allowed, equal to the pipe length. When $f_0 > 3$, a different deformation mechanism is observed, which is interpreted with the formation of plastic hinges. In these cases, the deformation range is reduced and is comparable to the extent of hazard zone ζ as predicted using equation (3.5). Diverse mechanisms were observed numerically, depending on the loading intensity and the relative thickness of the pipe. In order of increasing load intensity they are:

Cantilever mode — when a stationary hinge develops at the root.

Double-hinge mode — when a plastic hinge develops along the pipe, followed by the formation of a secondary hinge at the root.

Triple-hinge mode — similar to the previous mode, characterised by the formation

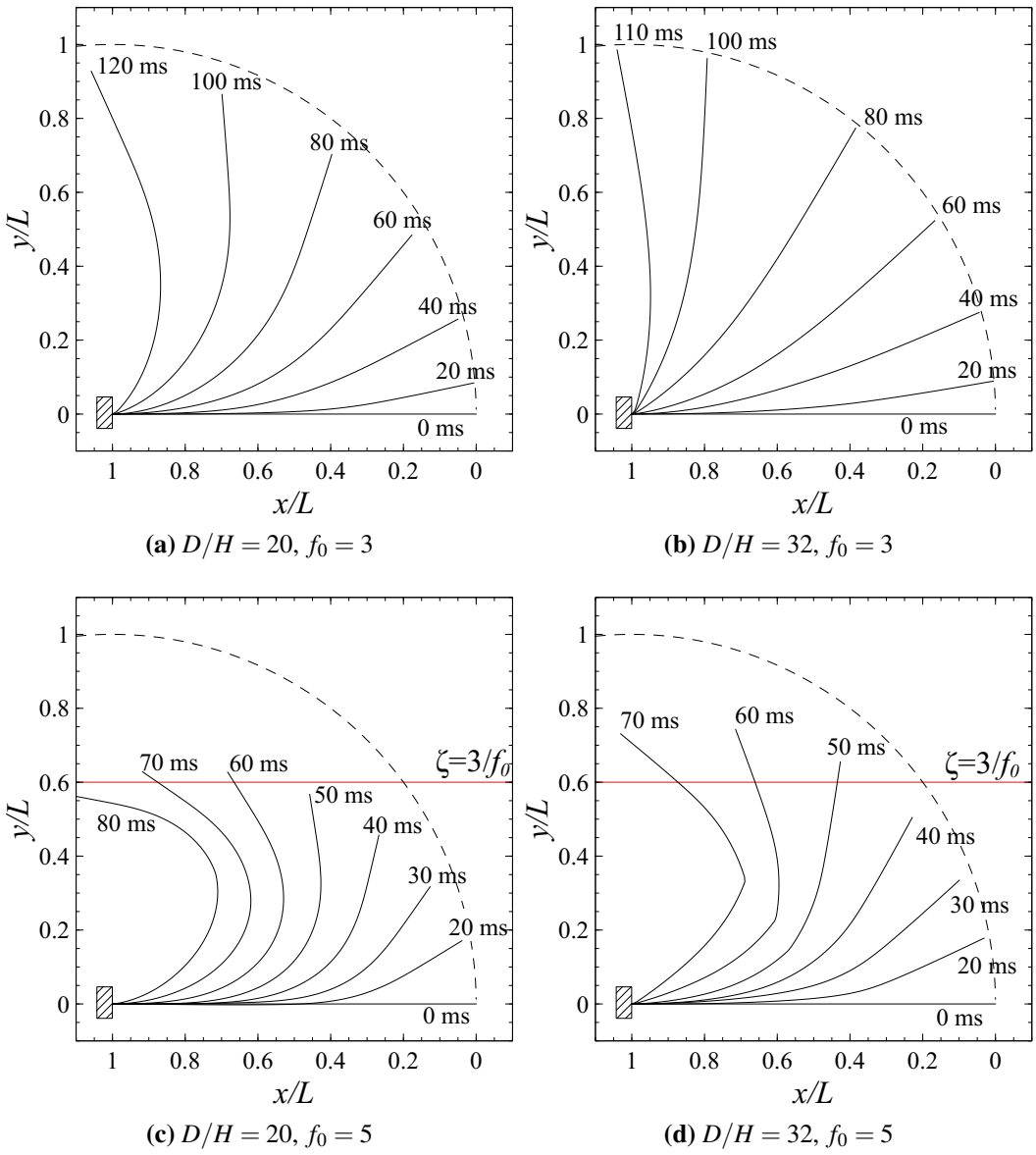

(a) $D/H = 20$, $f_0 = 3$ **(b)** $D/H = 32$, $f_0 = 3$

(c) $D/H = 20$, $f_0 = 5$ **(d)** $D/H = 32$, $f_0 = 5$

Figure 3.9: Deformation profiles of thick and thin pipe whips ($D/H = 20$ and 32, respectively), subjected to orthogonal follower forces of initial intensity $f_0 = 3$ (a, b) and 5 (c, d). The vertical displacement is compared with the hazard zone predicted by the RPP model, ζ. A circular arc with radius equal to the pipe length and centred in the fixed end is used to represent the maximum deformation range allowed.

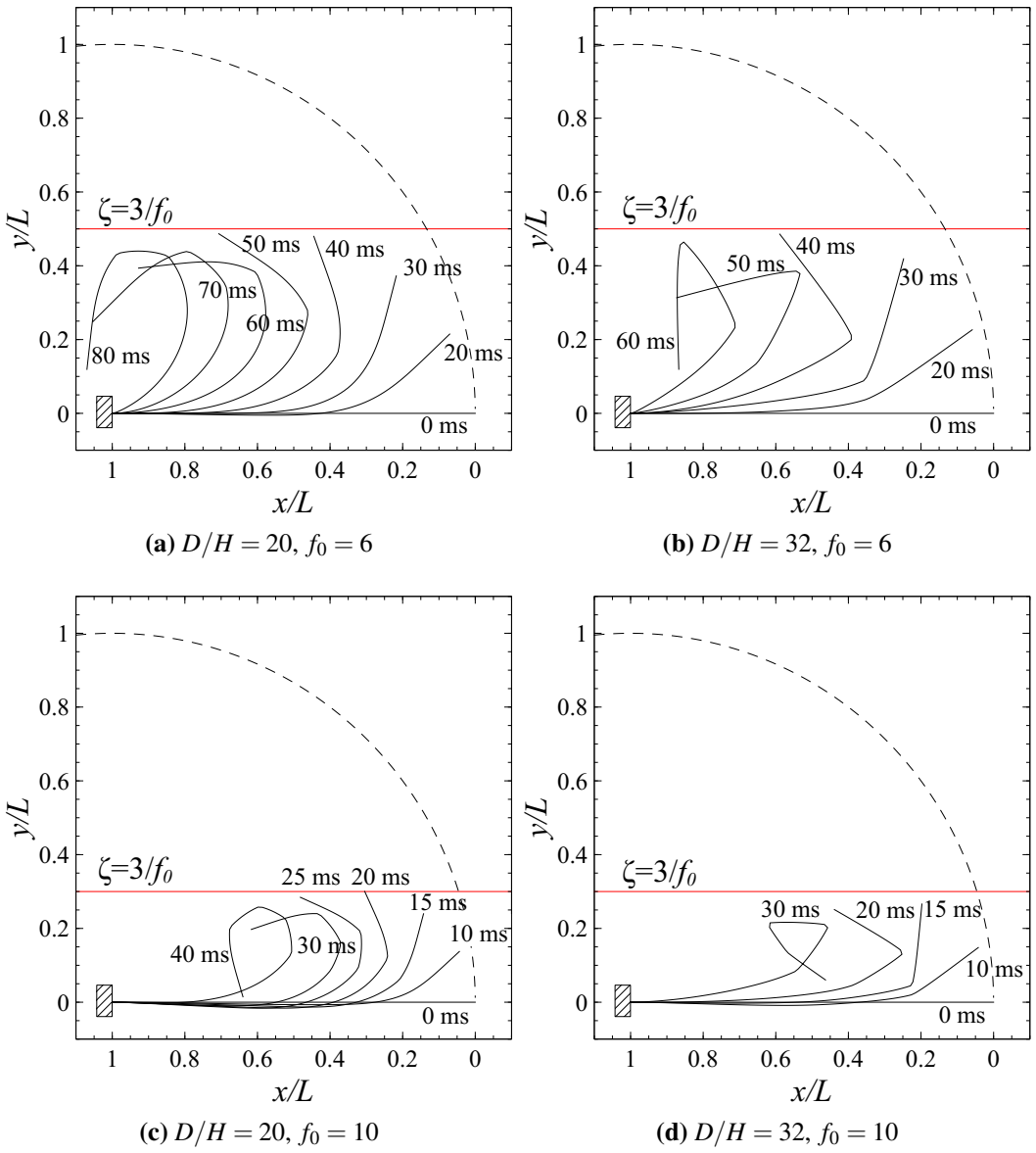

(a) $D/H = 20$, $f_0 = 6$ **(b)** $D/H = 32$, $f_0 = 6$

(c) $D/H = 20$, $f_0 = 10$ **(d)** $D/H = 32$, $f_0 = 10$

Figure 3.10: Deformation profiles of thick and thin pipe whips ($D/H = 20$ and 32, respectively), subjected to orthogonal forces of initial intensity $f_0 = 6$ (a, b) and 10 (c, d). The vertical displacement is compared with the hazard zone predicted by the RPP model, ζ. A circular arc with radius equal to the pipe length and centred in the fixed end is used to represent the maximum deformation range allowed.

of three plastic hinges, the last being formed at the root. This mechanism is observed only for thin pipes.

Self-intersecting mode — when the pipe collapses on itself forming a loop. Three or more plastic hinges develop along the pipe, but there is negligible rotation about the fixed end.

The last collapse mechanisms is of particular interest in the petrochemical field. Although a self-intersecting pipe produces a significantly reduced hazard zone (thus decreasing the probability of impacting with external bodies), the curvature is not always high enough to cause complete obstruction of the fluid flow [2, 18], leading to the uninterrupted release of the internal fluid, increasing the hazard of the system (e.g. temperature increase, release of chemicals, risk of explosion). When modelling the case of self-intersecting collapse, the simulation was stopped at the moment of self-contact, to avoid the use of a computationally expensive contact model. Loading intensities in the range $f_0 > 30$ are not considered here, as they are expected to cause deformations with a small hazard zone ($\zeta < 0.1$).

A more precise analysis of the formation and growth of plastic hinges is conducted by looking at the distribution of curvature along the pipe, as presented in Figure 3.11 and Figure 3.12. It can be seen that, for all values of f_0, the segment adjacent to the free end stays in elastic conditions throughout the simulation. After no more than 20 ms the remainder of the pipe starts deforming plastically, and the curvature goes above the yield value ($k_y/k_c = 0.03$ for thick pipes and $k_y/k_c = 0.08$ for thin pipes, according to the hardening-softening moment-curvature relation used, that was obtained in Section 2.5.1 and validated in Section 3.2). It is here assumed that plastic hinges form when the curvature exceeds the critical value $k/k_c \geq 1$.

Figure 3.11 (a) and (b) show that, for $f_0 = 3$, as the deformation progresses, a plastic hinge forms at the pipe's fixed end, in accordance to the *cantilever mode* identified in Figure 3.9 (a) and (b). As the force is increased ($f_0 = 5$), the *double hinge mode* is observed, with the first hinge forming at a distance $x/L \approx 0.5$ from the free end, and the second hinge forming at the root.

As the loading is increased further (Figure 3.12), we assist at the formation of

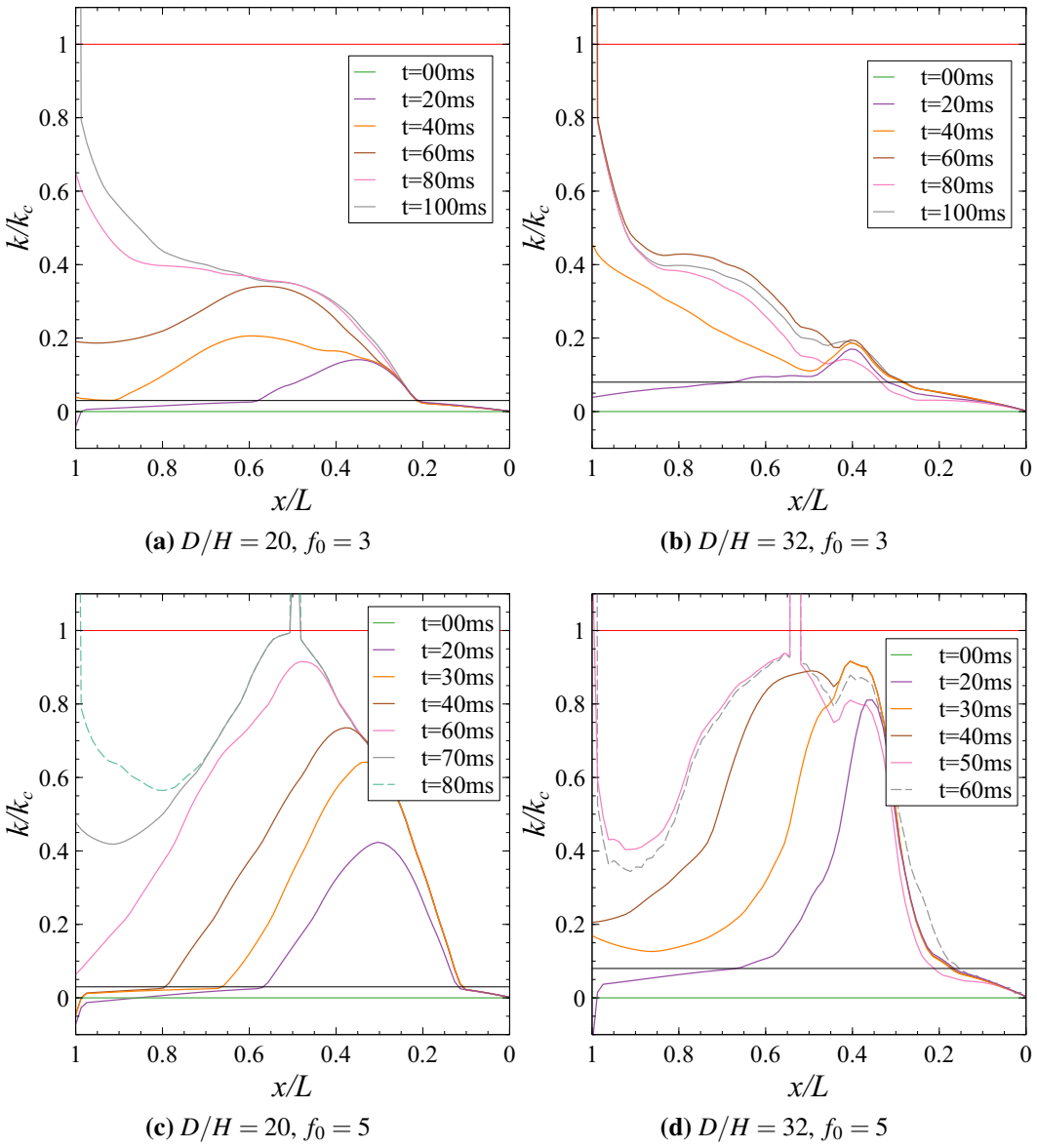

(a) $D/H = 20$, $f_0 = 3$ **(b)** $D/H = 32$, $f_0 = 3$

(c) $D/H = 20$, $f_0 = 5$ **(d)** $D/H = 32$, $f_0 = 5$

Figure 3.11: Time history of curvature distributions along the pipes, in dimensionless form, k/k_c, for loading intensity $f_0 = 3$ and 5. Black lines (—) indicate the yield point, red lines (—) indicate the critical point $k/k_c = 1$. Solid lines of different colours (—) indicate curvature distributions from the time $t = 0$ ms up to the moment of formation of a plastic hinge, and dashed lines (- -) are used in the following time frames.

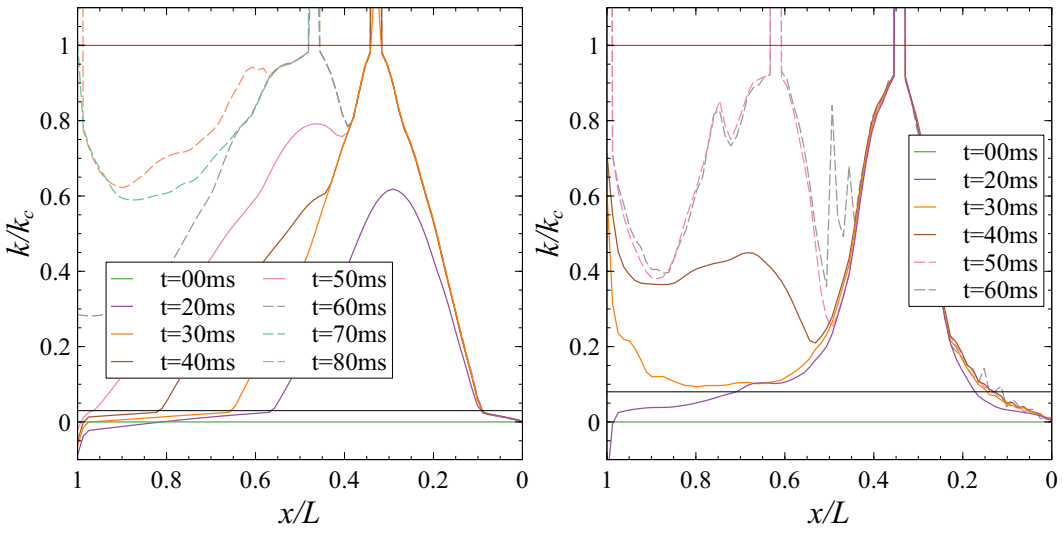

(a) $D/H = 20$, $f_0 = 6$ **(b)** $D/H = 32$, $f_0 = 6$

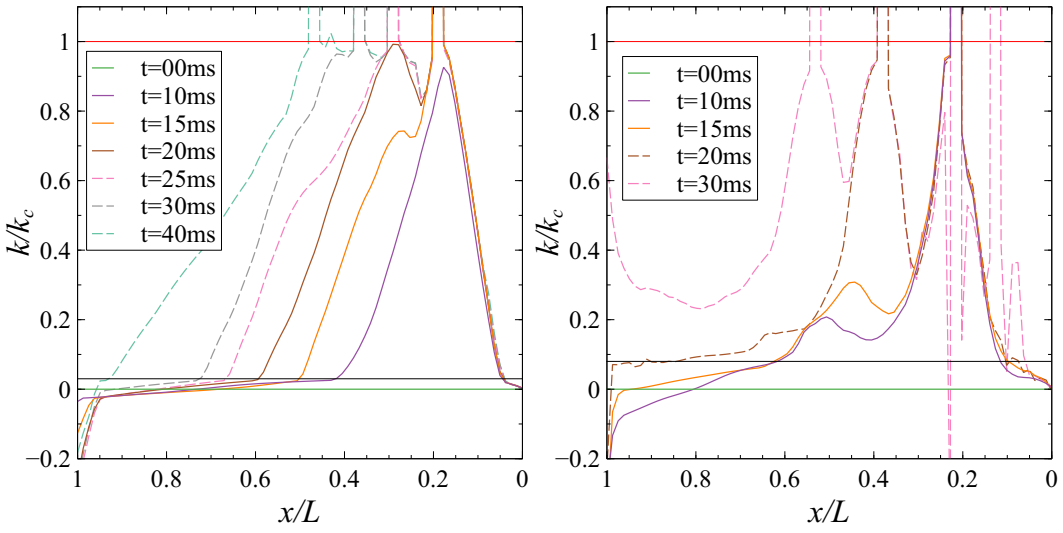

(c) $D/H = 20$, $f_0 = 10$ **(d)** $D/H = 32$, $f_0 = 10$

Figure 3.12: Time history of dimensionless curvature distribution along the pipes for loading intensity $f_0 = 6$ and 10. Black lines (—) indicate the yield point, red lines (—) indicate the critical point $k/k_c = 1$. Solid lines of different colours (—) indicate curvature distributions from the time $t = 0$ ms up to the moment of formation of a secondary plastic hinge, and dashed lines (- -) are used in the following time frames.

three or more hinges, eventually leading to the *self-intersecting* mode. Figure 3.12 (c) and (d) highlight a fundamental difference in the collapse mechanism of relatively thick and thin pipes. In Figure 3.12 (c) consecutive hinges are connected by regions with high levels of curvature, resulting in the formation of an extended plastic region, as observed in Figure 3.10 (c). In Figure 3.12 (d) plastic hinges are instead separated by regions of low curvature, resulting in the localised collapse mechanism of Figure 3.10 (d). These observations are coherent with what was observed experimentally in [2].

The two self-intersecting collapse mechanisms of Figure 3.10 (c) and (d) are schematically represented in Figure 3.13. We observe that thick pipes tend to collapse following the mechanism represented in Figure 3.13 (a). The mechanism takes place with the separation of the pipe in three sections: a relatively-straight elastic part at the free end, followed by a plastic region, followed by a section with low curvature. The plastic region is limited on either side by a plastic hinge (see Figure 3.12 (c)). Following a simple geometrical analysis, we determine that the dimensionless distance of the first plastic hinge from the tip, λ_1, falls in the range

$$\frac{1}{3} \leq \lambda_1^{\text{thick}} \leq \frac{\sqrt{3}}{2\pi}. \tag{3.20}$$

The self-intersecting deformation mode observed for thin pipes in Figure 3.10

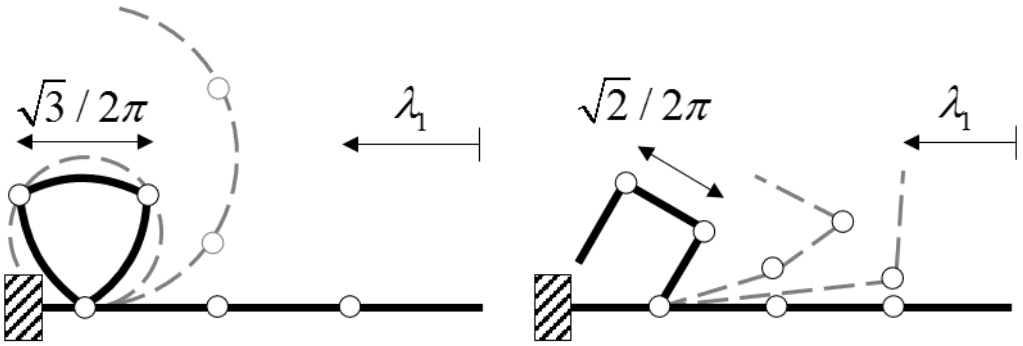

(a) $D/H \leq 20$ **(b)** $D/H > 20$

Figure 3.13: Schematic representation of self-intersecting collapse mechanisms for thick (a) and thin (b) pipe whips.

(d) is schematically represented in Figure 3.13 (b). Considering the curvature distributions in Figure 3.12 (d), it is observed that the collapse of thin pipes occurs with the sequential formation of several plastic hinges along the pipe, separated by relatively straight segments. Using a similar geometrical analysis, the following relationship is found

$$\frac{1}{4} \leq \lambda_1^{\text{thin}} \leq \frac{\sqrt{2}}{2\pi}. \tag{3.21}$$

Both relationships are in good agreement with the numerical observation from the parametric study.

The hinge position predicted by the RPP model at $t = 0$ s and $t = 0.2$ s (previously depicted in Figure 3.8 with λ_0 and $\lambda(\tau)$, respectively), are compared with the numerical predictions in Figure 3.14. Here, different symbols are used to point at primary (λ_1), secondary (λ_2) or tertiary (λ_3) plastic hinges, wherease error bars indicate the length of the plastic region that is observed in the case of thick pipes.

Figures 3.14 (a, b, c) show that the theoretical RPP model of equations (3.4) and (3.16) tends to over predict the λ_1 length, especially for the thick pipe. This phenomenon can be attributed to several causes. The RPP model allows rotation only at a single plastic hinge (a travelling hinge in the case of a decaying pulse), which is in disagreement with the observation of multiple hinges and extended plastic regions obtained numerically and from previous experiments [2, 18]. Furthermore, the RPP model fails to take into account elastic effects. Nevertheless, the RPP model is in excellent agreement with numerical predictions for the extent of the hazard zone, ζ, as reported in Figure 3.14 (d) and previously observed in Figures 3.9 and 3.10.

The grey bands in Figures 3.14 (a, b, c) corresponds to the geometrical criteria (3.20) and (3.21) for the initiation of the self-intersecting mode. In the case of thick pipes, the phenomenon first occurs for $f_0 = 7$, when the measured hinge position is $\lambda_1 = 0.29 \approx \sqrt{3}/(2\pi)$. A transition between double-hinge mode and self-intersection occurs for $f_0 = 6$ with $\lambda_1 = 0.32 \approx 1/3$. For thin pipes, self-intersection first occurs at $f_0 = 9$ with $\lambda_1 = 0.24 \approx \sqrt{3}/(2\pi)$.

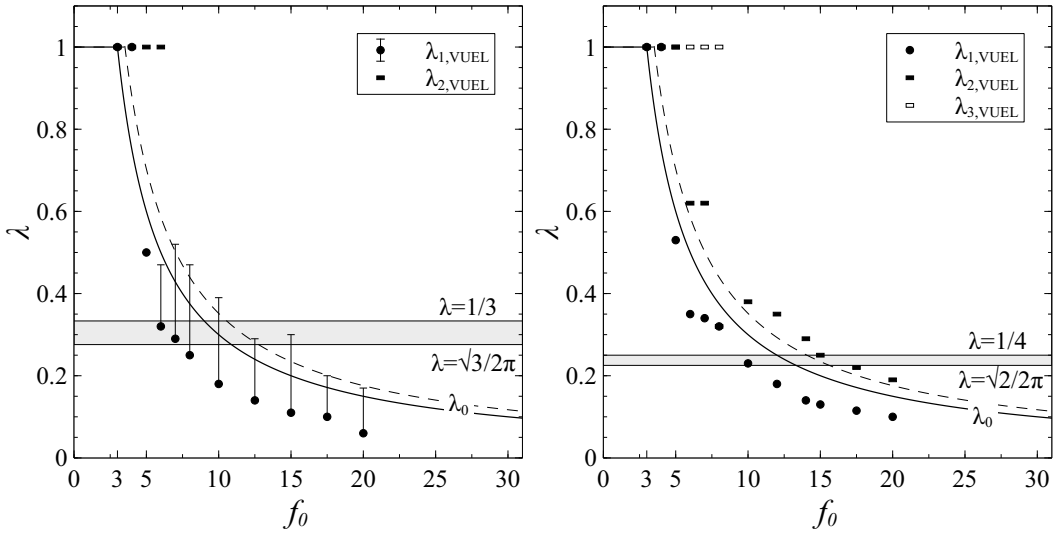

(a) $D/H = 20$

(b) $D/H = 32$

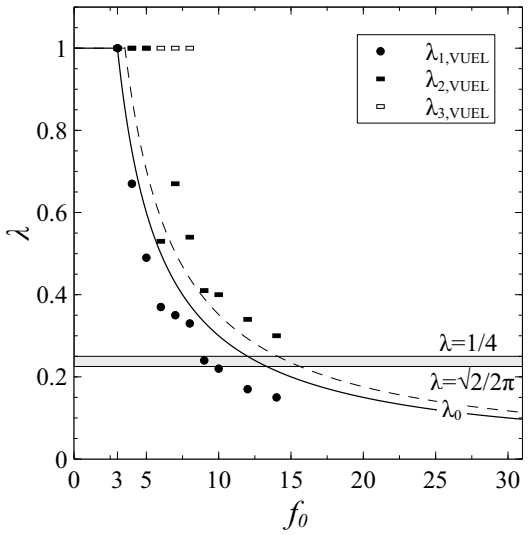

(c) $D/H = 40$

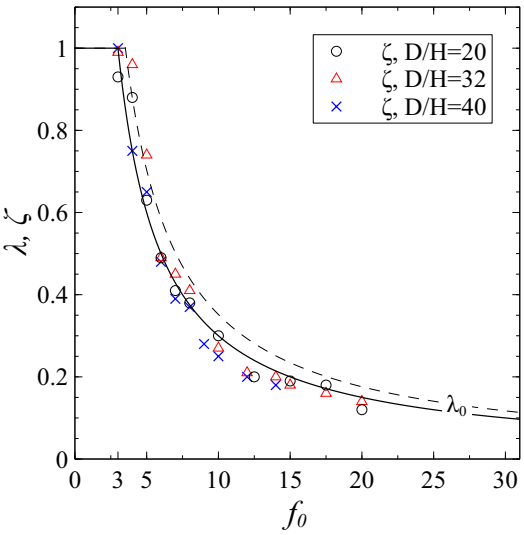

(d)

Figure 3.14: Numerical predictions of the hinge position λ_i and of the hazard zone ζ (d) from the first parametric study on pipe whips. $D/H = 20, 32, 40$, $f_0 \in [3, 30]$.

3.4.2 Effect of concentrated mass

The second parametric study investigates the change in the modes of deformation when the pipes of Table 3.3 are additionally loaded with a concentrated mass at the free end. The mass aims to simulate the weight of a flange or connector. The values of concentrated mass for the test cases #1m and #2m, reported in Table 3.4, are taken from [2]. The mass for test case #3m corresponds to that of a typical flange for high-pressure pipelines [81].

The numerical results of the second parametric study are reported in Figure 3.15. It is observed that the presence of the concentrated tip mass has the effect of extending the range of f_0 in which the cantilever deformation mode occurs. In particular, this was the mode of deformation observed for the test case #3m in the

Table 3.4: Values of pipe dimensions for the second parametric study on pipe whips, where each pipe has a concentrated mass m at its tip. All other parameters are unvaried from Table 3.3.

Test case	D/H	m (kg)	$\gamma = m/(\rho AL)$
#1m	20	1.8	0.2
#2m	32	1.4	0.2
#3m	40	1700	1.1

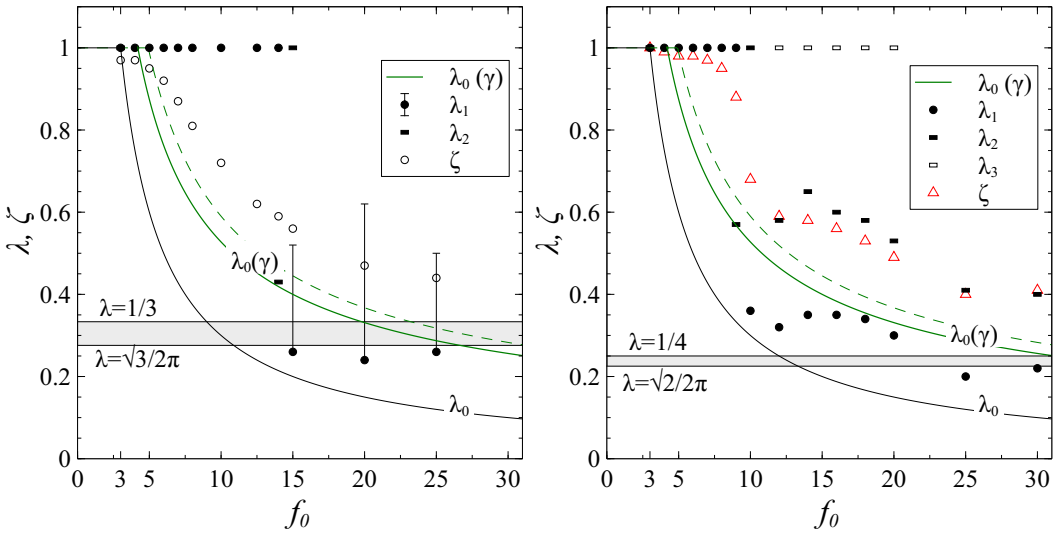

(a) $D/H = 20$ **(b)** $D/H = 32$

Figure 3.15: Numerical predictions of the hinge position λ_i and the hazard zone ζ from the first parametric study on thick (a) and thin (b) pipe whips.

whole range of f_0 considered. For this reason, the plot of the case #3m results is here omitted. In the test case #1m (Figure 3.15 (a)), a singular deformation mode takes place for $f_0 = 14$, in which the first plastic hinge forms at the fixed end ($\lambda = 1$), followed by the formation of a secondary hinge at $\lambda \approx 0.42$. At $f_0 = 15$, an abrupt transition between cantilever mode and self-intersecting mode with $\lambda_1 < \sqrt{(3)}/2\pi$ is observed, as predicted by equation (3.20).

Numerical predictions of ζ for the two cases are shown in Figure 3.15 (a) and (b) as white circles and triangles, respectively. The results are compared with those obtained with the RPP model using equations (3.13) and (3.17) reported in the figure with green lines. In both cases, the theoretical model provides a considerable underestimation of the plastic hinge position, compared to numerical observations. For this reason, the parametric study is repeated for different values of γ.

The plot points in Figure 3.16 indicate the hazard zone predicted for a pipe with $D/H = 32$ in the force range $f_0 \in [3,30]$, loaded with a variable concentrated mass at its free end. The value of γ is increased from 0.1 until the only deformation mode observed in the force range is the cantilever mode. The theoretical model of equation (3.13) is not capable of predicting accurately the hazard zone, therefore a parametric relation is employed to fit the numerical data when departure from cantilever mode occurs,

$$\zeta = \frac{3}{f_0 - a_1 \gamma^{a_2}} + b_1 \gamma^{b_2}. \tag{3.22}$$

The best-fit parameters found are $a_1 = 10.44, a_2 = 0.6968, b_1 = 1.057, b_2 = 0.8102$. The parametric model reduces to $\zeta = 3/f_0$ when $\gamma = 0$, which successfully predicts the hazard zone for both thick and thin pipes, as already demonstrated in Figure 3.14 (d).

3.4.3 Effect of pipe length

The third parametric study investigates the effect of pipe length on the deformation whilst keeping all the other parameters constant (load intensity, cross-sectional geometry). The study employs the cross-sectional dimensions reported in Table 3.3

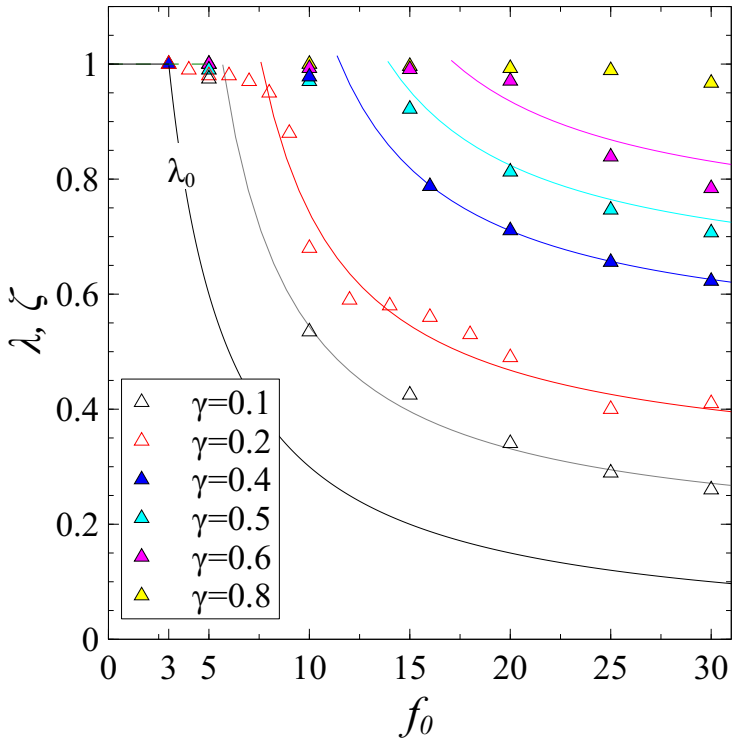

Figure 3.16: Numerical predictions of hazard zone ζ for thin pipe whips with $\gamma \in [0.1, 0.8]$. Solid lines represent the fitting curves using the parametric model of equation (3.22).

for the test case #3. Figure 3.17 shows that the predicted hazard zone, ζ, is in good agreement with the predictions of the RPP model.

This result is of particular relevance for the study of pipelines. Assuming that $\zeta = \lambda_0$, it follows from equation (3.4) that

$$\zeta = \frac{Z}{L} = \lambda_0 = \frac{3}{f_0}. \tag{3.23}$$

By substituting the definition of the dimensionless force $f_0 = F_0 L / M_P$ in the previous equation, one obtains an explicit expression for the vertical tip displacement Z

$$Z = \frac{3M_P}{F_0} = \frac{3M_P}{c_T P_0 A}, \tag{3.24}$$

where c_T is the thrust coefficient [2]. It can be noted that all the terms on the right-hand side of equation (3.24) depend solely on quantities related to the pipe's material, cross-sectional dimensions and internal pressure P_0, but are independent

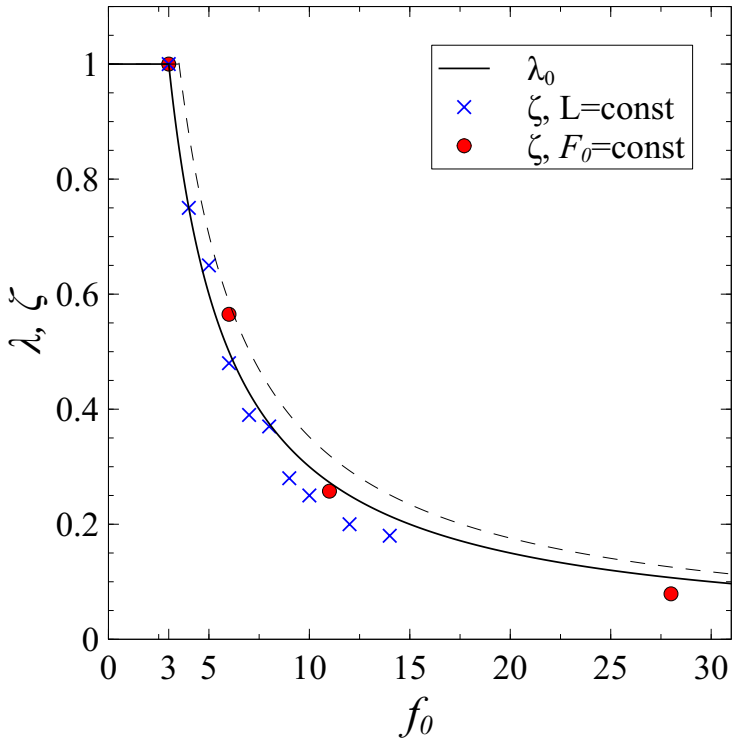

Figure 3.17: Numerical predictions for thin pipes of increasing length. The cross-sectional dimensions correspond to those of the test case #3 reported in Table 3.3.

of the pipe length L. Therefore, considering that P_0 is an input datum in a pipeline system, it can be deduced that the hazard zone of a pipeline is constant once the cross-sectional geometry is fixed.

3.4.4 Comparison with shell elements

To complete the analysis, the numerical results of the model of a thin pipe employing VUEL BM2D elements are compared with those obtained using an equivalent model in in Abaqus/explicit employing standard shell elements (type S4R). In order to discretise the geometry appropriately, 40 shell elements with aspect ratio 1 were used to partition the cross-sectional circumference and the pipe length. The final mesh is composed of 27360 shell elements.

Figure 3.18 (a) and (c) show that there is reasonably good agreement between the two models in terms of λ_i and ζ (the maximum relative difference for λ_1 was 6% measured at $f_0 = 15$ in Figure 3.18 (a), and for ζ was 35% at $f_0 = 10$ Figure 3.18 (d)), and the two models have similar deviations from the theoretical predictions.

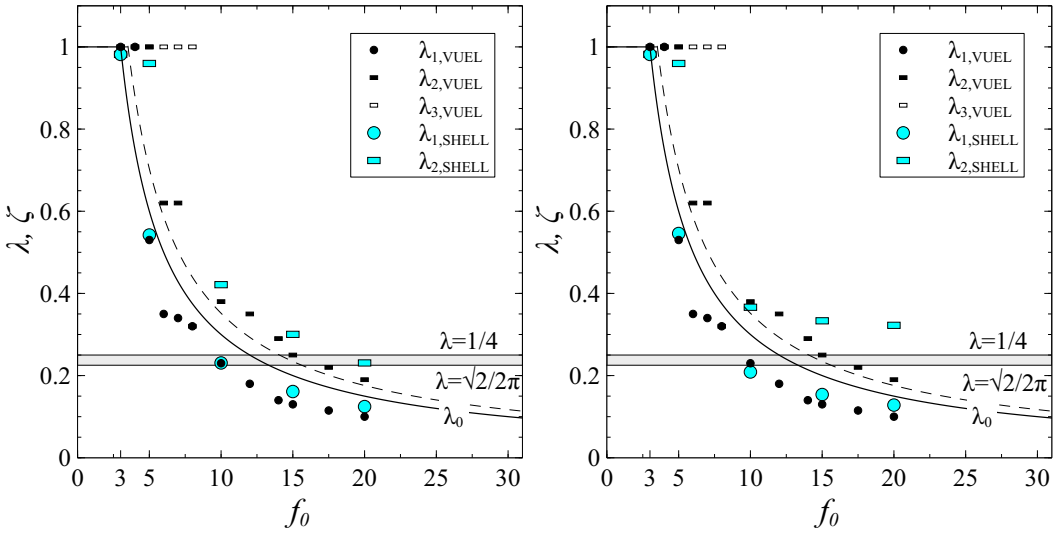

(a) strain-rate neglected

(b) strain-rate dependent

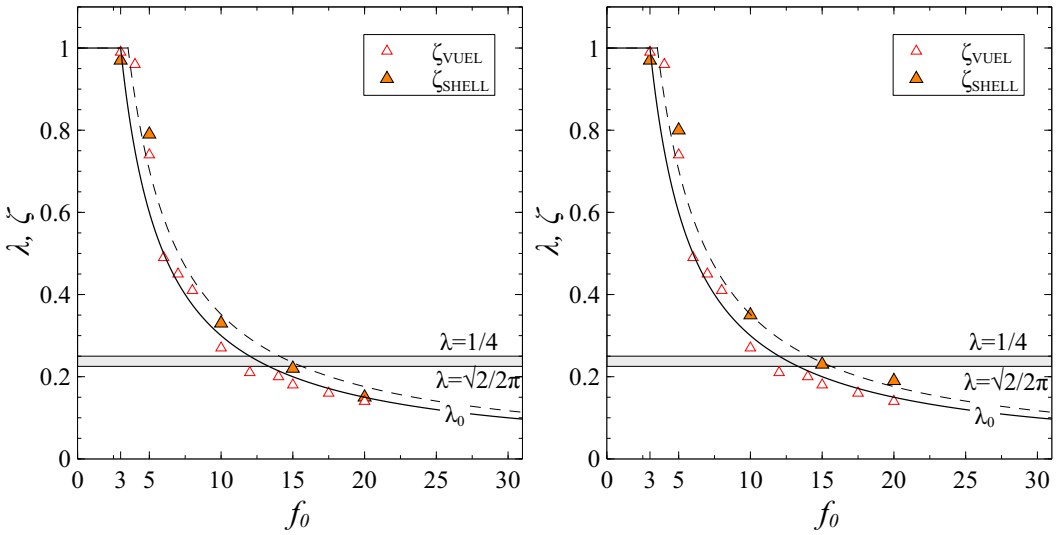

(c) strain-rate neglected

(d) strain-rate dependent

Figure 3.18: Comparison of numerical predictions of λ_i and ζ from pipe whips simulations using VUEL BM2D elements (labelled VUEL) and shell elements (labelled SHELL). The plots on the right-hand side show the numerical results for shell elements using a strain-rate dependent material model. $D/H = 32$, $f_0 \in [3, 30]$.

When comparing the results from the two models, one must take into account the limitations of the beam model, which is only able to capture the deformation of the longitudinal axis of the pipe, whilst the cross-sectional collapse is modelled through a constitutive relation. On the other hand, the usage of shell elements allows for a structural representation of the cross-section, which can directly influence the deformation profile.

The results from a third model employing shell elements and a strain-rate dependent material model are plotted in Figure 3.18 (b) and (d). There is in general negligible difference in results when strain-rate effects are considered, especially when comparing the hazard zone. The only substantial deviation was observed for λ_2 at $f_0 = 20$, where the high strain-rate causes an increase in the distance of the secondary plastic hinge from the free end.

3.4.5 Discussion

The theoretical RPP model predicts with satisfying accuracy the hazard zone of pipe whips in the absence of heavy flanges. It also offers a conservative prediction for the formation of plastic hinges, which is in turn useful for making kinetic energy calculations aimed at the correct design of pipe whip restraint devices.

The advantage of using the VUEL BM2D code was discussed in Section 3.2.3. Compared to traditional beam elements, the VUEL BM2D allows to successfully model the dynamic collapse mechanisms of pipes with a negligible increase of the computational cost. Therefore, the code is ideal for industrial applications thanks to its computational efficiency and ease of use, requiring only information of the cross-sectional dimensions to characterise the moment-curvature relationship.

In order to capture the dynamic collapse with similar accuracy in Abaqus/explicit, one would need to employ shell elements to discretise the whole pipe. Using the setup mentioned in Section 3.4.4, the completion time for two simulations with a timestep of 45ms and the same output frequency are: 31 s with VUEL BM2D elements, 45 min and 36 s with shell elements, or 4 min and 39 s with shell elements when 12 parallel units are used to speed-up the simulation. Therefore, a simulation employing VUEL BM2D elements is reportedly 88 times faster than an analogous

shell-elements simulation, and 9 times faster than the same simulation employing 12 parallel units.

3.5 Summary

The VUEL BM2D code developed in Chapter 2 was here used in FE simulations modelling the in-plane deformation of thick and thin pipe whips investigated experimentally by Reid et al. [2]. The code was then employed in parametric studies investigating the effect of the cross-sectional dimensions and loading conditions on the pipe deformation. Predictions of the hazard zone and the mechanism of collapse through the development of plastic hinges were compared against analytical predictions from a rigid-perfectly plastic beam model [8], and against numerical predictions from benchmark models in Abaqus using shell elements. It has been proven that simulations using the VUEL BM2D code are up to 88 times faster than the benchmark, whilst giving a reliable prediction of the deformation profile. The improved computational efficiency derives in the first place from the usage of one-dimensional beam elements, rather than two-dimensional shells, and in the second place from the adoption of the corotational formulation.

The parametric studies have led to the development of simple phenomenological equations useful in the design of piping systems. Equations (3.20) and (3.21) can be used to predict the initiation of self-intersecting collapse mechanisms in thick and thin pipe whips, respectively. Equation (3.22) predicts the extent of the hazard zone (in dimensionless form) for thin pipes bearing a heavy flange on the free end, and equation (3.24) allows to predict the pipe hazard zone with the knowledge of few system parameters, such as the fluid pressure, the cross-sectional dimensions and the strength of the pipe material.

Chapter 4

Simulation of out-of-plane pipe whips

4.1 Introduction

Similarly to the approach used in the 2D space, the objective of the corotational formulation in the 3D space is to introduce a local reference frame that follows the motion of each element, decomposing it into its rigid body and pure deformational parts. Within this framework, the deformational part is captured at the local frame, whereas the geometric non-linearity deriving from large rigid-body rotations is captured by the transformation tensors relating the local and global reference frames.

When the element type and the number of nodes are fixed, the transformation tensors depend only on geometrical relations, and do not depend on the formulation employed for the evaluation of local strains [22]. Assuming the change in deformation between subsequent increments is sufficiently small, linear theories can be used for the evaluation of strains in the local frame [27, 33].

The 3D corotational framework is presented visually in Figure 4.1. Let $\mathbf{e}_1$, $\mathbf{e}_2$, $\mathbf{e}_3$ be the unit vectors identifying the global Cartesian coordinate system,

$$\mathbf{e}_1 = \{1,0,0\}^{\mathrm{T}}, \quad \mathbf{e}_2 = \{0,1,0\}^{\mathrm{T}}, \quad \mathbf{e}_3 = \{0,0,1\}^{\mathrm{T}}, \tag{4.1}$$

and $\mathbf{e}_{0,1}$, $\mathbf{e}_{0,2}$, $\mathbf{e}_{0,3}$ the vectors identifying the initial configuration of a beam element in the 3D-space. It is possible to rotate between the two configurations using the rotation tensor $\mathbf{R}_0$:

$$\mathbf{e}_{0,i} = \mathbf{R}_0 \mathbf{e}_i\,, \quad i = 1,2,3\,. \tag{4.2}$$

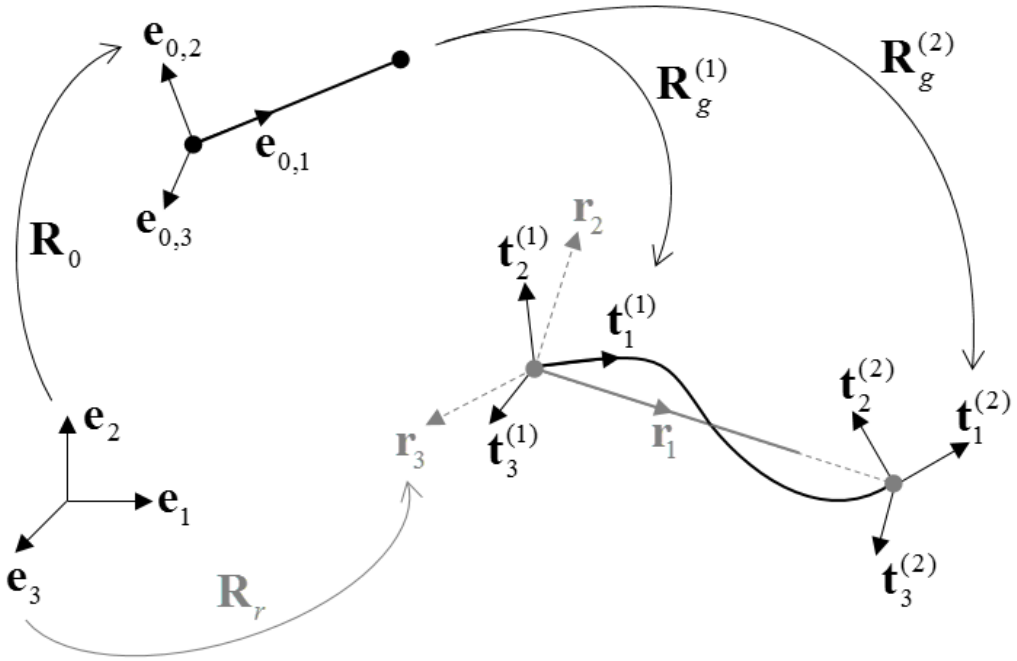

Figure 4.1: Coordinate systems for a beam element in space. The unit vectors $\mathbf{e}_i$ identify the global Cartesian coordinate system, and $\mathbf{e}_{0,i}$ the initial configuration of the beam element. At any time increment, $\mathbf{r}_i$ identify the current (corotated) configuration, and $\mathbf{t}_i^{(j)}$ the deformed configuration at the j-th node. The rotations $\mathbf{R}_0$, $\mathbf{R}_g^{(j)}$ and $\mathbf{R}_r$ are highlighted.

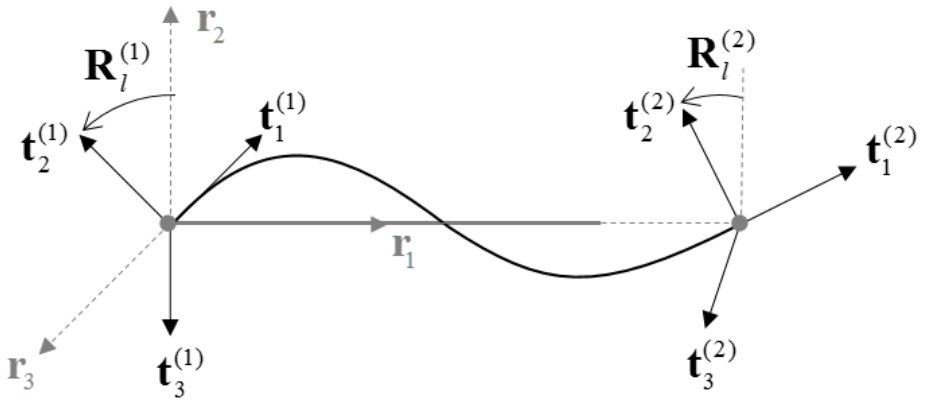

Figure 4.2: Corotational framework for a beam in space. At each node, the local configuration vectors $\mathbf{t}_i^{(j)}$ are obtained from the current configuration $\mathbf{r}_i$ through the rotations $\mathbf{R}_l^{(j)}$.

At any time increment a corotated frame is defined, indicated by the vectors $\mathbf{r}_1, \mathbf{r}_2, \mathbf{r}_3$, that moves rigidly with the element. With respect to the global coordinates it is obtained through the rotation $\mathbf{R}_r$:

$$\mathbf{r}_i = \mathbf{R}_r \mathbf{e}_i \,. \tag{4.3}$$

To separate the element motion between the rigid body and pure deformational parts, two local reference frames are introduced that follow the rotation of each node (j), indicated in Figure 4.1 as $\mathbf{t}_i^{(j)}$. The local frames are obtained from the initial configuration through the rotations $\mathbf{R}_g^{(j)}$:

$$\mathbf{t}_i^{(j)} = \mathbf{R}_g^{(j)} \mathbf{e}_{0,i} = \mathbf{R}_g^{(j)} \mathbf{R}_r \mathbf{e}_i \,, \quad j = 1,2 \,, \quad i = 1,2,3 \,. \tag{4.4}$$

In the previous expression, subscript $[\,]_g$ is used to indicate that the tensor is evaluated with respect to the global reference frame. It is also possible to obtain the local frames from the corotated configuration, as illustrated in Figure 4.2, with

$$\mathbf{t}_i^{(j)} = \mathbf{R}_l^{(j)} \mathbf{r}_i \,, \quad j = 1,2 \,, \quad i = 1,2,3 \,. \tag{4.5}$$

Here, subscript $[\,]_l$ indicates that the tensor is evaluated with respect to the local corotated frame. By equating the local and global expressions for $\mathbf{t}_i^{(j)}$, the local rotation matrices $\mathbf{R}_l^{(j)}$ are obtained [27, 33],

$$\mathbf{R}_l^{(j)} = \mathbf{R}_r^{\mathrm{T}} \mathbf{R}_g^{(j)} \mathbf{R}_0 \,, \quad j = 1,2 \,. \tag{4.6}$$

that determine the deformed configuration and are needed to compute the degrees of freedom and the local forces in the 3D corotational framework.

4.1.1 Parametrisation of finite rotations in 3D

There exist several notations to represent rotations in space, which can all be described in terms of three independent parameters. The simplest notation relies on

the definition of a rotation vector $\boldsymbol{\theta}$, expressed as

$$\boldsymbol{\theta} = \{\theta_1, \theta_2, \theta_3\}^{\mathrm{T}} = \theta \mathbf{n}. \tag{4.7}$$

According to equation (4.7), any finite rotation in space can be represented by a rotation of an angle $\theta = \sqrt{{\theta_1}^2 + {\theta_2}^2 + {\theta_3}^2}$ about an axis identified by the unit vector $\mathbf{n}$, as illustrated in Figure 4.3. In the previous section, finite rotations are expressed through the tensor $\mathbf{R}$, which is related to the rotation vector by Rodrigues's formula [25],

$$\mathbf{R} = \exp(\tilde{\boldsymbol{\Theta}}) = \mathbf{I} + \frac{\sin\theta}{\theta}\tilde{\boldsymbol{\Theta}} + \frac{1-\cos\theta}{\theta^2}\tilde{\boldsymbol{\Theta}}\tilde{\boldsymbol{\Theta}}, \tag{4.8}$$

where $\tilde{\boldsymbol{\Theta}}$ is a skew-symmetric matrix, defined as

$$\tilde{\boldsymbol{\Theta}} = \begin{bmatrix} 0 & -\theta_3 & \theta_2 \\ \theta_3 & 0 & -\theta_1 \\ -\theta_2 & \theta_1 & 0 \end{bmatrix}. \tag{4.9}$$

Using this notation, the rotation of a vector $\mathbf{x}_0$ is computed through the product

$$\mathbf{x} = \mathbf{R}\mathbf{x}_0 \tag{4.10}$$

and consecutive rotations are obtained through a sequence of matrix products. The relationship (4.8) employs a matrix exponential to obtain the rotation tensor $\mathbf{R}$ from

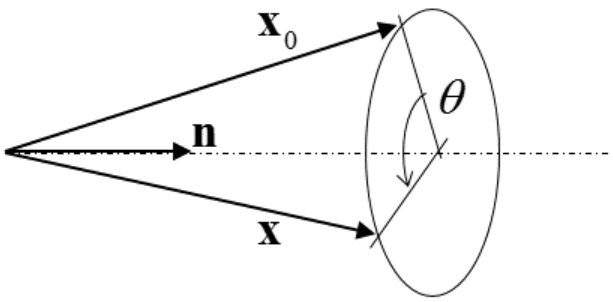

Figure 4.3: Finite rotation of a vector in space.

the matrix $\tilde{\mathbf{\Theta}}$. If the rotation angle is non-null, the inverse function is defined

$$\tilde{\mathbf{\Theta}} = \log(\mathbf{R}), \tag{4.11}$$

which allows to obtain the rotation angles θ_i from the tensor $\mathbf{R}$.

4.1.2 Variation of finite rotations

The evaluation of strains and local forces will require calculating the admissible variations of rotation tensors, $\delta\mathbf{R}$. Suppose at a certain increment the element is perturbed from the configuration $r_i = \mathbf{R}e_i$ to the new configuration $r_i'' = \mathbf{R}_\varepsilon e_i$. Applying the same approach of equation (4.4) for compound rotations and equation (4.8) gives

$$\mathbf{R}_\varepsilon = \exp\left(\varepsilon\delta\tilde{\mathbf{W}}\right)\mathbf{R} \tag{4.12}$$

where $\varepsilon\delta\tilde{\mathbf{W}}$ is the skew-symmetric matrix describing the infinitesimal rotation between r_i and r_i''. If $\mathbf{R}$ is fixed, the variation $\delta\mathbf{R}$ is then calculated as [33]

$$\delta\mathbf{R} = \left.\frac{\partial\mathbf{R}_\varepsilon}{\partial\varepsilon}\right|_{\varepsilon=0} = \delta\tilde{\mathbf{W}}\mathbf{R}. \tag{4.13}$$

From a physical point of view, equation (4.13) implies a change of variables from the infinitesimal rotation vector $\delta\boldsymbol{\theta}$ to the spin variables $\delta\tilde{\mathbf{W}}$ [27]. The change of variables is operated through the formulas

$$\delta\mathbf{W} = \mathbf{T}_S\delta\boldsymbol{\theta} \quad \text{or} \quad \delta\boldsymbol{\theta} = \mathbf{T}_S^{-1}\delta\mathbf{W} \tag{4.14}$$

with the transformation matrices

$$\mathbf{T}_S = \frac{\sin\theta}{\theta}\mathbf{I} + \left(1 - \frac{\sin\theta}{\theta}\right)\boldsymbol{\theta}\boldsymbol{\theta}^{\mathrm{T}} + \frac{1}{2}\left(\frac{\sin\theta/2}{\theta/2}\right)^2\tilde{\mathbf{\Theta}}, \tag{4.15}$$

$$\mathbf{T}_S^{-1} = \frac{\theta/2}{\tan\theta/2}\mathbf{I} + \left(1 - \frac{\theta/2}{\tan\theta/2}\right)\boldsymbol{\theta}\boldsymbol{\theta}^{\mathrm{T}} - \frac{1}{2}\tilde{\mathbf{\Theta}}. \tag{4.16}$$

The details pertaining to how to obtain the equations (4.14) to (4.16) are discussed in [27]. It must be noted that the relations above are not defined for angles $\theta = \pm n\pi$,

which limits the angular variation between consecutive increment and, as a consequence, the size of time increments.

4.2 Corotational kinematics in 3D space

The scope of this section is the derivation of the internal force vector and the mass matrix that define the kinematics of a two-node beam element using the corotational formulation.

The vector of degrees of freedom of a beam element in space, with respect to the global reference frame, $\mathbf{u}$, is characterised by 6 components for each node, 3 displacements and 3 rotations,

$$\mathbf{u} = \{u_1, u_2, u_3, \theta_1, \theta_2, \theta_3\}^{(j)^{\mathrm{T}}}, \quad j = 1,2, \tag{4.17}$$

to which corresponds a force vector, $\mathbf{f}$, of the same length,

$$\mathbf{f} = \{N_1, N_2, N_3, M_1, M_2, M_3\}^{(j)^{\mathrm{T}}}, \quad j = 1,2. \tag{4.18}$$

Using the corotational framework, the deformation vector expressed in the local reference frame, $\bar{\mathbf{u}}$, and the local force vector, $\bar{\mathbf{f}}$, have only 7 components, respectively

$$\bar{\mathbf{u}} = \left\{\bar{u}, \bar{\theta}_1^{(1)}, \bar{\theta}_2^{(1)}, \bar{\theta}_3^{(1)}, \bar{\theta}_1^{(2)}, \bar{\theta}_2^{(2)}, \bar{\theta}_3^{(2)}\right\}^{\mathrm{T}}, \tag{4.19}$$

$$\bar{\mathbf{f}} = \left\{\bar{N}, \bar{T}^{(1)}, \bar{M}_2^{(1)}, \bar{M}_3^{(1)}, \bar{T}^{(2)}, \bar{M}_2^{(2)}, \bar{M}_3^{(2)}\right\}^{\mathrm{T}}. \tag{4.20}$$

In the previous equations, the symbol [$\bar{}$] indicates quantities expressed in the local frame, $\bar{u} = L_n - L_0$ is the variation in element length and $\bar{N}$ the force acting along the longitudinal axis. For each node, the angles of twist $\bar{\theta}_1^{(j)}$ about the local axes $\mathbf{t}_1^{(j)}$ correspond to the twisting moments $\bar{T}^{(j)}$, and the rotation angles $\bar{\theta}_2^{(j)}$ and $\bar{\theta}_3^{(j)}$ correspond to the local bending moments $\bar{M}_2^{(j)}$ and $\bar{M}_3^{(j)}$.

As in the 2D case, the local and global deformation vectors are related through

the transformation matrix **B**

$$\delta\bar{\mathbf{u}} = \mathbf{B}\delta\mathbf{u}\,. \tag{4.21}$$

At any time increment, the components of the local force vector, i.e. the axial force, the twisting moment and the bending moments, are evaluated through appropriate constitutive relations that depend on the local deformation and strains

$$\bar{\mathbf{f}} = f\left(\delta\bar{\mathbf{u}}\right). \tag{4.22}$$

Then, the expression of the global force vector is obtained by equating the internal virtual work evaluated in the local system to that evaluated in the global system

$$U = \delta\bar{\mathbf{u}}^{\mathrm{T}}\bar{\mathbf{f}} = \delta\mathbf{u}^{\mathrm{T}}\mathbf{f}. \tag{4.23}$$

Substituting (4.21) into (4.23) gives

$$\mathbf{f} = \mathbf{B}^{\mathrm{T}}\bar{\mathbf{f}}. \tag{4.24}$$

4.2.1 Transformation matrix B

The approach proposed by Battini [27] to obtain an expression for **B** in the 3D space involves an intermediate change of variables from local to spin variables, $\delta\bar{\boldsymbol{\theta}} \rightarrow \delta\bar{\mathbf{w}}$, followed by a change from spin to global variables, $\delta\bar{\mathbf{w}} \rightarrow \delta\boldsymbol{\theta}$. With this approach, the transformation matrix is decomposed in two components, leading to:

$$\mathbf{B} = \mathbf{B}_a\mathbf{B}_g \tag{4.25}$$

and

$$\delta\bar{u} = \mathbf{B}_a\mathbf{B}_g\delta\mathbf{u}\,. \tag{4.26}$$

4.2.1.1 Change of variable $\mathbf{B}_a$: $\delta\bar{\boldsymbol{\theta}} \rightarrow \delta\bar{\mathbf{w}}$

Remembering the definition of the rotation vector $\boldsymbol{\theta}$, the variation of the degrees of freedom in local components may be written as

$$\delta\bar{\mathbf{u}} = \left\{\delta\bar{u}, \delta\bar{\boldsymbol{\theta}}^{(1)}, \delta\bar{\boldsymbol{\theta}}^{(2)}\right\}^{\mathrm{T}}, \tag{4.27}$$

whereas its equivalent in spin variables is

$$\delta\bar{\mathbf{u}}_a = \left\{\delta\bar{u}, \delta\bar{\mathbf{w}}^{(1)}, \delta\bar{\mathbf{w}}^{(2)}\right\}^{\mathrm{T}}. \tag{4.28}$$

Remembering the variational principle (4.14),

$$\delta\bar{\boldsymbol{\theta}}^{(j)} = \mathbf{T}_S^{-1(j)}\delta\bar{\mathbf{w}}^{(j)}. \tag{4.29}$$

The change of basis is then obtained with

$$\delta\bar{\mathbf{u}} = \mathbf{B}_a\delta\bar{\mathbf{u}}_a, \tag{4.30}$$

where

$$\mathbf{B}_a = \begin{bmatrix} 1 & \emptyset_{1\times3} & \emptyset_{1\times3} \\ \emptyset_{3\times1} & \mathbf{T}_S^{-1(1)} & \emptyset_{3\times3} \\ \emptyset_{3\times1} & \emptyset_{3\times3} & \mathbf{T}_S^{-1(2)} \end{bmatrix}. \tag{4.31}$$

Here, $\emptyset_{n\times m}$ represent zero matrices, whereas the matrices $\mathbf{T}_S^{-1(j)}$ were defined in equation (4.16).

4.2.1.2 Change of variable $\mathbf{B}_g$: $\delta\bar{\mathbf{w}} \rightarrow \delta\boldsymbol{\theta}$

The second change of variables requires finding the matrix $\mathbf{B}_g$ that transforms $\bar{\mathbf{u}}_a$ into the global deformation vector $\delta\mathbf{u}$,

$$\delta\mathbf{u} = \left\{\delta u_1^{(1)}, \delta u_2^{(1)}, \delta u_3^{(1)}, \delta\boldsymbol{\theta}^{(1)}, \delta u_1^{(2)}, \delta u_2^{(2)}, \delta u_3^{(2)}, \delta\boldsymbol{\theta}^{(2)}\right\}. \tag{4.32}$$

The first row of $\mathbf{B}_g$, relating the change in length of the element to the nodal displacements, is simply evaluated as

$$\mathbf{b}_g = \left\{-\mathbf{r}_1^{\mathrm{T}}, \mathbf{0}_{1\times 3}, \mathbf{r}_1^{\mathrm{T}}, \mathbf{0}_{1\times 3}\right\} \tag{4.33}$$

where $\mathbf{r}_1$ is the axial vector of Figure 4.1. The expression for the remaining rows of $\mathbf{B}_g$ is obtained in Battini [27] by differentiating $\delta\bar{\mathbf{w}}/\delta\bar{\boldsymbol{\theta}}$. The complete expression is

$$\mathbf{B}_g = \begin{bmatrix} \mathbf{b}_g \\ \mathbf{P}\mathbf{E}^{\mathrm{T}} \end{bmatrix}, \tag{4.34}$$

with

$$\mathbf{E} = \begin{bmatrix} \mathbf{R}_r & \mathbf{0}_{3\times 3} & \mathbf{0}_{3\times 3} & \mathbf{0}_{3\times 3} \\ \mathbf{0}_{3\times 3} & \mathbf{R}_r & \mathbf{0}_{3\times 3} & \mathbf{0}_{3\times 3} \\ \mathbf{0}_{3\times 3} & \mathbf{0}_{3\times 3} & \mathbf{R}_r & \mathbf{0}_{3\times 3} \\ \mathbf{0}_{3\times 3} & \mathbf{0}_{3\times 3} & \mathbf{0}_{3\times 3} & \mathbf{R}_r \end{bmatrix}, \tag{4.35}$$

where $\mathbf{R}_r$ is the rotation matrix of equation (4.3) and

$$\mathbf{P} = \begin{bmatrix} 0 & 0 & -\frac{\eta}{L} & 1-\frac{\eta_{12}}{L} & \frac{\eta_{11}}{2} & 0 & 0 & 0 & \frac{\eta}{L} & -\frac{\eta_{22}}{2} & \frac{\eta_{21}}{2} & 0 \\ 0 & \frac{1}{L} & -\frac{1}{L} & 0 & 1 & 0 & 0 & 0 & \frac{1}{L} & 0 & 0 & 0 \\ 0 & 0 & 0 & 0 & 0 & 1 & 0 & -\frac{1}{L} & 0 & 0 & 0 & 0 \\ 0 & 0 & -\frac{\eta}{L} & -\frac{\eta_{12}}{L} & \frac{\eta_{11}}{2} & 0 & 0 & \frac{\eta}{L} & 0 & 1-\frac{\eta_{22}}{2} & \frac{\eta_{21}}{2} & 0 \\ 0 & \frac{1}{L} & -\frac{1}{L} & 0 & 0 & 0 & 0 & 0 & \frac{1}{L} & 0 & 1 & 0 \\ 0 & 0 & 0 & 0 & 0 & 0 & 0 & 0 & -\frac{1}{L} & 0 & 0 & 1 \end{bmatrix}. \tag{4.36}$$

The terms η and η_{hk} in the equation above are coefficients that depend on the local vectors $\mathbf{r}_i$ [27], whose expressions will be explained in Section 4.4.

4.3 Local element formulation

The formulation for the local strains and forces of the corotational beam element in the 3D space follows largely that of the 2D beam element, with the addition of the twisting motion about the beam longitudinal axis and a second bending moment along the extra perpendicular axis. The new element, named VUEL BM3D, employs the Euler-Bernoulli formulation for evaluating the local strains, with the hermitian shape functions [33]:

$$N_1 = 1-\xi\,, \qquad N_2 = \xi\,, \tag{4.37}$$

$$N_3 = \xi L(1-\xi)^2\,, \quad N_4 = -\xi^2 L(1-\xi)\,, \tag{4.38}$$

where $\xi = x_1/L$ is the dimensionless coordinate along the $\mathbf{r}_1$ axis. The local strains are then evaluated as

$$\varepsilon_{\text{nom}} = \frac{\partial}{\partial\xi}\bar{u}\,, \tag{4.39}$$

$$k_1(\xi) = \frac{\partial^2}{\partial\xi^2}\left[N_1\bar{\theta}_1^{(1)} + N_2\bar{\theta}_1^{(2)}\right], \tag{4.40}$$

$$k_i(\xi) = \frac{\partial^2}{\partial\xi^2}\left[N_3\bar{\theta}_i^{(1)} + N_4\bar{\theta}_1^{(2)}\right], \quad i = 2,3 \tag{4.41}$$

which leads to

$$\varepsilon_{\text{nom}} = L_n/L - 1\,, \tag{4.42}$$

$$k_1 = \left(\bar{\theta}_1^{(2)} - \bar{\theta}_1^{(1)}\right)/L, \tag{4.43}$$

$$k_2(\xi) = \left[-2\left(\bar{\theta}_2^{(2)} + 2\bar{\theta}_2^{(1)}\right) + 6\xi\left(\bar{\theta}_2^{(2)} + \bar{\theta}_2^{(1)}\right)\right]/L, \tag{4.44}$$

$$k_3(\xi) = \left[-2\left(\bar{\theta}_3^{(2)} + 2\bar{\theta}_3^{(1)}\right) + 6\xi\left(\bar{\theta}_3^{(2)} + \bar{\theta}_3^{(1)}\right)\right]/L. \tag{4.45}$$

Substituting $\xi = 0$ and $\xi = 1$ in the equations above allows to evaluate the strain at the first and second node of the element, respectively.

4.3.1 Constitutive assumptions and internal force vector

The corotational beam element developed by Battini [27] for static analyses employed a bi-linear elastoplastic law, whereas the element developed by Le [33] for dynamic analyses employed a linear-elastic constitutive law.

The VUEL BM3D element here developed presents an improvement on the formulations of [27] and [33], by employing the same constitutive assumptions of The VUEL BM2D element for evaluating the internal forces, with the addition of a constitutive model for torsion. The relationship between axial strains and axial forces is modelled through a piece-wise linear elasto-plastic model with strain hardening and softening, as described in Section 2.3. The relationship between the curvature along the axes 2,3 and the corresponding bending moment follows the model presented in Section 2.5, employing the M–k master curves obtained through numerical testing for thick and thin pipes.

Lastly, the VUEL BM3D element adopts a bi-linear approach to model the behaviour of the pipe in torsion, in which the initially linear stage is followed by a strain-hardening stage, as follows

$$T(k_1) = \begin{cases} T^*(k_1) = GI_p k_1 \,, & |k_1| < k_p \\ \\ T^H(k_1) = \text{sign}(k_1)\left(T_p + G_U I_p |k_1|\right) \,, & |k_1| \geq k_p \end{cases} \tag{4.46}$$

where G is the shear modulus, T_p the plastic twisting moment and I_p the second polar moment of area so that, for a pipe of circular cross-section,

$$T_p = \frac{2\pi\sigma_Y}{3\sqrt{3}}\left(R_{\text{ext}}^3 - R_{\text{int}}^3\right) \,, \tag{4.47}$$

$$k_p = \frac{T_p}{GI_p} \,, \tag{4.48}$$

$$G_U = \frac{1}{\sqrt{3}}\frac{\sigma_U - \sigma_Y}{\varepsilon_U - \varepsilon_Y} \,. \tag{4.49}$$

This approach is relatively simpler than that employed for the bending moment, and

future studies are required to obtain a more comprehensive characterisation of the torsional behaviour. The final torsional model, obtained combining the constitutive relation (4.46) with a kinematic hardening law, is reported in Appendix C and schematised in Figure 4.4.

The inclusion of a more realistic constitutive model for torsion, which will require the execution of experimental and numerical tests for pipes in torsion, will be the object of future studies.

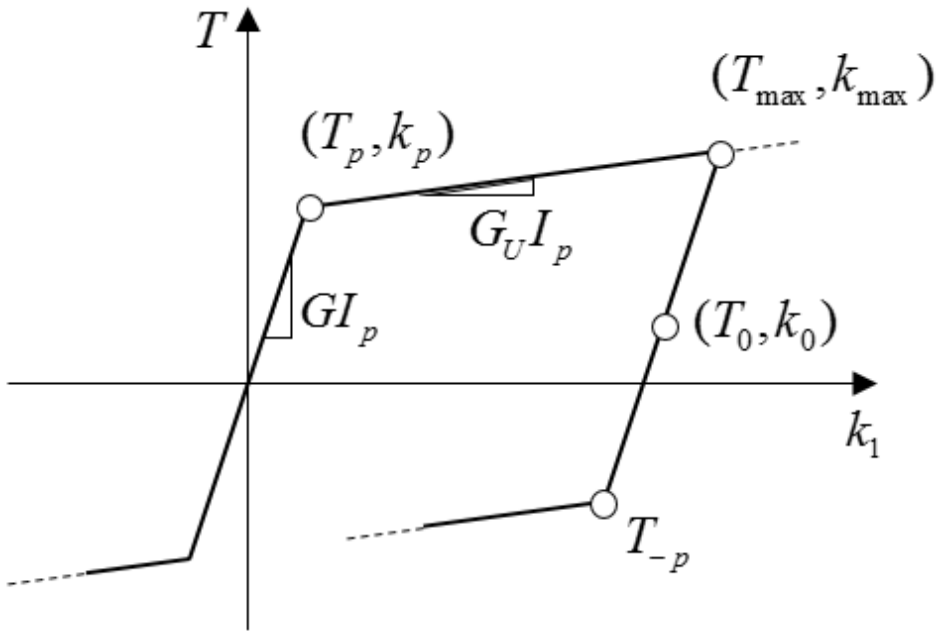

Figure 4.4: Schematics of the torsional constitutive model for the VUEL BM3D element code, as described in Listing C.

4.3.2 Element mass matrix and stable time increment

The final step in the construction of the corotational kinematics is the definition of the mass matrix. The solution algorithm employed in the present work requires the use of a lumped mass matrix, **M**, to reduce the computational cost. Taking into account the order of the degrees of freedom in the global frame, the matrix is

defined as

$$\mathbf{M} = \begin{bmatrix} m_0 & & & & & & & & & & & \\ & m_0 & & & & & & & & & & \\ & & m_0 & & & & & & & & & \\ & & & \mathbf{M}_r & & & & & & & & \\ & & & & m_0 & & & & & & & \\ & & & & & m_0 & & & & & & \\ & & & & & & m_0 & & & & & \\ & & & & & & & \mathbf{M}_r & & & & \end{bmatrix} \tag{4.50}$$

where $m_0 = \rho AL/2$ is the translational inertia term — it corresponds to half of the element mass for a beam element with two nodes — and $\mathbf{M}_r$ is the matrix given by

$$\mathbf{M}_r = \mathbf{R}_r \begin{bmatrix} m_2 & & \\ & m_1 & \\ & & m_1 \end{bmatrix} \mathbf{R}_r{}^{\mathrm{T}} \tag{4.51}$$

where $m_1 = m_0 L^2/12$ is the flexural inertia term and $m_2 = \rho L I_p/6$ is the torsional inertia.

The dynamic solution algorithm requires the specification of a stable time increment. The same formulation of the VUEL BM2D code is here used, given by

$$\Delta t = f\sqrt{\frac{\rho L L_n}{E}}. \tag{4.52}$$

with $f = 0.2$–0.01.

4.4 VUEL BM3D architecture

The sequence of operations that compose the coding of the VUEL BM3D element is here presented. At any increment, for each finite element, the explicit solution algorithm provides the current coordinates of the j-th node, $\mathbf{x}^{(j)}$, and the translational and rotational degrees of freedom associated with it, $\mathbf{u}^j$ and $\boldsymbol{\theta}^{(j)}$. The scope of the code is then to evaluate the internal force vector $\mathbf{f}$ and the mass matrix $\mathbf{M}$ necessary to solve Newton's equation and evaluate the state of the element at the end of the

increment. The list of operations to be executed is summarised as follows:

1. Evaluate the initial and current element length, L, L_n

$$\mathbf{L} = \mathbf{x}^{(2)} - \mathbf{x}^{(1)}, \qquad L = ||\mathbf{L}|| \tag{4.53}$$

$$\mathbf{L}_n = \mathbf{x}^{(2)} + \mathbf{u}^{(2)} - \mathbf{x}^{(1)} - \mathbf{u}^{(1)}, \qquad L_n = ||\mathbf{L}_n||. \tag{4.54}$$

2. Identify the initial reference frame $\mathbf{R}_0$, equation (4.2)

$$\mathbf{R}_0 = \begin{bmatrix} \mathbf{e}_{0,1} & \mathbf{e}_{0,2} & \mathbf{e}_{0,3} \end{bmatrix} \tag{4.55}$$

$$\mathbf{e}_{0,1} = \frac{\mathbf{L}}{L}, \quad \mathbf{e}_{0,3} = \frac{\mathbf{e}_1 \times \mathbf{e}_{0,1}}{||\mathbf{e}_1 \times \mathbf{e}_{0,1}||}, \quad \mathbf{e}_{0,2} = \frac{\mathbf{e}_{0,3} \times \mathbf{e}_{0,1}}{||\mathbf{e}_{0,3} \times \mathbf{e}_{0,1}||}. \tag{4.56}$$

3. Build the skew-symmetric global rotation matrices $\tilde{\mathbf{\Theta}}^{(j)}$, equation (4.9)

4. Obtain the global rotation matrices $\mathbf{R}_g^{(j)}$, equation (4.8)

$$\mathbf{R}_g^{(j)} = \exp\left(\tilde{\mathbf{\Theta}}^{(j)}\right), \quad j = 1,2. \tag{4.57}$$

5. Identify the current orientation $\mathbf{R}_r$, equation (4.3)

$$\mathbf{R}_r = \begin{bmatrix} \mathbf{r}_1 & \mathbf{r}_2 & \mathbf{r}_3 \end{bmatrix} \tag{4.58}$$

$$\mathbf{r}_1 = \frac{\mathbf{L}_n}{L_n}, \quad \mathbf{r}_3 = \frac{\mathbf{r}_1 \times \mathbf{p}}{||\mathbf{r}_1 \times \mathbf{p}||}, \quad \mathbf{r}_2 = \frac{\mathbf{r}_3 \times \mathbf{r}_1}{||\mathbf{r}_3 \times \mathbf{r}_1||} \tag{4.59}$$

where $\mathbf{p}$ is an auxiliary vector defined as

$$\mathbf{p} = \frac{1}{2}(\mathbf{p}_1 + \mathbf{p}_2) \tag{4.60}$$

$$\mathbf{p}_i = \mathbf{R}_g^{(j)} \mathbf{e}_{0,2}, \quad j = 1,2. \tag{4.61}$$

6. Evaluate the local rotation matrices $\mathbf{R}_l^{(j)}$, equation (4.6).

7. Use equation (4.11) to obtain the skew-symmetric local rotation matrices $\tilde{\mathbf{\Theta}}_l^{(j)}$

and the local rotation vectors $\bar{\boldsymbol{\theta}}^{(j)}$

$$\tilde{\boldsymbol{\Theta}}_l^{(j)} = \log\left(\mathbf{R}_l^{(j)}\right). \tag{4.62}$$

8. Compute the transformation matrix $\mathbf{B}$, equation (4.25). This step requires the definition of the coefficients encountered in equation (4.36). Based on the auxiliary vectors, they are defined as [33]

$$\eta = \frac{p_1}{p_2}, \quad \eta_{11} = \frac{p_{11}}{p_2}, \quad \eta_{12} = \frac{p_{12}}{p_2}, \quad \eta_{21} = \frac{p_{21}}{p_2}, \quad \eta_{21} = \frac{p_{22}}{p_2} \tag{4.63}$$

where the terms p_1, p_2, p_{11}, p_{12}, p_{21}, p_{22}, are derived from the relations

$$\begin{Bmatrix} p_1 \\ p_2 \\ 0 \end{Bmatrix} = \mathbf{R}_r^T \mathbf{p}\,, \quad \begin{Bmatrix} p_{11} \\ p_{12} \\ p_{13} \end{Bmatrix} = \mathbf{R}_r^T \mathbf{p}_1\,, \quad \begin{Bmatrix} p_{21} \\ p_{22} \\ p_{23} \end{Bmatrix} = \mathbf{R}_r^T \mathbf{p}_2\,. \tag{4.64}$$

9. Compute the local strains, equations (4.42)–(4.45).

10. Apply the constitutive models, Section 4.3.1.

11. Compute the local force vector $\bar{\mathbf{f}}$, equation (4.20).

12. Obtain the global force vector $\mathbf{f} = \mathbf{B}^{\mathrm{T}}\bar{\mathbf{f}}$, equation (4.24).

13. Build the mass matrix $\mathbf{M}$, equation (4.50)

14. Estimate the stable time increment Δt, equation (4.52).

4.4.1 Matrix exponential and logarithm

The steps 4 and 7 in the element coding requires the computation of matrix exponentials and logarithms. Battini [27] and Le [33] evaluate the exponential using a Taylor series expansion:

$$\mathbf{R} = \exp(\tilde{\boldsymbol{\Theta}}) \approx \mathbf{I} + \tilde{\boldsymbol{\Theta}} + \frac{1}{2}\tilde{\boldsymbol{\Theta}}^2\,. \tag{4.65}$$

The approximation has a truncation error of magnitude $o(\theta^2)$ that is negligible at any increment. However, the solution algorithms employed in dynamic analyses generally require 10^4–10^6 increments in a simulation, resulting in a non-negligible accumulated error. For that reason, the current work employs Rodrigues's formula to compute the exact matrix exponential. Similarly, it is possible to calculate the exact matrix logarithm. Rodrigues's formula (4.8) can be rewritten as

$$\mathbf{R} = \cos\theta\mathbf{I} + \frac{\sin\theta}{\theta}\tilde{\boldsymbol{\Theta}} + \frac{1-\cos\theta}{\theta^2}\boldsymbol{\theta}\boldsymbol{\theta}^{\mathrm{T}}. \tag{4.66}$$

Therefore, for any orthogonal matrix it is possible to directly derive the corresponding rotation vector and skew-symmetric matrix

$$\theta = \arccos\left(\frac{\mathrm{tr}\mathbf{R}-1}{2}\right), \tag{4.67}$$

$$\tilde{\boldsymbol{\Theta}} = \frac{\theta}{2\sin\theta}\left(\mathbf{R}-\mathbf{R}^{\mathrm{T}}\right). \tag{4.68}$$

The above equation requires that $\theta \neq 0$, in which case the result of the matrix logarithm is simply a zero matrix, and that $\theta \neq \pm n\pi$, in which case equation (4.66) gives

$$\theta_1 = \sqrt{\frac{\mathbf{R}(1,1)+1}{2}}\frac{\theta}{n}, \quad \theta_2 = \sqrt{\frac{\mathbf{R}(2,2)+1}{2}}\frac{\theta}{n}, \quad \theta_3 = \sqrt{\frac{\mathbf{R}(3,3)+1}{2}}\frac{\theta}{n}. \tag{4.69}$$

4.5 Model validation and implementation

This section deals with the results of numerical simulations carried out to validate the VUEL BM3D code. Despite the importance for many industries of accurately predicting the deformation mechanisms of out-of-plane pipe whips [1], and the numerical studies on the subject [11, 13], there is a lack in the literature of experimental data detailing the extent of the hazard zone and the formation of collapse mechanisms for this particular problem.

To compensate for the lack of experimental data required for the proper validation of the element code, we adopted the following approach: in the first step, a

numerical model for in-plane pipe whips is built using the VUEL BM3D code. The results were compared with those obtained with the VUEL BM2D code to ensure the correctness of the element coding in the case of pure bending. In the second step, the simulation of an out-of-plane pipe whip using VUEL BM3D is benchmarked against a model built in Abaqus using shell and beam elements, comparing its capability to model the effect of torsion on the pipe deformation.

4.5.1 Simulation of in-plane pipe whips with VUEL BM3D

The simulation setup previously described as test case #2 in Table 3.3 (Section 3.4.1) is here reproposed using the VUEL BM3D code. The pipe has dimensions $D = 50.8$ mm, $H = 1.58$ mm (D/H=32), $L = 2.73$ m and is loaded with a linearly decaying force of initial intensity $f_0 = 10$ and pulse duration $t_D = 68$ s. The simulation results are presented in Figure 4.5 (a, b) and benchmarked against an homologous simulation using the VUEL BM2D.

It can be seen from the Figures 4.5 (a) and (c) that the two simulations present the same results, in terms of deformed shape and hazard zone, in the time frame of interest. The results only start differing at 30 ms, after self impact has occurred. Our models do not consider the effect of self-contact. For this reason, the results from this point onward are not analysed. Figures 4.5 (b) and (d) show the distribution of curvature along the beam with the two models. The plot show analogous evolution for the distribution in the two cases. Plastic hinges form in the same position at the same time, and the difference between the two distributions becomes noticeable only at the root of the pipe, following the point of self-intersection. It must be noted that the measurement of the curvature is much more time-sensitive than that of the deformation profile. The software is only capable to provide the results at approximate times, and the temporal resolution is influenced by the time-stepping procedure employed by Abaqus. When an element enters into the plastic stage ($k > k_y$), evolves very rapidly, thus justifying the small discrepancies in curvature between the two models.

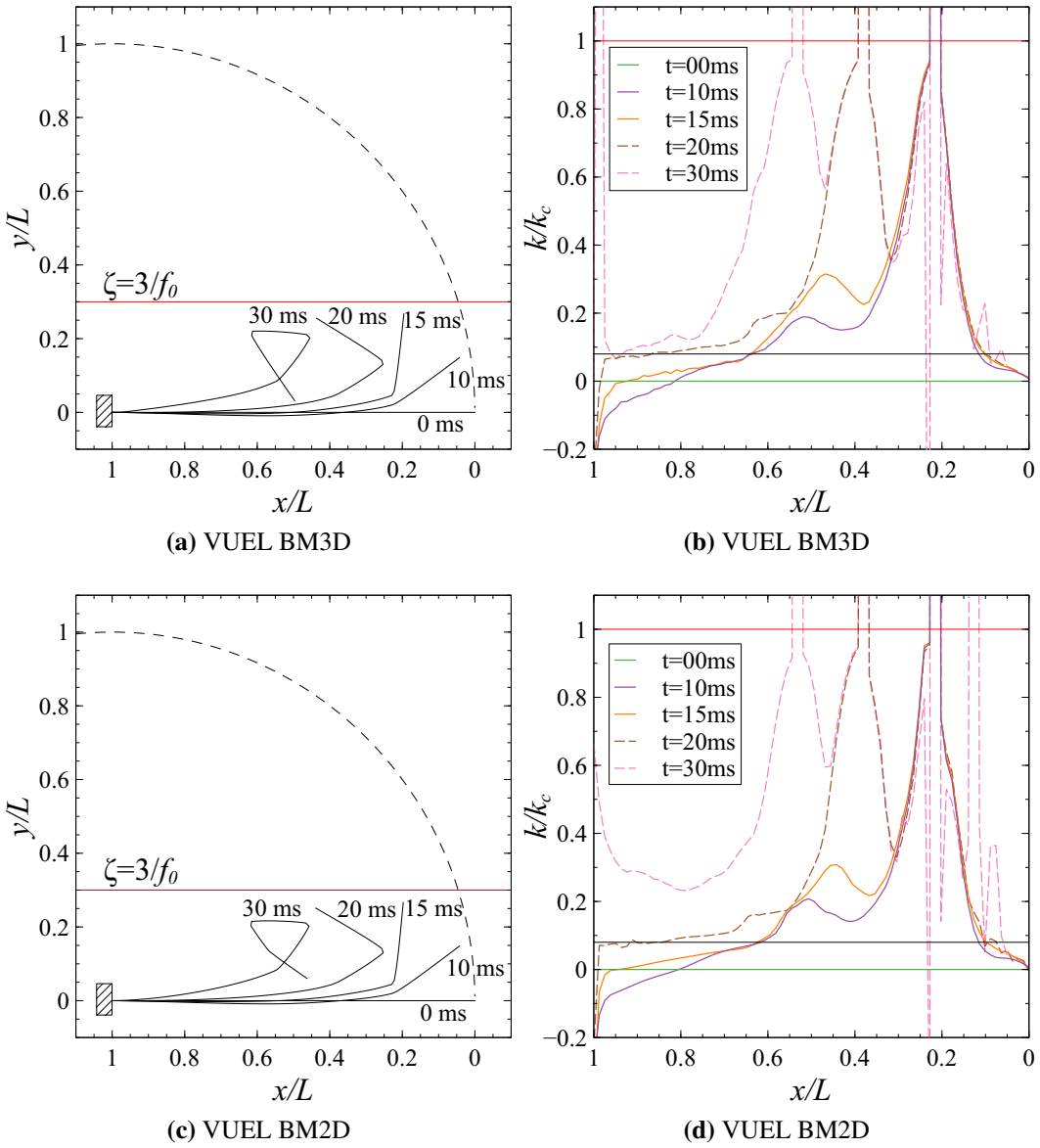

(a) VUEL BM3D **(b)** VUEL BM3D

(c) VUEL BM2D **(d)** VUEL BM2D

Figure 4.5: Simulation of an in-plane pipe whip with $D/H = 32$, $f_0 = 10$, using the pipe elements VUEL BM3D (top) and VUEL BM2D (bottom). Comparison of the deformation profile (plots a, c) and of the curvature distribution (plots b, d). Black lines (—) indicate the yield point ($k = k_y$) and red lines (—) indicate the critical point ($k = k_c$).

4.5.2 Simulation of out-of-plane pipe whips

Figure 4.6 illustrates the geometry of an initially bent cantilever pipe used for the simulation of out-of-plane pipe whips, taken from Reid et al. [13]. The segment AB, connecting the free end (A) to the elbow (B) has length $L_1 = 1.26$ m and the segment BC, connecting the elbow (B) to the root (C) has length $L_2 = 2.4$ m. The two segments are connected through a 90° elbow of radius $r = 0.1$ m. The circular thin-walled pipe has cross-sectional dimensions $D = 50.8$ mm, $H = 1.58$ mm (D/H=32). The system is subjected to a concentrated follower force of constant intensity $F_0 = 8$ kN, applied at A and originally acting in the z-direction. The weight of a flange at the free end is modelled with a concentrated mass $m = 1$ kg. The system is constrained in C with an encastre, modelled with fully-constrained boundary conditions.

The geometry was discretised in Abaqus/explicit using 96 beam elements of length $L = 0.039$ m. The results obtained with the model using VUEL BM3D element were benchmarked against those obtained in Abaqus using 96 Timoshenko B31 elements, and also against the results of an additional model using shell S4R element. In the latter, the shell elements had in-plane dimensions of 0.004 m×0.004 m, using 40 elements along the external cross-sectional circumference, for a total of 38552 elements. In the all the models, convergence was checked by measuring the free-end displacements and the position of the first plastic hinge.

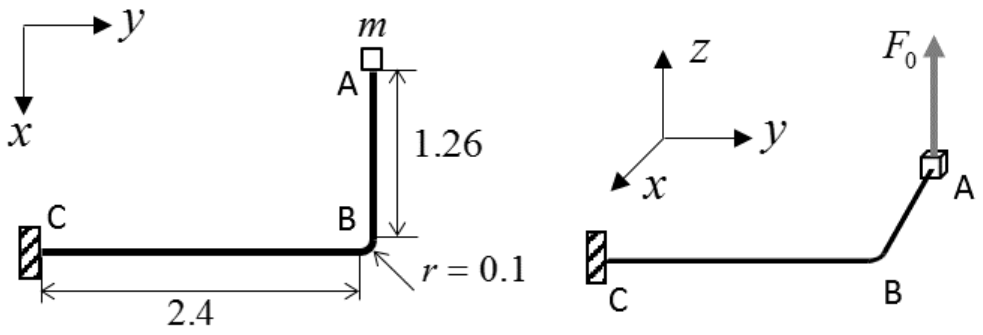

Figure 4.6: Geometry of the bent cantilever pipe with a 90° elbow used for the study of out-of-plane pipe whips. F_0 is a follower force, and m represent the pass of the tip flange. All dimensions are in m.

In each case, the element size satisfies the criterion of a relative error on the two quantities smaller than 3%.

4.5.3 Results and discussion

Figure 4.7 illustrates the modes of deformation of the pipe, as obtained from the benchmark simulation using shell elements. In the first 20 ms, Figure 4.7 (a), the loading causes the pipe to twist about the segment BC, which results in the rotation of segment AB in the xz-plane about the point B. At 30 ms, the pipe motion shows the initiation of a collapse mechanism (point D in the figure), evidenced by the deformation of the cross-section, that results from a combination of torsion and bending. The contour plot of the rotation magnitude, UR, shows that a second collapse mechanism has occurred at the elbow (point B), highlighted by the discontinuity of UR in that point. At 40 ms, the deformation of the cross-section shows that the first collapse mechanism has progressed from D towards the fixed end (point C), whereas the second collapse mechanism has localised at point B, leading to the complete occlusion of the cross-section.

The following time increments up to 80 ms, Figure 4.7 (c-f), show that point D has reached the fixed end, where it eventually causes complete cross-sectional collapse, while an additional collapse point arises at about 60 ms along the segment BC, as evidenced by the deformation of the member. The simulation was stopped at 100 ms due to the pipe undergoing a 360° rotation about the fixed end.

Figure 4.8 shows the deformation of the same pipe when modelled with VUEL BM3D elements. In the plot, the cartesian coordinates are divided by the total length L of the pipe. At each time frame, arrows point at the position of the elbow B. The deformation mechanism duplicates that observed with shell elements: the twisting and collapse about the elbow, a distributed collapse that starts along BC and progresses towards the root C, and a localised collapse in a point along BC starting from 60 ms. Visually similar results were obtained in the simulation using beam B31 elements, and are not reported here for brevity.

A thick dotted line illustrates the path of the free end of the pipe, where the loading is applied. At the beginning of the simulation, this path follows closely a

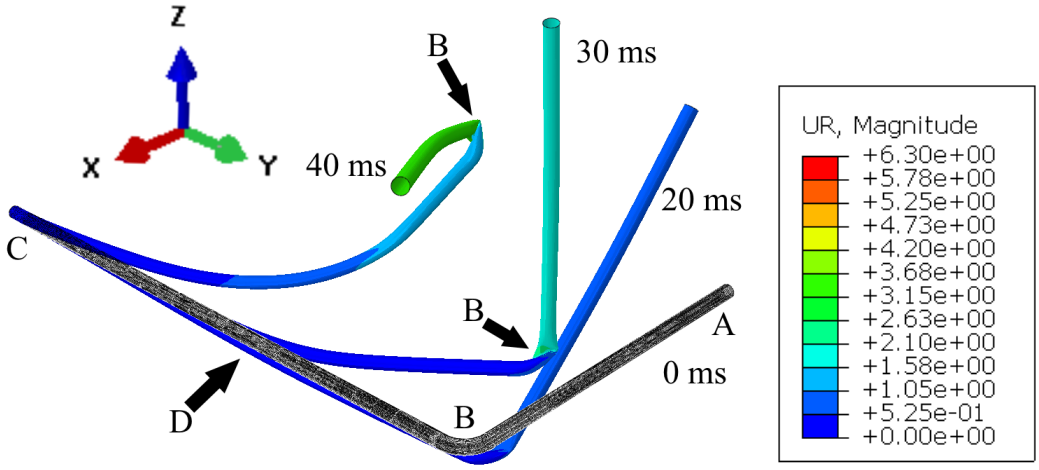

(a) $t = 0$–40 ms

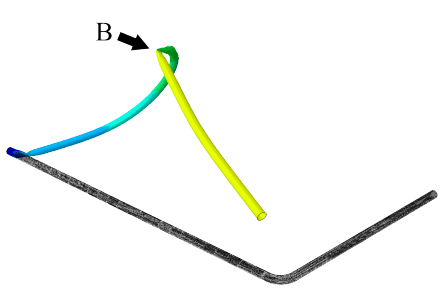

(c) $t = 50$ ms

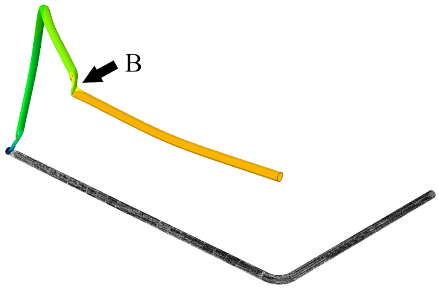

(d) $t = 60$ ms

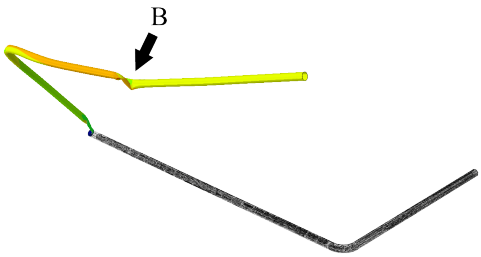

(e) $t = 70$ ms

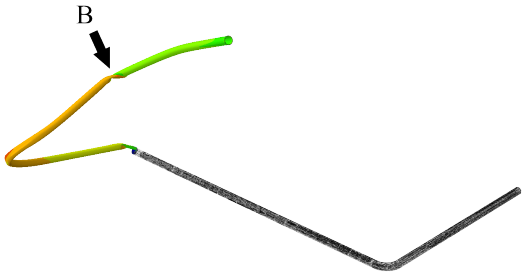

(f) $t = 80$ ms

Figure 4.7: Deformation of a out-of-plane pipe whip with $D/H = 32$, $F_0 = 8$kN, concentrated tip mass $m = 1$ kg modelled in Abaqus/explicit using shell S4R elements. Colours are used to indicate the rotation magnitude UR.

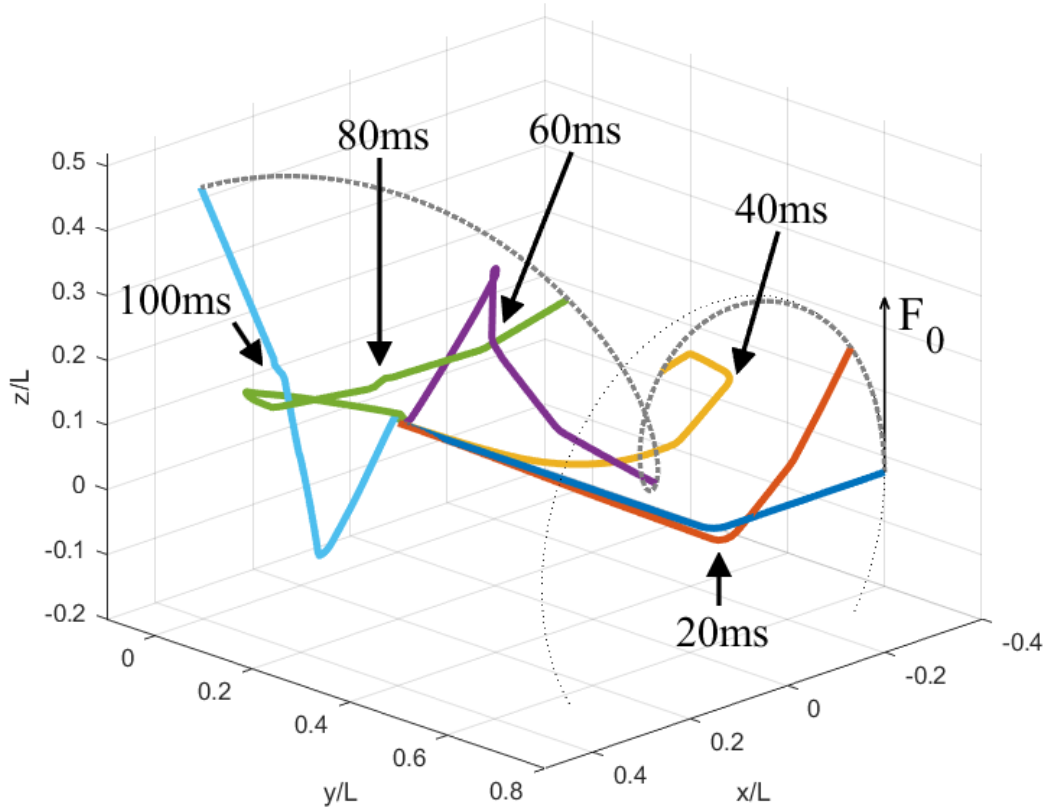

Figure 4.8: Deformation a of out-of-plane pipe whip with $D/H = 32$, $F_0 = 8$ kN, concentrated tip mass $m = 1$ kg modelled in Abaqus/explicit using VUEL BM3D elements. Arrows point at the position of the elbow at each time frame. A thick dotted line shows the path of the pipe tip, which is compared against a circular motion about the elbow, shown with a thin dotted line.

circular arch in the xz-plane of radius L_1, depicted with a thin dotted line in the figure, centred in the elbow. As the deformation progresses and the pipe collapses in several points, the tip motion deviates from the circular path and approaches the root. It is of interest noting that, despite the elbow being straightened at approximately 80 ms (as observed also for the shell elements simulation), the hazard zone of the pipe remains contained in a region of dimensions that are smaller than the total length of the pipe.

The tip displacement predicted with VUEL BM3D is compared in Figure 4.9 against that predicted with beam and shell elements. Although all the elements display similar evolutions of the displacements up to 40 ms, the beam element model shows an evident phase delay ($\Delta t \approx 5$ ms) and a slightly amplified magni-

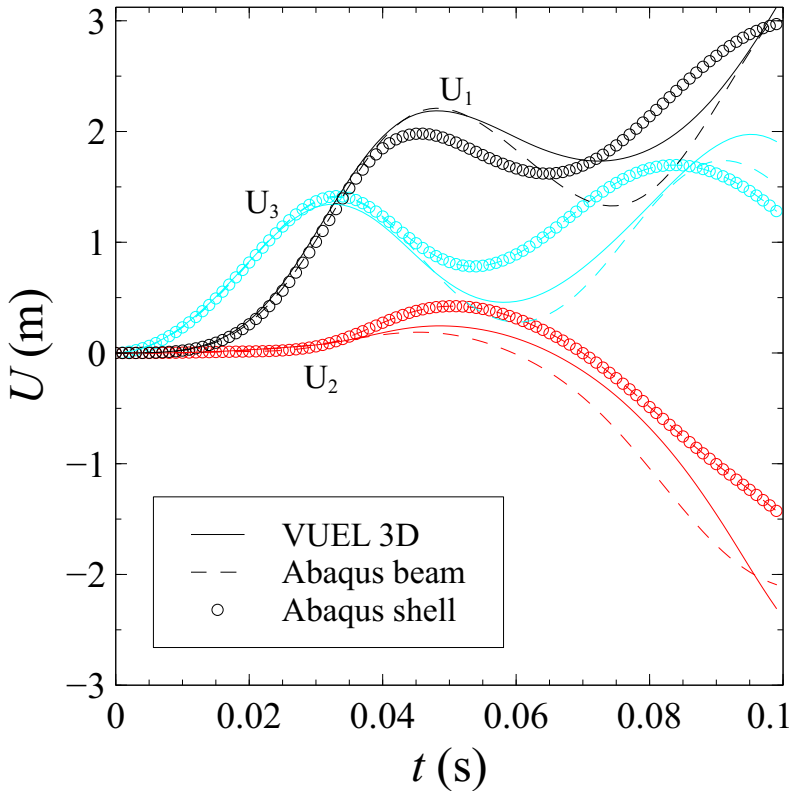

Figure 4.9: Comparison of the tip displacement in the simulation of the out-of-plane pipe whip modelled respectively with shell (∘), beam (− −) and VUEL BM3D elements (—). Colours are used to differentiate among the three displacement components.

tude ($\Delta U \approx 15\%$), caused by the reduced ability of beam elements to model the pipe collapse, compared to shells. The results predicted with VUEL BM3D show a noticeable improvement in both terms, with the curves passing between those obtained with beam and shell elements. The improved prediction, compared to the standard beam elements, is due to the capability of the VUEL BM3D code of representing the collapse mechanisms through the hardening-softening moment-curvature relation. Nevertheless, compared to shell elements, the VUEL BM3D code makes simplifying assumptions in the modelling of the torsional behaviour and neglects any interaction between axial forces, bending and twisting moment.

A more thorough analysis of the mode of deformation of the L-shaped pipe whips is obtained by looking at the time history of the curvature and twisting angle along the pipe, as predicted with the three element types. In Figure 4.10, results are compared in terms of the quantity $k_n = \sqrt{{k_2}^2 + {k_3}^2}$, which represents the change in

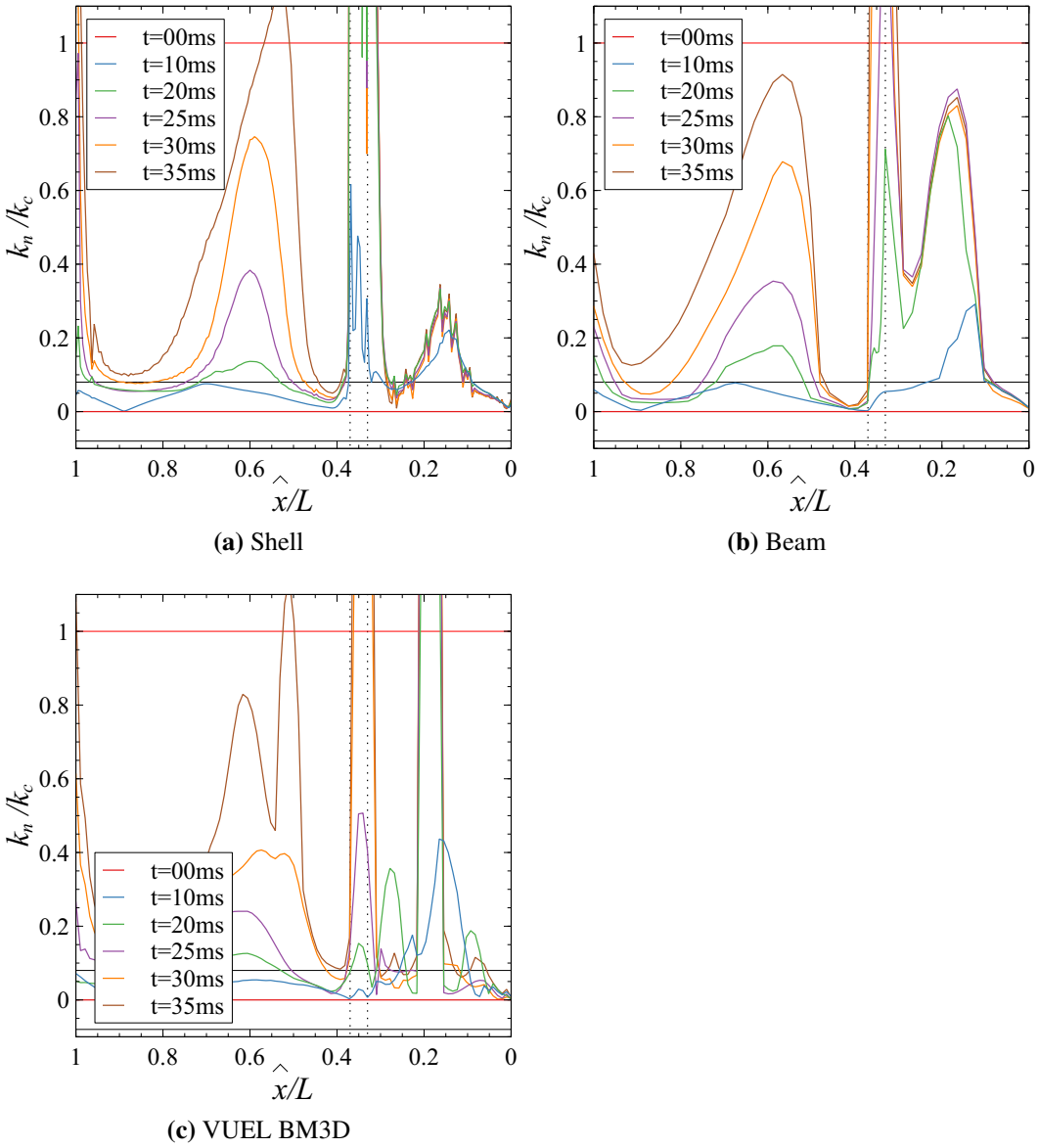

(a) Shell

(b) Beam

(c) VUEL BM3D

Figure 4.10: Distribution of curvature k_n along the pipe for out-of-plane pipe whips modelled in Abaqus/explicit with (a) shell, (b) beam and (c) VUEL BM3D elements. Vertical dotted lines highlight the elbow segment of the pipe, in the range of (dimensionless) axial coordinates $0.33 < \hat{x}/L < 0.38$.

curvature due to bending, divided by the maximum curvature k_c. On the horizontal axis, the symbol $\hat{x}/L$ is here used to represent the dimensionless axial coordinate, measured from the free end, and vertical dotted lines denote the extremities of the elbow segment, in the range $0.33 < \hat{x}/L < 0.38$.

Figure 4.10 (a) shows the curvature distribution predicted with shell elements up to 35 ms. At 10 ms, it is observed that k_n has already reached the yield value

(k_y, identified by a horizontal black line) at the elbow and in a point close to the tip ($\hat{x}/L \approx 0.15$). In the following time frames it is observed that $k_n > k_c$ in the whole elbow region, which corresponds to the formation of a plastic hinge, whereas the curvature distribution stays fixed in the segment AB. This corresponds to the behaviour observed in Figure 4.7 (a) with the collapse of point B, while the segment AB is seemingly straight.

Afterwards, the formation of two plastic hinges is observed at $\hat{x}/L = 1$ and $\hat{x}/L \approx 0.55$ at 30 ms and 35 ms, respectively. After this point, the last plastic hinge grows to envelop the whole segment BC, which is coherent with the intense deformation and collapse observed in Figure 4.7 (c-f).

It must be noted that the plot of the curvature for shell elements is afflicted with heavy noise in the region adjacent to the tip. This is due to the way by which the cross-sectional curvature is measured by the software when using shell elements, which requires the averaging of the curvature values extracted from all the elements belonging to a cross-section.

The results obtained with beam elements are shown in Figure 4.10 (b). The results agree with those obtained with shell elements in terms of position of the plastic hinges, but perceptible disagreement is observed in terms of k_n/k_c and time response. The hinge at $\hat{x}/L \approx 0.55$ forms with a delay of 5 ms, which corresponds to the phase delay observed in the U plot in Figure 4.9; the curvature at $\hat{x}/L \approx 0.15$ reaches values much higher than those observed in Figure 4.10 (a), whereas the values are much lower at $\hat{x}/L = 1$. The slower development of the hinge is interpreted as the cause of the phase delay in Figure 4.9 which, combined with the curvature variation, contributes to the different tip displacement. Nevertheless, considering the limitations of beam elements —that is, the inability to capture softening mechanisms in bending— the model achieves acceptable results, especially if one considers the extreme simplicity and computational inexpensiveness of such a model, compared to one using shell elements.

Lastly, the curvature distribution obtained with VUEL BM3D elements are shown in Figure 4.10 (c). In this model, the plastic hinges are successfully predicted

at $\hat{x}/L \approx 0.35$, $\hat{x}/L \approx 0.55$, $\hat{x}/L = 1$, improving on the results obtained with beam elements. However, the model overpredicts the curvature magnitude at $\hat{x}/L \approx 0.15$ with the formation of a plastic hinge at 20 ms. This behaviour corresponds to what observed in Figure 4.8 which shows a relatively small bend between the elbow and the free end.

Plots of the distributions of dimensionless twist angle, k_1/k_p, are shown in Figure 4.11 (a-c). According to the shell model, Figure 4.11 (a), three plastic hinges form simultaneously at $\hat{x}/L = 0.33$, 0.65 and 1, which then propagate over time. The beam model, Figure 4.11 (b), predicts the formation of a single hinge at $\hat{x}/L = 0.7$, followed by two more hinges at the ends of the member. The VUEL BM3D model, Figure 4.11 (c), predicts instead the simultaneous formation of many hinges in the region $\hat{x}/L = 0.33$–1. It must be noted that the plot in Figure 4.11 (a) is affected by extreme levels of noise, especially in the region $\hat{x}/L = 0$–0.35 which compromises the reliability of the shell model. As previously discussed, this phenomenon is the result of the way Abaqus evaluates the value of k_1 at each cross-section from those of the elements that compose it.

The study is completed by comparing the computational costs of the three models. The simulation with beam elements runs in less than 1 min, whereas the one with VUEL BM3D elements, mainly due to the cost of writing the results on an external file at any time increment, has a completion time of 11 min. Lastly, the completion time of a simulation with shells runs longer than 1 hour, and can only be reduced when using multiple parallel units (for example, its cost reduces to 12 min when using up to 40 units).

The simulation with VUEL BM3D is therefore up to 5 times faster than the shell element analogous. Although the cost reduction is relatively small, with respect to the 88 times reduction measured in the 2D case, the new model constitutes a valid alternative to the benchmark model, thanks to its ease of application.

In the case examined, the beam model was able to achieve good results in predicting the twist and the location of plastic hinges. However, the limitation of the element in modelling the deformation in bending leads to less accurate predictions of

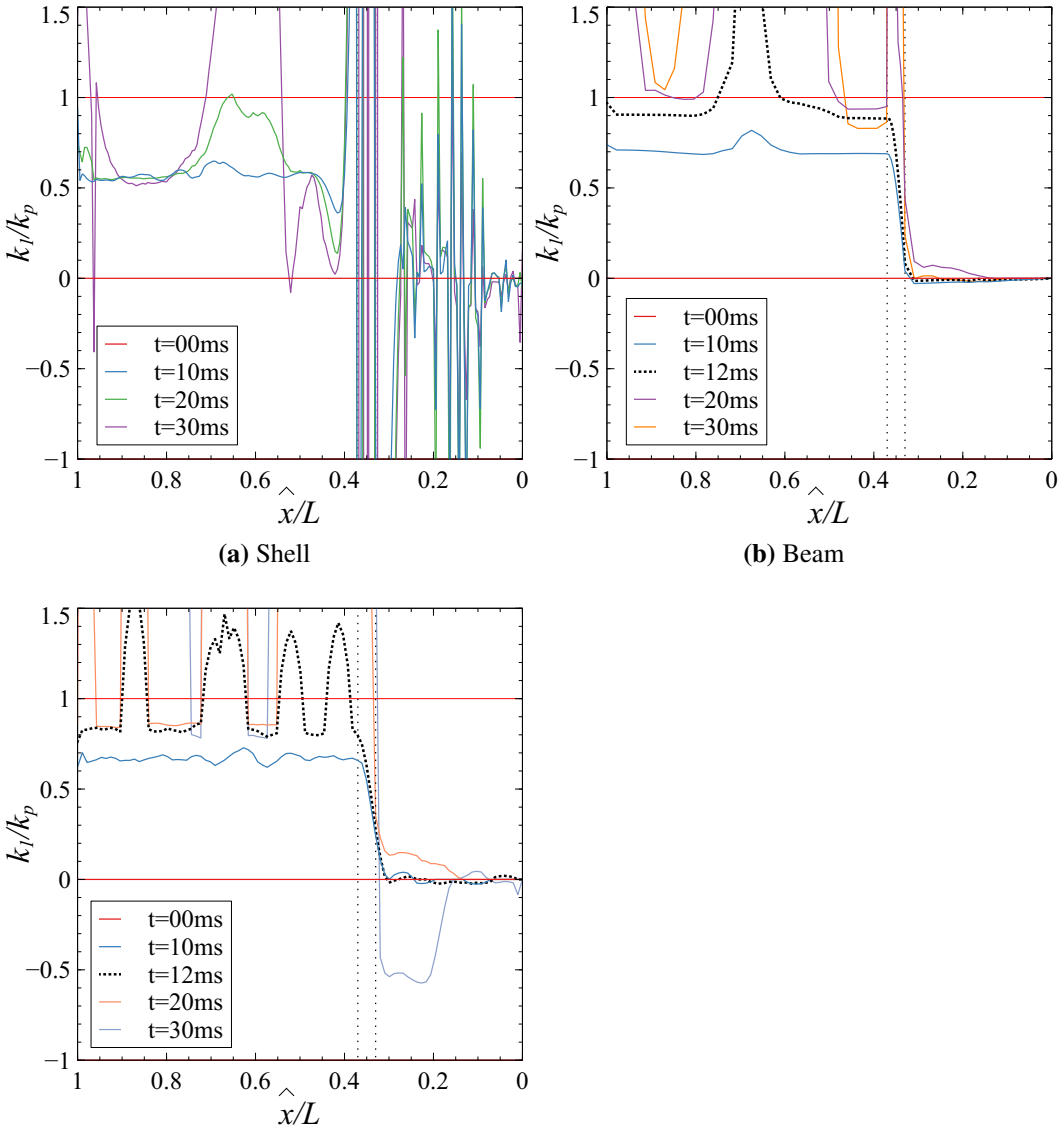

(a) Shell

(b) Beam

(c) VUEL BM3D

Figure 4.11: Distribution of dimensionless twist angle k_1 along the pipe for out-of-plane pipe whips modelled in Abaqus/explicit with (a) shell, (b) beam and (c) VUEL BM3D elements. Vertical dotted lines highlight the elbow segment of the pipe, in the range of (dimensionless) axial coordinates $0.33 < \hat{x}/L < 0.38$.

the tip displacement, which is necessary for a correct estimation of the hazard zone. The VUEL BM3D element, in its current state, presents a noticeable improvement in the results. Taking in consideration the achievement of the VUEL BM2D in the in-plane simulations, additional modifications to the constitutive models employed in the VUEL BM3D have the potential of further improving the results, whilst optimisations of the code can further reduce the computational cost.

Additional studies, aimed at improving the accuracy of the model, should be dedicated to including an interactive yield criterion between axial forces, bending moments and twisting moment. Contrary to the 2D case, where the axial forces were negligible and did not affect the results, it has been observed that in 3D the axial stress reaches up to 60% of the yield strength. A general interactive criterion can be represented by the yield surface

$$\left(\frac{N}{N_P}\right)^a + \left(\frac{M}{M_P}\right)^b + \left(\frac{T}{T_P}\right)^c = 1\,, \tag{4.70}$$

where the values of the exponents need to be found. In the absence of torsion, $a = 2$, $b = 1$ and the last term on the left-hand side vanishes [8]. In the presence of torsion, however, the term cannot be neglected and, at each increment where plasticity occurs, the above equation must be solved iteratively to find the combination of N, M and T that respects the yield surface.

The model could be improved further by implementing the effects of softening and the dependence of the torsional constitutive relation on the strain rate. All of the aforementioned modifications must be subjected to thorough testing and validated against purposely obtained experimental data.

4.6 Summary

In this chapter, the corotational beam element VUEL BM2D, previously applied to the simulation of planar pipe whips, has been modified to study the deformation in space of out-of-plane pipe whips. The upgraded element code, VUEL BM3D, required the implementation of a constitutive relation for torsion, and a more comprehensive kinematic formulation capable of manipulating three-dimensional ro-

tation tensors. A numerical model employing the VUEL BM3D element has been benchmarked against simulations of out-of-plane pipe whips performed in Abaqus/-explicit using traditional shell and beam elements, demonstrating its capability to predict the pipe hazard zone and the development of hinges when bending and twisting occur simultaneously. At the current stage, the VUEL BM3D element displays a significant increase in computational cost compared to its 2D counterpart. The code offers the potential to be enhanced by employing faster algorithms for many of its subroutines, in particular those dedicated to the constitutive relations and the input/output of data.

Chapter 5

Modelling of plastic deformation and failure of thin-walled plates

5.1 Introduction

The previous chapters have dealt with the development of numerical models for the investigation of the dynamic response of thin-walled pipes. In the present and following chapters, a shell-element model is developed for the simulation of thin metal plates deforming under the influence of explosive loadings.

As previously discussed in detail in Section 1.2.3, impulsively loaded plates show three typical failure modes, depending on the loading intensity, characterised by large inelastic deformations, the development of fracture surfaces, and detachment from the support. It has been determined that fracture and detachment are dictated by two competing damage mechanisms of ductile failure (induced on a microscopic level by the nucleation, growth and coalescence of imperfections in the material) and shear failure (caused by shear band localisation) [68]. Due to the complexity of the problem, theoretical models are not capable of assessing in detail the failure modes, and numerical analyses using advanced FE models are required [70].

The shell-element model here developed employs comprehensive damage criteria for predicting the failure modes of impulsively loaded plates. Experimental tensile and shear tests on steel specimens are performed to calibrate the damage

parameters, and numerical simulations reproducing the empirical tests are carried out to ascertain the element-size independence of the fracture mechanisms.

The plate model is validated against experimental data on steel plates by Olson et al. [56] and Nurick and Shave [55]. Based on the numerical results obtained, a new theoretical model is presented for predicting the loading threshold that separates the ductile-dominated and shear-dominated failure modes.

5.2 Material characterisation and failure models

The shell-element model employs strain-based failure criteria developed in the context of continuum damage mechanics. The initiation of failure is assumed to take place when the strain reaches a critical value, corresponding to the onset of necking. In FE modelling, this point is identified with the definition of a damage variable, $D(\bar{\varepsilon})$, so that

$$\begin{cases} D(\bar{\varepsilon}) = 0 & \text{before necking}\,, \\ 0 < D(\bar{\varepsilon}) < 1 & \text{after necking}\,, \\ D(\bar{\varepsilon}) = 1 & \text{at rupture}\,. \end{cases} \tag{5.1}$$

In the numerical model, the development of damage is represented by the gradual reduction of the element stiffness, based on the value of $D(\bar{\varepsilon})$, followed by the deletion of the element when $D(\bar{\varepsilon}) = 1$.

Two different damage variables, D_D and D_S need to be defined to capture separately the initiation and evolution of damage due to ductile and shear failure, respectively. The definition of these variables based on phenomenological criteria is discussed in the following paragraphs. The effect of the two damage variables is then combined as follows

$$D(\bar{\varepsilon}) = D_D D_S\,. \tag{5.2}$$

5.2.1 MMC damage initiation criterion

The initiation of ductile damage is represented by a function that correlates the true plastic strain at necking, $\bar{\varepsilon}_0$ (also called equivalent von Mises strain), with the stress

triaxiality, η [72, 73],

$$\bar{\varepsilon}_0 = \bar{\varepsilon}_0(\eta)\,. \tag{5.3}$$

Stress triaxiality is a variable that describes the loading conditions within a body, defined as the ratio of hydrostatic pressure, p, to the von Mises stress, $\bar{\sigma}$, [82, 83]

$$\eta = -\frac{p}{\bar{\sigma}}\,. \tag{5.4}$$

In particular, $\eta = 0$ indicates pure shear loading conditions, $\eta = 1/3$ and $\eta = 2/3$ identify uniaxial and equibiaxial tensile states, whilst $\eta = -1/3$ and $\eta = -2/3$ denote uniaxial and equibiaxial compression states, respectively.

Several phenomenological models are available in the literature to characterise equation (5.3) (see for example [84, 85]). The Modified Mohr-Coulomb (MMC) damage initiation criterion developed by Bai and Wierzbicki [72] and Li et al. [82] is here chosen for its proven effectiveness in a wide range of triaxiality, especially around $\eta = 0$ [83], which will be necessary in the modelling of plates for an accurate prediction of failure mode III, which is dominated by shear.

According to the MMC criterion, under the assumption of plane stress, equation (5.3) is expressed as [82]

$$\begin{aligned}\bar{\varepsilon}_0 = \Bigg\{ \frac{A}{c_2}\left[c_3 + \frac{\sqrt{3}}{2-\sqrt{3}}(1-c_3)\left(\frac{1}{\cos f_\eta} - 1\right)\right] \times \\ \times \left[\cos f_\eta \sqrt{\frac{1+c_1^2}{3}} + c_1\left(\eta + \frac{\sin f_\eta}{3}\right)\right]\Bigg\}^{-1/m}\,,\end{aligned} \tag{5.5}$$

where

$$f_\eta = \frac{1}{3}\arcsin\left[-\frac{27}{2}\eta\left(\eta^2 - \frac{1}{3}\right)\right]. \tag{5.6}$$

Equation (5.5) defines a fracture locus that depends on five material parameters, A, m, c_1, c_2, c_3 that need to be calibrated on experimental values of $\bar{\varepsilon}_0$ measured in a wide range of loading conditions. The fracture locus is then univocally determined once 5 material points of $(\bar{\varepsilon}_0, \eta)$ are known.

Table 5.1: List of experimental tests for the characterisation of the fracture locus of equation (5.3) [83].

Test type	Specimen Type		Triaxiality
	Prismatic	Round bar	η
Tensile, uniaxial	dog-bone	cylinder	$1/3$
Tensile, biaxial	flat with cut-outs	notched cylinder	$(1/3, 2/3)$
Tensile, equibiaxial	punch disk	-	$2/3$
Pure shear	simple shear	-	0
Combined shear and tension	butterfly	-	$(0, 1/3)$
Compression, uniaxial	-	cylinder	$-1/3$
Compression, equibiaxial	-	notched cylinder	$(-2/3, -1/3)$

The list of experimental tests originally indicated by Luo and Wierzbicki [83] for the calibration of the model parameters is reported in Table 5.1. The experiments involve complex specimen geometries (e.g. butterfly specimens) and require multiple machines for testing (tensile, punching and dual actuators loading frames) and measuring purposes (DIC). The original calibration process was therefore quite lengthy and expensive, severely limiting its practicality. However, Brünig et al. [84] and Driemeier et al. [86] observed that any series of tests that gives 5 combinations of $(\bar{\varepsilon}_0, \eta)$ can be used to characterise the fracture locus. Therefore, they proposed an alternative procedure solely based on the tensile testing of notched prismatic coupons, with the geometries reported in Figure 5.1 [87]. In the figure, R0 indicates a typical prismatic dogbone specimen, whilst R1.25, R2.5 and R.5 indicate prismatic specimens with a central notch radius $R = 1.25, 2.5, 5$ mm, respectively. Depending on the notch radius, the values of triaxiality $\eta = 0.58, 0.50, 0.43$ are obtained during the tensile tests in the central region of each specimen, where necking occurs [87, 68]. The last specimen (S) presents a special geometry that, when loaded under tension, allows to obtain pure shear conditions ($\eta = 0$) in the central region at the onset of fracture [84, 86].

5.2.2 Experimental tensile and shear tests

Following the procedure of Driemeier et al. [86], tensile experiments were carried out in the present work on mild steel specimens, grade S235. Five tests were per-

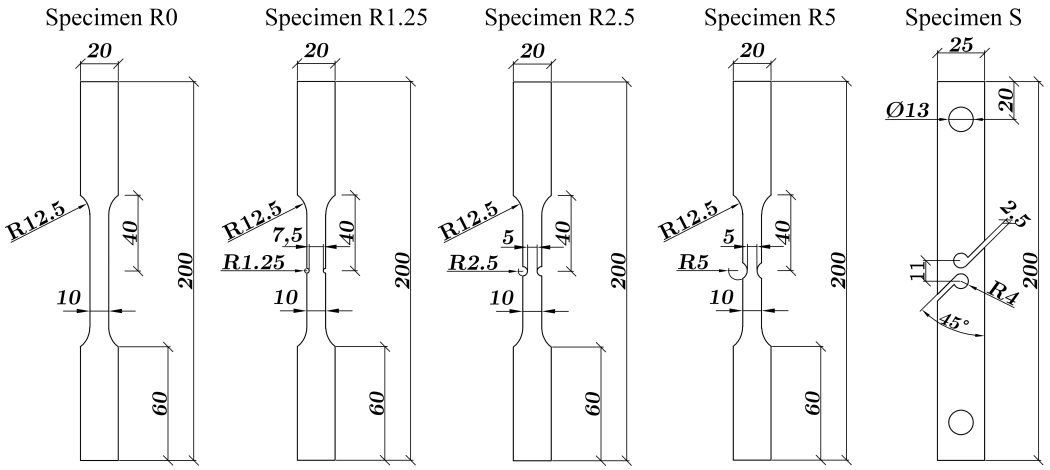

Figure 5.1: Geometries of un-notched (R0), pre-notched (R1.25, R2.5 and R5), and shear (S) specimens. The specimens have thickness 6 mm and initial gauge length of 50 mm. All dimensions are in mm. Reproduced with the author's permission from Faralli [87].

formed for each geometry (Figure 5.1) using an electromechanical testing machine (Instron, model 5985) at a constant cross-head speed of 0.05 mm/s. The first test performed was a uniaxial tensile test (geometry R0), carried out to measure the strain at necking $\bar{\varepsilon}_0(\eta = 1/3)$, the strength coefficient A and the strain hardening exponent n. The remaining MMC parameters, c_1, c_2, c_3, are then calibrated by fitting the experimental data of $\bar{\varepsilon}_0(\eta)$ obtained from the other geometries through equation (5.5).

The force-elongation (F-Δ) curves obtained from the experiments on steel S235 specimens for each notch radius are presented in Figure 5.2, where the labels R0, Rx and S follow the nomenclature introduced in the previous section. The measured values of nominal stress and strain are reported in Table 5.2, and the values of $\bar{\varepsilon}_0$ are reported in Table 5.3. Fitting equation (5.5) to the five material points of $(\bar{\varepsilon}_0, \eta)$, each corresponding to the necking point in one of the tensile tests (i.e. to the maximum point in the force-displacement curves of Figure 5.2) defines the fracture locus plotted in Figure 5.3, where the best-fit parameters for the MMC model were obtained as $A = 774.9$ MPa, $m = 0.274$, $c_1 = 0.033$, $c_2 = 273.6$ MPa and $c_3 = 1.016$.

Table 5.2: Nominal values of stress and strain for steel S235 obtained from uniaxial tensile tests.

	Yield	Necking	Rupture	Failure
σ (MPa)	242	411	302	0
ε (mm/mm)	$1.15 \cdot 10^{-3}$	0.29	0.46	0.47

Table 5.3: Values of true plastic strain at necking $\bar{\varepsilon}_0$ and stress triaxiality η from the experimental tests on steel S235.

Test type	η	notch radius (mm)	$\bar{\varepsilon}_0$
S	0	-	0.16
R0	0.33	-	0.25
R5	0.43	5.00	0.18
R2.5	0.50	2.50	0.15
R1.25	0.58	1.25	0.14

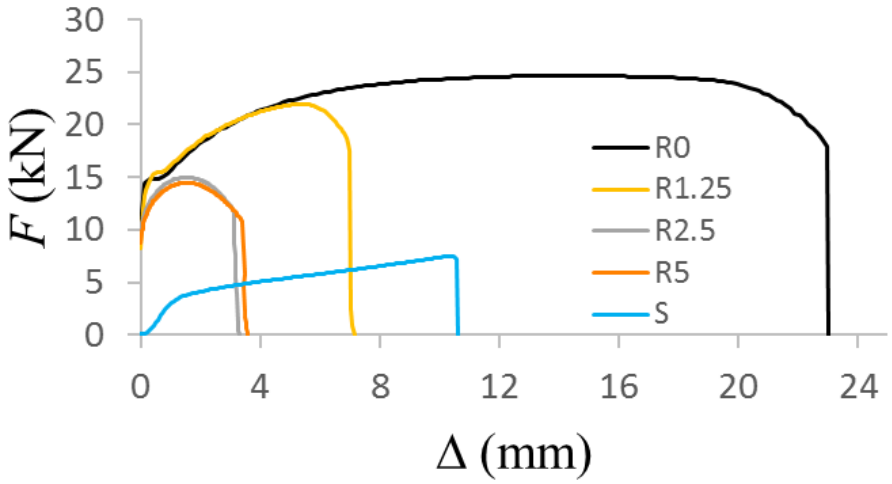

Figure 5.2: Experimental force-elongation curves (F-Δ) from the experimental tests on steel S235. R0 indicates tensile experiments on dumb-bell specimens, Rx represents tensile tests on notched samples, where x is the notch radius in mm, and S denotes the response of the shear specimen.

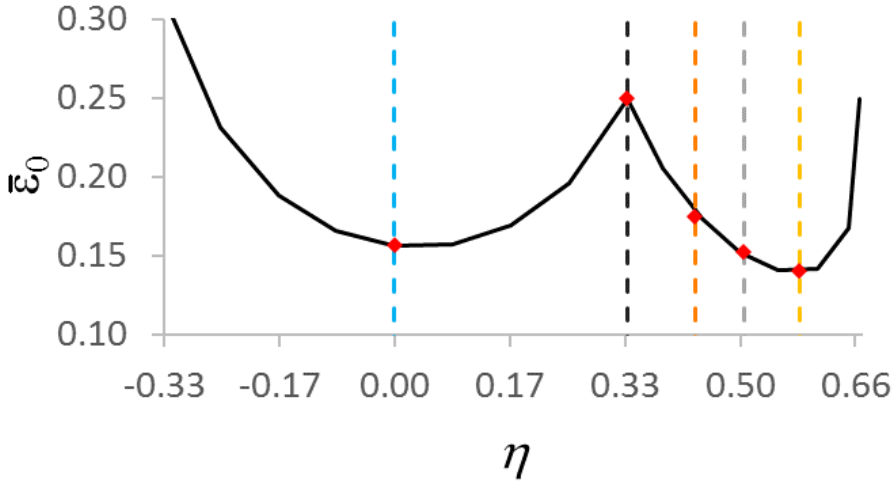

Figure 5.3: Fracture locus for steel S235 according to the MMC criterion, equation (5.5).

5.2.3 Calibration of damage evolution parameters

5.2.3.1 Ductile damage evolution model

Pavlović et al. [73] developed a phenomenological model to describe the evolution of the ductile damage after necking, used in FE analysis [16]. The model is based on the definition of a function correlating the element plastic elongation, $\bar{u}$, to the damage variable, D_D, evaluated from uniaxial tensile tests data using the following relation

$$D_D(\bar{\varepsilon}) = \begin{cases} 1.5\left(1 - \dfrac{\bar{\sigma}}{\bar{\sigma}'}\right) & \text{before rupture} \\ 1 & \text{after rupture} \end{cases} \tag{5.7}$$

with

$$\bar{\sigma}' = \begin{cases} \bar{\sigma} = \sigma(1+\varepsilon) & \text{before necking} \\ \sigma_N(1+\varepsilon) & \text{after necking} \end{cases} \tag{5.8}$$

where σ and ε are the nominal stress and strain, respectively, σ_N the value of stress at necking, $\bar{\sigma}$ is the true stress, and $\bar{\sigma}'$ the hypothetical value of true stress in the absence of damage [73, 88]. In the tensile tests, the point of rupture is defined as the last point in a nominal stress-strain curve before the complete loss of load-carrying capacity. It can be noted that before necking $D_D = 0$. After necking, the damage variable increases with the straining of the material, until the rupture point, where

$D_D = 1$ and the element is deleted from the FE model [16].

For the second part of the phenomenological model, the post-necking element plastic elongation, $\bar{u}$, is evaluated as [73]

$$\bar{u} = \frac{\bar{\varepsilon} - \bar{\varepsilon}_{\mathrm{N}}}{\bar{\varepsilon}_{\mathrm{F}} - \bar{\varepsilon}_{\mathrm{N}}} \bar{u}_{\mathrm{F}}\,, \tag{5.9}$$

with

$$\bar{u}_{\mathrm{F}} = \lambda_S \lambda_E L_E \left(\bar{\varepsilon}_{\mathrm{F}} - \bar{\varepsilon}_{\mathrm{N}}\right), \tag{5.10}$$

where L_E is the characteristic element length and the subscripts N and F are used to indicate values of true plastic strain at the points of necking and failure, respectively. Equation (5.10) introduces two extra parameters to remove the dependence of the plastic elongation at fracture, $\bar{u}_{\mathrm{F}}$, on the element size [16, 88]: the element-type factor λ_E and the mesh-refinement factor λ_S. The former is a constant that depends only on the element type, while the latter is a function of L_E with respect to a reference value $L_{E,0}$m,

$$\lambda_S = \begin{cases} 1 & \text{for } L_E = L_{E,0}\,, \\ f\left(L_E\right) & \text{for } L_E \neq L_{E,0}\,. \end{cases} \tag{5.11}$$

The two parameters are calibrated following an iterative procedure, developed by Pavlović et al. [73] for solid elements, perfected by Faralli et al. [88], and here adapted to shell elements, which involves FE simulations that reproduce the uniaxial tensile tests.

5.2.3.2 Simulation of tensile tests

Numerical simulations modelling the tensile tests of the specimen type R0 were performed in Abaqus/standard to calibrate the ductile damage evolution parameters λ_E and λ_S. The material, steel S235, had the following properties: density $\rho = 7850$ kg/m^3, elastic modulus $E = 210$ GPa, Poisson's coefficient $\nu = 0.33$. Metal plasticity was modelled in Abaqus using a piece-wise linear approximation of the true stress strain curve obtained from the force-displacement curve extracted

from the tensile experiment (curve R0 in Figure 5.2) with 31 discretisation points [68, 88]. Other material properties are reported in Table 5.2. Strain-rate dependence of the material was implemented by using the Cowper-Symonds model

$$\bar{\sigma}(\bar{\varepsilon},\dot{\bar{\varepsilon}}) = \bar{\sigma}_0(\bar{\varepsilon})\left(1+\left|\frac{\dot{\bar{\varepsilon}}}{\dot{\varepsilon}_0}\right|^{1/q}\right), \tag{5.12}$$

where $\dot{\bar{\varepsilon}}$ represent the true plastic strain rate, $\bar{\sigma}_0$ the true stress measured in quasi-static condition, $\dot{\varepsilon}_0 = 40.4\ \mathrm{s}^{-1}$ and $q = 5$ are the commonly accepted value of the strain-rate dependence parameters for mild steel [55]. The ductile damage model, equations (5.7)-(5.9), was implemented in Abaqus in the form of tabular data of $(D_D, \bar{u})$.

The R0 specimen had the dimensions reported in Figure 5.1, initial gauge length of 50 mm and thickness of 6 mm. The specimen had fully-clamped boundary conditions at one end and a prescribed displacement with constant velocity of 0.05 mm/s at the other end. The displacement in the direction of the thickness was constrained for the whole specimen. The sample was modelled using a uniform distribution of small square shell elements (element type S4R [16], aspect ratio 1), with no less than 8 elements discretising the smallest dimension (the gauge width of 10 mm). The simulations were carried out several times with different degrees of mesh refinement to verify the mesh insensitivity of the damage models. Although the body was loaded under plane stress conditions, shell elements needed to be used for the simulation of the tensile tests for the calibration of the model parameters necessary required by the damage model employed in the simulation of plate fracture under explosive blasts.

The parameters λ_S and λ_E were calibrated with the following iterative procedure. In the first step, the reference element size $L_E = L_{E,0} = 0.5$ mm is chosen. Following equation (5.11), $\lambda_S = 1$ is fixed and the value of λ_E is found iteratively. The initial guess value $\lambda_E = 2.5$ [73] is used to evaluate the ductile damage evolution law $(D_D, \bar{u})$, equations (5.7)-(5.9), which is employed in the first simulation run. The predicted nominal stress-strain curve is then compared with the exper-

imental data. The guess value of λ_E is considered satisfactory if the percentage difference between the numerical and experimental rupture strain, $\delta(\varepsilon_R)$ is lower than 3%; otherwise λ_E is modified by ± 0.1. The law $(D_D, \bar{u})$ is re-evaluated, based on the new λ_E value, and the simulation is repeated.

Once the value λ_E is found that satisfies $\delta(\varepsilon_R) < 3\%$, the simulation is repeated using a new mesh with element size $L_E = L_{E,1}$. In this second step, λ_E is fixed, and the value of λ_S is found iteratively. The first guess value is assumed as $\lambda_S = (L_{E,0}/L_{E,1})^{1/3}$ [73]. The simulation is performed again and the predicted rupture strain is compared to the experimental data. The value of λ_S is modified by ± 0.01 until $\delta(\varepsilon_R) < 3\%$.

After the first two steps are completed and λ_E and λ_S are identified for the reference element size, the simulation and the calibration procedure are repeated for a new model with a refined mesh. The second step is reiterated for five element sizes $L_{E,i}$ until five values of λ_S are found. A second order polynomial is then used to correlate λ_S to L_E. The element size considered in this study are $L_{E,0} = 0.5$ mm and $L_{E,i} = [1.25, 1.00, 0.20, 0.10]$ mm. The calibrated damage parameters are $\lambda_E = 2.8$ and $\lambda_S = 0.118 {L_E}^2 - 0.4768 L_E + 1.2126$.

The nominal stress-strain curve measured experimentally and the curves predicted for different values of L_E are compared in Figure 5.4. The mesh sensitivity of the ductile damage model is satisfactory in the entire range of L_E analysed, as testified by the percentage error on the strain at rupture, ε_R, which resulted always

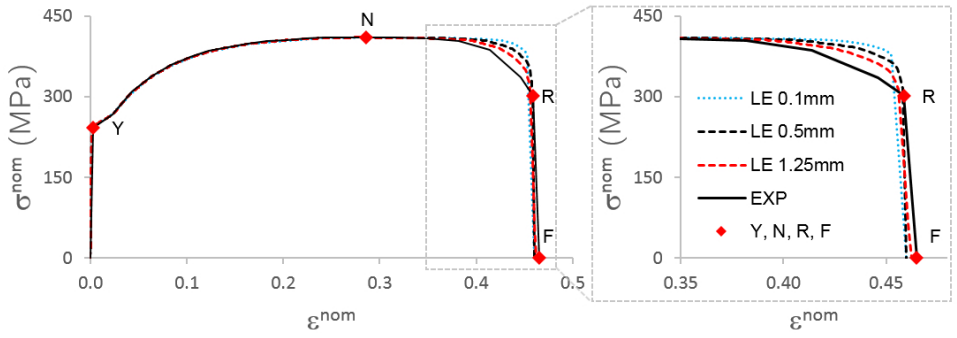

Figure 5.4: Comparison between the experimental nominal stress-strain curve (labelled EXP) from the uniaxial tensile test on steel S235, and the numerical predictions for the element sizes $L_E = 0.1, 0.5, 1.25$ mm.

smaller than 3%.

5.2.3.3 Shear damage evolution model

The model for the initiation of shear damage assumes that the strain at the onset of damage depends on the shear stress ratio, τ_S, which is defined as a function of stress triaxiality [16]

$$\tau_S = (1 - k_S \eta) \frac{\bar{\sigma}}{\tau_{\max}} \tag{5.13}$$

where $k_S = 0.1$ is a material constant [89]. The value of true plastic strain measured at the onset of damage in pure shear (test type S) is $\bar{\varepsilon}_{0,S} = 0.56$, to which corresponds $\tau_S = 1.732$ [68]. Similarly to the ductile model, the shear damage evolution is modelled through a function correlating the additional damage variable D_S to the element elongation $\bar{u}$. The softening branch of the test curve S, reported in Figure 5.2, shows that damage evolves more rapidly in shear, compared to the slow evolution of ductile damage attributed to the softening branch of the tensile curve R0. For this reason, a linear damage evolution law $(D_S, \bar{u})$ was assumed in shear:

$$\begin{cases} D_S = 0, \bar{u} = 0 & \text{at necking}, \\ D_S = 1, \bar{u} = \bar{u}_{\mathrm{F},S} & \text{at failure}. \end{cases} \tag{5.14}$$

In the expression above, the element elongation at failure in shear, $\bar{u}_{\mathrm{F},S}$, is a parameter that depends on the element size and needs to be calibrated iteratively through the simulation of the shear test.

5.2.3.4 Simulation of shear tests

The shear test simulations use the same material model described earlier in this section. The central region of the S specimen was discretised using square shell elements. Due to the extremely small width of the central region (≈ 3 mm, Figure 5.1), the model required a more refined mesh ($L_E \leq 0.13$ mm). The parameter $\bar{u}_{\mathrm{F},S}$ was calibrated with the following iterative procedure. In the first step, $L_E = L_{E,0} = 0.13$ mm is fixed, and the guess value of $\bar{u}_{\mathrm{F},S}$ is estimated as

$$\bar{u}_{\mathrm{F},S} = L_{E,0}(\bar{\varepsilon}_{\mathrm{F},S} - \bar{\varepsilon}_{\mathrm{N},S}) \tag{5.15}$$

where $\bar{\varepsilon}_{F,S}$ and $\bar{\varepsilon}_{N,S}$ are the values of true plastic strain at failure and at necking measured in shear, respectively. The actual value of $\bar{u}_{F,S}$ is found iteratively when the condition $\delta(\varepsilon_{F,S}) \leq 3\%$ is satisfied. The process is then repeated for different element sizes, $L_E = [0.13, 0.12, 0.10, 0.09, 0.07]$ mm, and the fitting curve obtained is $\bar{u}_{F,S} = -1.1564{L_E}^2 + 0.1636L_E + 0.0055$.

Figure 5.5 shows the comparison between the numerical and experimental force-displacement curves, demonstrating that the shear damage model is mesh size independent in the range of element dimensions analysed. It must be noted that the two damage evolution models due to shear and ductile mechanisms neglect the effect of the rate of deformation. In all the simulations, the strain-rate effect is incorporated through the Cowper-Symonds law of (5.12) applied to the undamaged material behavior.

5.3 Modelling of metal plates

The material models used in the simulation of the tensile and shear tests, employing the calibrated damage parameters, were implemented in FE analyses, carried out in Abaqus/explicit, aimed at analysing the transient deformation of steel square plates subjected to impulsive loadings, which reproduced the experiments performed by

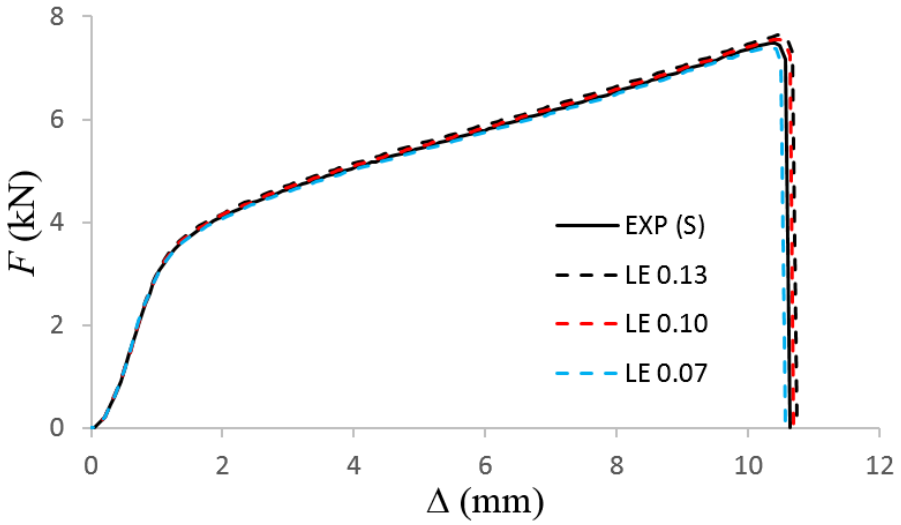

Figure 5.5: Comparison between experimental and numerical force-displacement curves for shear specimen (type S) made of steel S235. Numerical results are shown for the element sizes $L_E = 0.13, 0.10, 0.07$ mm.

Olson et al. [56] and Nurick and Shave [55]. In the experiments, thin square plates (width $L = 89$ mm, thickness $H = 1.6$ mm) were clamped between two rigid frames by means of high-strength bolts and exposed to blasts waves of various intensity generated by the detonation of explosive strips.

In the FE model here developed, the plate is discretised with a uniform distribution of square S4R shell elements (aspect ratio 1) with five integration points through the thickness. Based on the study of the deformation modes observed experimentally, it is assumed that the maximum deformation occurs at the plate centre, and that in the absence of local imperfection fracture should occur simultaneously along the four sides. Under this conditions the configuration is symmetrical and only one-quarter of the plate needs to be modelled. Based on the observations of Aune et al. [71], the supports were modelled with fully-clamped boundary conditions applied along the external edges, whilst symmetry conditions were imposed along the internal edges, as reported in Figure 5.6.

Previous studies [56, 70] have shown that the explosive blast duration, $15\,\mu$s, is much smaller than the average time necessary for the plate to reach maximum deformation, $120\,\mu$s. Under these conditions, the loading pulse can be idealised as

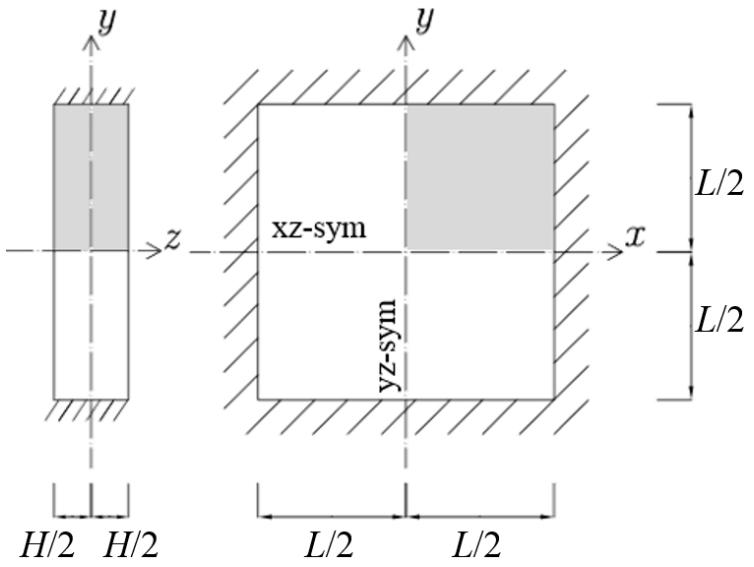

Figure 5.6: Side (left) and top (right) views of a thin square plate of length L and thickness H. One quarter of the plate is modelled (highlighted in grey), constrained by symmetry boundary conditions on the internal edges and fully-clamped supports on the exterior.

an instantaneous velocity field of initial velocity v_0 uniformly distributed across the plate surface [70]. The corresponding impulse intensity, in dimensionless form, is

$$I^* = v_0 \sqrt{\frac{\rho}{\sigma_Y}}, . \tag{5.16}$$

The mesh sensitivity study performed in the simulation of shear and tensile tests has shown that the damage model was independent of the characteristic element length and the mechanisms of propagation of failure through element deletion were mesh-size independent in a wide range of element size. A second mesh sensitivity analysis was carried out in the simulation of the metal plates, accounting for the convergence of strains at the mid-point along the plate edges (where strains reach maximum values) and the sensitivity of fracture to the element size. Mesh-size independence of the results is obtained for element lengths $L_E < 0.2$ mm. The final mesh size chosen is $L_E = 0.111$ mm.

5.3.1 Model validation

The plate model was validated against experimental data for mild steel square plates [55, 56]. The sequence of failure modes (mode I, II*, II and III) observed experimentally was successfully reproduced in the numerical model by varying the impulse intensity in the range $I^* = 0.5$-3, as depicted in Figure 5.7.

For each value of I^*, the permanent deflection measured at the centre of the plate, W (see Figure 5.8) was compared to experimental data. The results are plotted in dimensionless form (W/H) in Figure 5.9. For mode I, very good agreement is observed with the experimental data [55, 56] and also with analytical predictions using a strain-rate dependent, rigid-perfectly plastic model from Jones [65, equation 23 C]:

$$\frac{W}{H} = \left(1 + \frac{2\lambda}{3\lambda_0}\right)^{1/2} - 1 \tag{5.17}$$

with

$$\lambda = \frac{\rho A}{\sigma_Y} \left(\frac{v_0}{H}\right)^2 \tag{5.18}$$

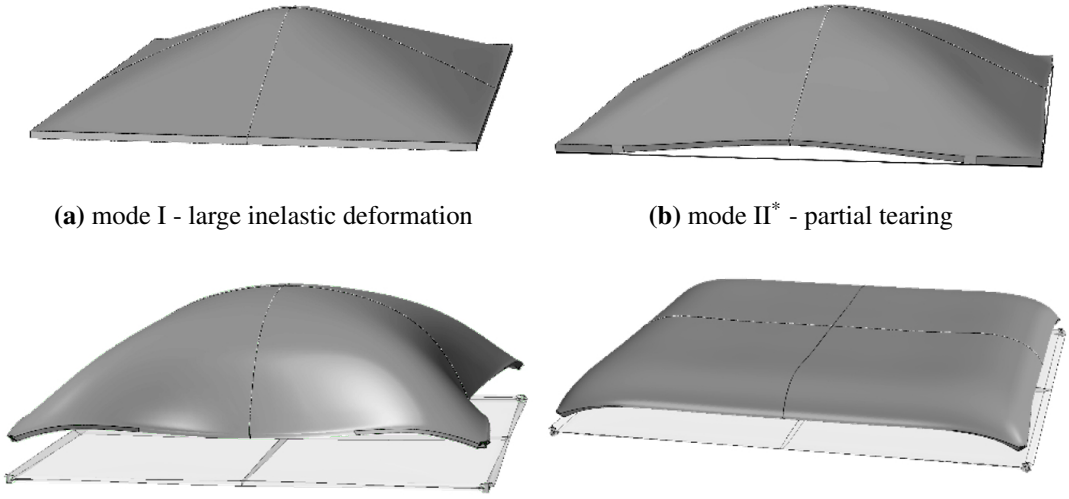

(a) mode I - large inelastic deformation

(b) mode II* - partial tearing

(c) mode II - tensile tearing

(d) mode III - transverse shear failure

Figure 5.7: Numerically observed failure modes of fully-clamped square plates under impulsive loads.

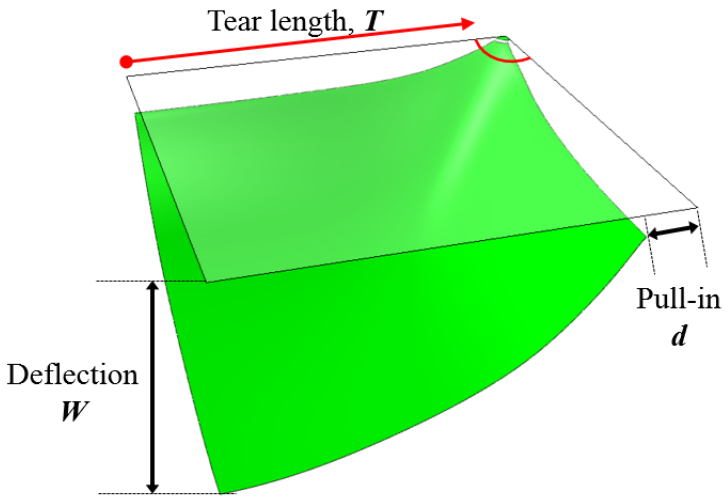

Figure 5.8: Measurements of permanent central deflection, W, lateral pull-in displacement, d, and tear length, T, in the plate simulations.

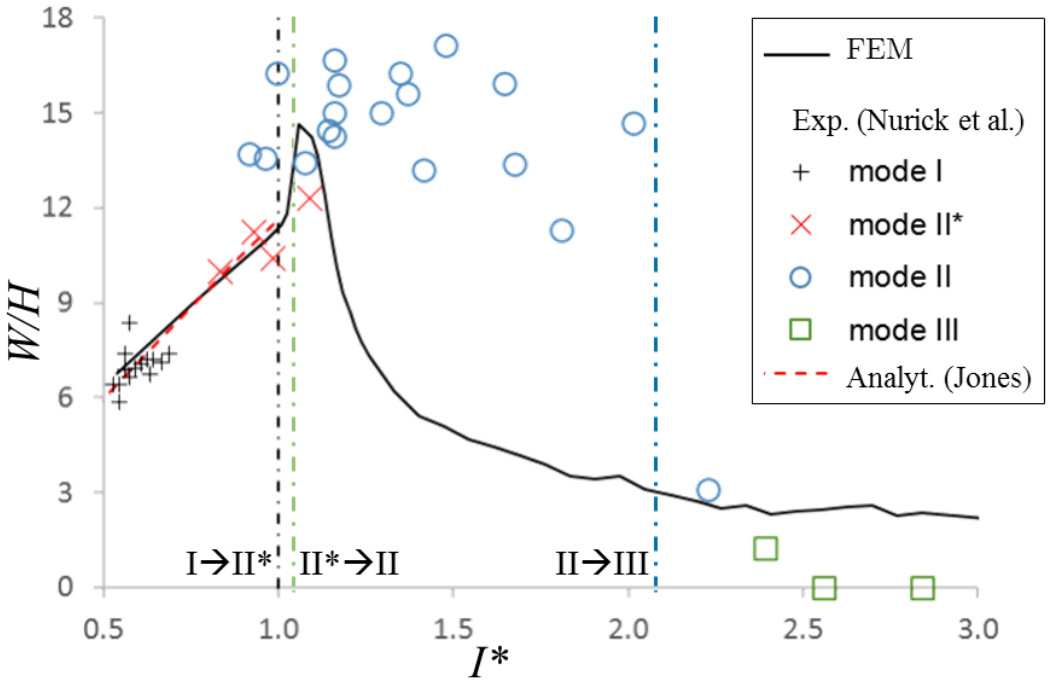

Figure 5.9: Maximum dimensionless central deflection W/H plotted as a function of dimensionless impulse I^*. Numerical predictions are compared against experimental data from Nurick et al. [55, 56] (labelled Exp.) and analytical predictions from Jones [65] (labelled Analyt). Vertical lines indicate the transition between failure modes predicted nomerically.

and

$$\lambda_0 = 1 + \left(4 \frac{2\rho}{\sigma_Y} \frac{v_0^2}{3\pi L \dot{\varepsilon}_0} \right)^{1/q}. \tag{5.19}$$

Using a linear regression for the central deflection measured experimentally in modes I and II* as reference, and comparing it to numerical predictions and the theoretical model of equation (5.17), the relative error was smaller than 2.7% in the range of impulse $I^* = 0.5$–1.0.

The FE model predicts a reduction of W/H for mode II with increasing I^*. In a previous numerical study, Yuan and Tan [70] suggested that the discrepancies between the numerical and experimental values of W/H can be explained by noticing that the central deflection is measured at different times in the experiments and FE models. The maximum deflection in FEM was evaluated at the moment of fracture, whereas the experimental values were obtained a posteriori, after the plate had hit a target. Rudrapatna et al. [69] have previously shown that, after complete

detachment, the plate deformation progresses as a result of the release of residual stored kinetic energy, highlighting the importance of the time of measurement of the central deflection.

Due to the difference in rupture strain between our model ($\varepsilon_R = 0.46$, steel S235) and the values reported in the experimental studies [55, 56] ($\varepsilon_R = 0.31$, mild steel), an increase in the critical impulse at the mode I-II* transition was observed, as expected.

Other quantities measured in the experiments [55, 56] were the tear length T (i.e. the length of cracks along the plate edge) in mode II*, and the pull pull-in displacement d in mode II (i.e. the inward in-plane displacement of the mid-side). The comparison with the numerical prediction is reported in Table 5.4, showing a general good agreement in terms of T and d in their respective failure modes.

5.3.2 Impulse threshold at the mode II-III transition

Nurick and Shave [55] and Olson et al. [56] observed that the onset of mode III occurs when the plate detaches from the support with a negligible central deflection, accompanied by a small value of pull-in displacement ($d \leq 1$ mm). However, Rudrapatna et al. [69, 62] suggested that the failure modes II and III are not individually dominated by tensile or shear failure, respectively; instead they observed an overlap of the two effects, with shear failure becoming predominant as the impulse intensity increases. Furthermore, they observed that mode III is also charac-

Table 5.4: Comparison between numerical results and experimental data [55, 56] of the tear length T for mode II*, and of pull-in displacement d for mode II.

	T_{EXP} (mm)	T_{FEM} (mm)
Average	66	61
Median	61	66
Maximum	80	80

	d_{EXP} (mm)		d_{FEM} (mm)	
	mode IIa	mode IIb	mode IIa	mode IIb
Average	5.8	3.5	5.4	2.9
Median	6.0	3.5	5.4	3.1

terised by instantaneous complete detachment and earlier failure times, compared to mode II [69]. For this reason, they came to the conclusion that a criterion for the onset of mode III based purely on the amount of deformation is highly subjective, and a more rigorous criterion must account for the time-evolution of the failure mechanism. This consideration is in agreement with our numerical results, which predict a gradual transition between modes II and III, as evidenced by the slow decrease of the central deflection at high impulses in Figure 5.9.

In light of these observations, a more rigorous definition of the critical impulse at the mode II-III transition is necessary, based on time-dependent quantities. In the simulations, the crack propagation velocity can be defined as the ratio between the crack length and the time interval from the initiation of fracture (identified by the deletion of the first element) to the moment of detachment.

In our FE results, it is observed that the numerically measured crack propagation velocity increases monotonically with I^*, varying from subsonic to supersonic values in the range of impulses where the transition is supposed to occur. Therefore, we propose a phenomenological criterion for determining the threshold value I^*_{II-III} based on the definition of the dimensionless crack speed

$$v^* = \frac{v_{\text{crack}}}{c}, \tag{5.20}$$

where

$$c = \sqrt{\frac{E(1-\nu)}{\rho(1+\nu)(1-\nu)}} \tag{5.21}$$

is the propagation velocity of pressure waves in solids. When $v^* \geq 1$, the plate response is categorised as mode III. The proposed criterion satisfies the conditions of $d \leq 1$ mm and of negligible W/H.

The corresponding predicted critical impulse for the analysed square plate is $I^*_{II-III,\text{FEM}} = 2.10$, which is in close agreement with the value established experimentally, $I^*_{II-III,\text{EXP}} = 2.39$ [55].

5.4 Summary

In this chapter, a finite element model has been presented for the prediction of the inelastic response of impulsively loaded quadrangular plates made of steel. The model incorporates two comprehensive failure criteria, based on a continuum damage mechanics approach, to capture the concurring ductile and shear failure mechanisms. The damage parameters were calibrated with a combined empirical and numerical procedure based on experimental data obtained from tensile and shear tests, ensuring the mesh insensitivity of the fracture mechanisms.

The plate model developed is then validated against experimental data for thin square plates [55, 56], showing a good agreement in the comparison of the permanent central deflection, the length of tears along the support and the edge displacement. Based on the numerical results, a novel criterion is proposed for predicting the critical impulse at the threshold between mode II and III, I^*_{II-III}. The criterion, based on the definition of the dimensionless crack speed, v^*, predicts that mode III initiates at $I^*_{II-III,\mathrm{FEM}} = 2.10$, when $v^* \geq 1$, in agreement with previous experimental findings. Further empirical studies measuring the crack propagation velocity with the use of optical techniques, such as high-speed digital image correlation (DIC), are required to demonstrate the accuracy of the criterion.

Chapter 6

Simulation of failure of metal plates

6.1 Introduction

This chapter deals with the numerical analysis of square and rectangular plates subjected to impulsive blast loading. The plate model, developed and validated in Chapter 5, is firstly employed to analyse the propagation of the detachment path and investigate the causes of its inward deviation observed experimentally in mode II and III [56, 55, 63]. The plate model is then employed in parametric studies aimed at investigating the impulsive response of fully-clamped square and rectangular plates of various size, and the failure modes of quadrangular plates constrained by simply-supported boundary conditions.

6.2 Prediction of the detachment path

The propagation of the crack path and the evolution of the stress triaxiality distribution in a square plate deforming in mode II ($I^* = 1.08$) is illustrated in Figure 6.1. As seen in Figures 6.1 (a) and 6.1 (b), in the FE model rupturing always initiates simultaneously at the midpoint of each boundary and propagates along the edges (this is in contrast to what was occasionally observed in [55, 57], where imperfections of the material or of the experimental apparatus induced rupture on less than four sides in some instances). Subsequently, the cracks rapidly propagate through most of the side; as time increases, the crack tips approach the corner, and the region under equibiaxial tension, which previously enveloped most of the plate, becomes smaller (Figure 6.1 (c)).

The instants immediately before and after complete detachment are displayed in Figures 6.1 (d, e, f), showing that the cracks deviate from their path, avoiding the region of equibiaxial tension, and propagate towards areas where $\eta \approx 0.5$. When two propagating cracks meet, the plate detaches from its support and flies away in the direction of the blast. It is of interest noticing that, in all simulations of square plates, the cracks deviation follows a diagonal path, similar to that observed experimentally [63].

Measurements of the dimensionless tear length, T/L, will be used in the following sections to determine the position at the crack deviation. The residual plate material that remains connected to the support after detachment can be identified by the residual length: $a = (T - L)/2$. It is possible to explain the deviation phenomenon by looking at the damage initiation curve of Figure 5.3: $\bar{\varepsilon}_0$ is maximum in uniaxial ($\eta = 1/3$) and equibiaxial tensile conditions ($\eta = 2/3$) and has local minimum points in shear ($\eta = 0$) and for $\eta \approx 1/2$. The material suffers a decrease in ductility in the areas of the plate where $\bar{\varepsilon}_0$ is reduced due to the loading conditions; therefore, lower energy is required for the propagation of the crack through regions where $\eta \approx 0$ or $\eta \approx 1/2$ [68]. A similar evolution of the η distribution is observed for mode III at high impulses. At lower values of I^*, corresponding to mode II*, the impulse intensity is not sufficient to cause complete detachment of the plate from its support, and the final state becomes similar to that shown in Figure 6.1 (c).

6.3 Parametric studies on square plates

Two parametric studies were performed to assess the effect of the plate thickness H and volume V on the inelastic response. In the first study, the thickness was varied in the range $H = 1.6$–6 mm whilst keeping the width constant ($L = 89$ mm) whereas, in the second study, H was varied in the same range whilst keeping the volume constant. The second study was repeated for several values of volume in the range $V = 12674$–47526 mm^3; the effect of the surface area A was then inferred by analysing the results obtained from plates with different V and the same H. According to the Kirchoff-Love theory, the aspect ratio L/H can be used to identify

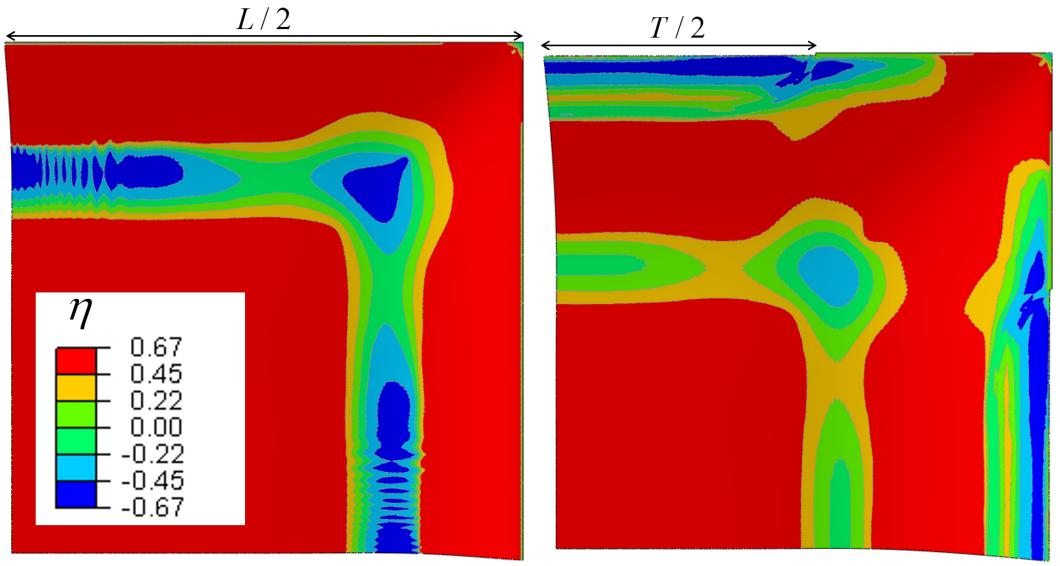

(a) Prior to rupture, $t = 1.8\text{e}{-5}$ s **(b)** Rupture, $t = 3.4\text{e}{-5}$ s

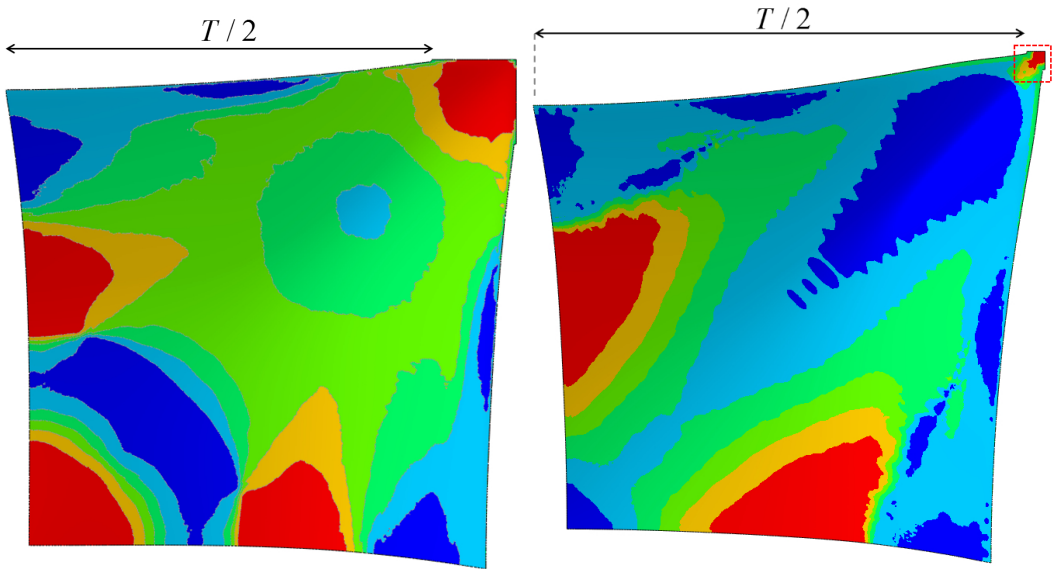

(c) Propagation, $t = 7.30\text{e}{-5}$ s **(d)** Deviation, $t = 11.2\text{e}{-5}$ s

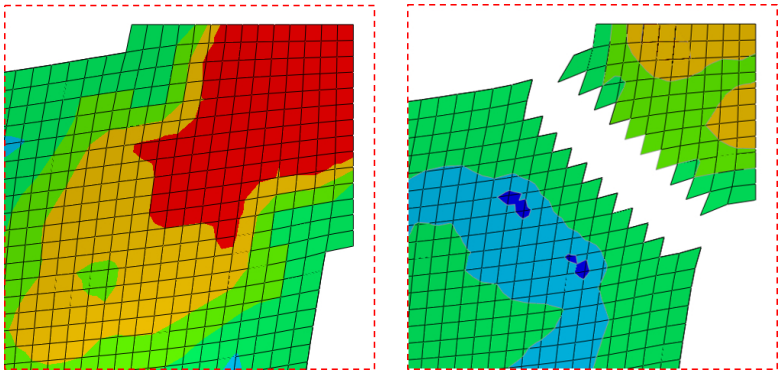

(e) Deviation (detail) **(f)** Detachment, $t = 11.4\text{e}{-5}$ s

Figure 6.1: Top view of square plates deforming in mode II under the dimensionless impulse $I^* = 1.08$. The images report the evolution of the stress triaxiality η distribution and of the tear length T.

a plate as thin or thick. In our studies, we focused on the analysis of thin plates, with values of the ratio selected in the range $L/H = 20$–56, and on few examples of relatively thick plates, with $L/H = 15$–20. The study did not consider thicker plates ($L/H < 15$), because an accurate analysis would require a model using solid elements, rather than shells.

The results of the first parametric study, in which the thickness varies in the range $H = 1.6$–6 mm whilst the width is kept constant ($L = 89$ mm) are presented in Figure 6.2. For all the cases analysed, the initiation of mode II* always coincided with the deviation of linearity between the dimensionless central deflection, W/H, and the dimensionless impulse, I^*, whereas the maximum deflection always corresponded to the initiation of mode II. As expected, increasing H reduces the capability of the plate to deform, thus decreasing significantly the central deflection Figure 6.2. This effect is more evident for relatively thick plates ($L/H \leq 20$), which show a pronounced flattening of the peak of W/H.

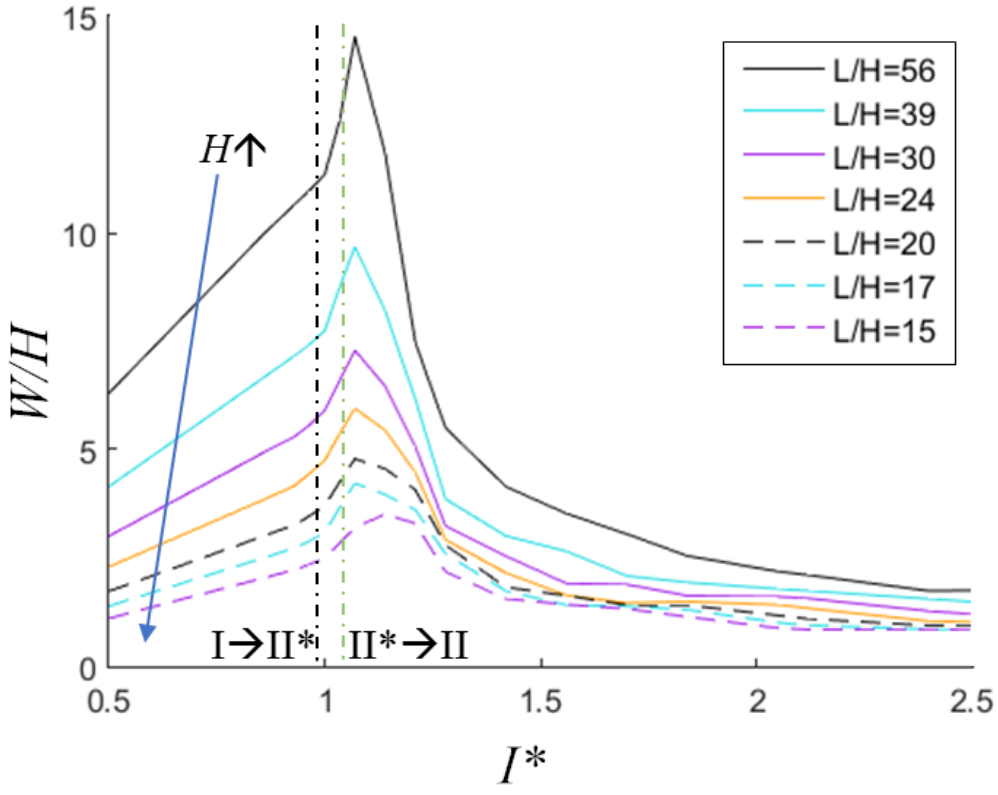

Figure 6.2: Numerical predictions of W/H for square plates from the first parametric study ($H = 1.6$–6 mm, $L = 89$ mm).

Dimensionless diagrams, named failure maps, are introduced in Figure 6.3 to analyse the boundaries between failure modes. The dimensionless variables L/H and I^* define a 2-D space which is divided into four regions, each corresponding to a different failure mode. Observing the failure map gives the combinations of loading intensity and aspect ratio that are safe (mode I) or expected to rupture (mode II*) or would, otherwise, incur into complete detachment (modes II and III). Figure 6.3 (a) shows that the boundaries between mode I-II* and mode II*-II are mostly unaffected by changes in thickness, since the initiation of damage depends only on the amount of strain accumulating along the support. On the contrary, the region belonging to mode III becomes smaller with H because, as the thickness increases, the plate is capable of absorbing more energy against the development of cracks, and the crack propagation velocity decreases(see equation (5.20)). The results of Figure 6.2 are then overlaid on the failure map in Figure 6.3 (a) as isolines of W/H.

Failure maps displaying the effect of the geometry on the tear length, as isolines of T/L, are shown in Figure 6.3 (b) for the first parametric study and in Figures 6.4 (a) and (b) for the second parametric study, in which $H = 1.6$–6 mm and $V = 12674, 47526$ mm^3.

An almost perfect correspondence is observed between the mode I-II* transition and the isoline $T/L = 0.34$, indicating that the minimum tear length at the onset of mode II* is independent of H and V. In the narrow range of impulses where mode II* occurs, T/L varies from 0.34 to 0.90. This implies that small increments in the impulse intensity correspond to large variations of the tear length for mode II*. It is worth noting that the isoline $T/L = 0.98$ passes through the mode III region, indicating that the crack deviation occurs even at high impulses, and a small amount of material remains connected to the support.

Numerical predictions have been compared in Section 5.3.1 with experimental data for a square plate of thickness $H = 1.6$ mm [55, 56]. Further comparisons against analogous data for plates of different thickness are required for the complete validation of the model and the failure maps, which could then be proposed for the use in plate design.

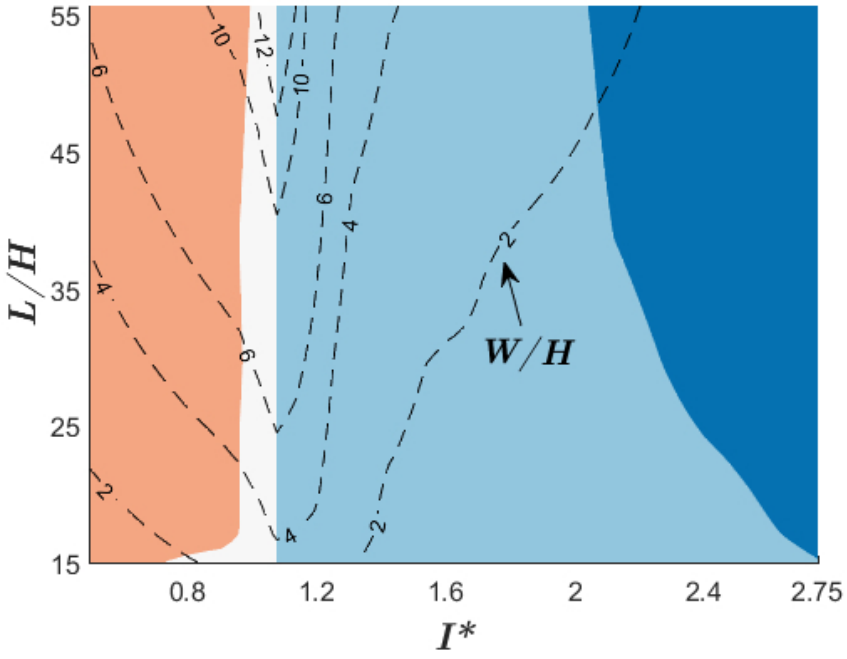

Figure 6.3: Failure maps for the first parametric study ($H = 1.6$-6 mm, $L = 89$ mm) displaying the boundaries between failure modes, overlaid with isolines of W/H (a) and T/L (b). Colours indicate, from left to right, the sequence of failure modes I, mode II*, mode II, and mode III.

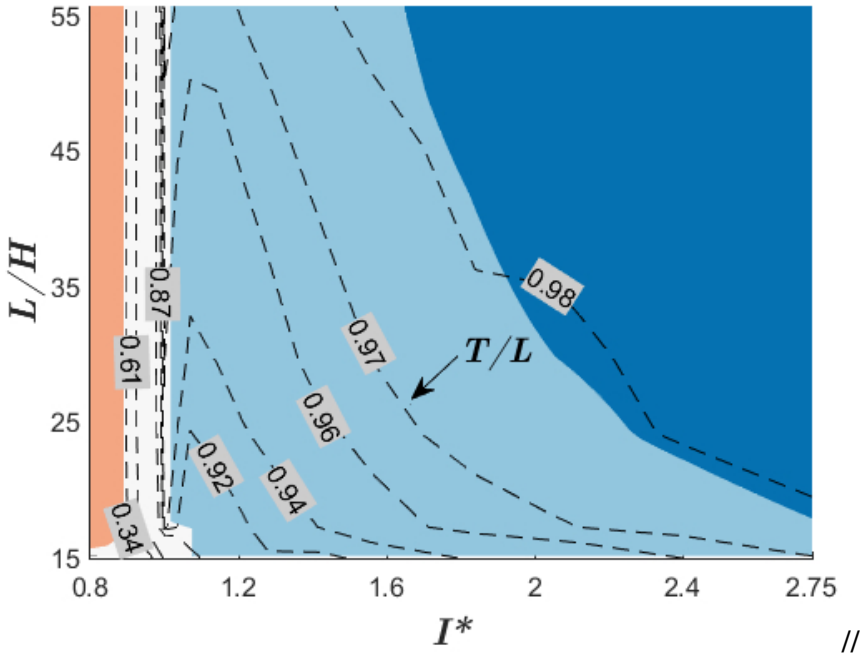

(a) $V = 12674$ mm^3

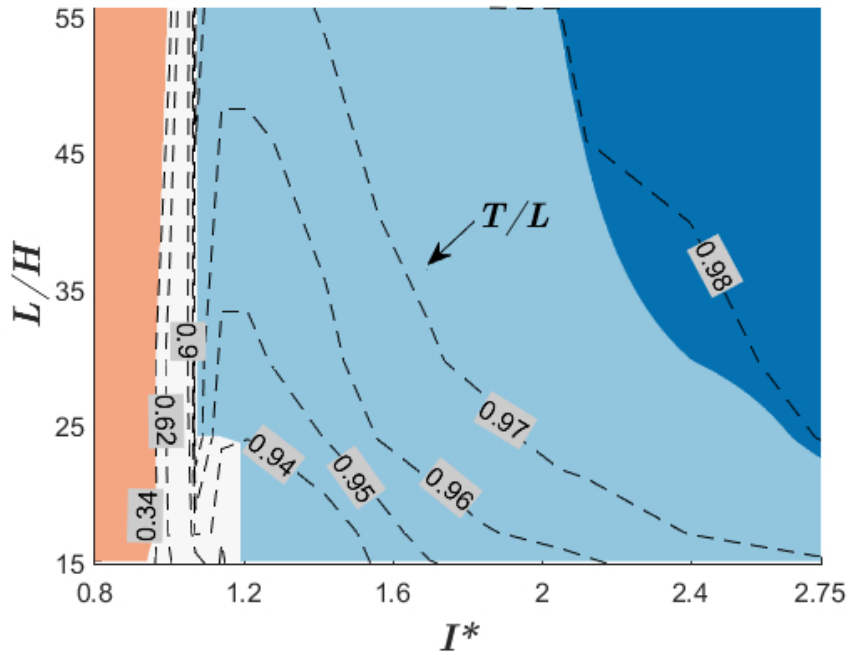

(b) $V = 47526$ mm^3

Figure 6.4: Failure maps of predicted T/L from the second parametric study, in which $H = 1.6$-6 mm, $V = 12674$ mm^3 (a) and $V = 47526$ mm^3 (b). Colours indicate failure mode I, mode II*, mode II, and mode III.

6.4 Parametric studies on rectangular plates

A numerical study was conducted to assess the response of fully-clamped rectangular plates loaded with impulsive blasts, adopting the plate setup illustrated in Figure 6.5. The rectangular plates have the same thickness $H = 1.6$ mm and surface area $A = 7921$ mm^2 of the square plates analysed in Section 5.3. The aspect ratio γ between the longer and the shorter side was varied in the range $\gamma = L_A/L_B =$ 1-5.

The simulated rectangular plates display mostly the same sequence of failure modes as the square plates. The only difference is observed in mode II* where, at low I^*, failure occurs only on the longer edge. The propagation of the crack path and the evolution of the stress triaxiality distribution in a rectangular plate deforming in mode II ($I^* = 2.7$) is illustrated in Figure 6.6.

When failure mode II or III occur, the crack propagation velocity is initially faster on L_A and slower on L_B. The two cracks propagate at different speed until the residual length on the long edge matches that on the short edge, $a \approx b$. Afterwards, the two cracks propagate at the same speed until detachment occurs. It is worth noting that the crack deviation follows a diagonal path with $a/b \approx 1$ for all combinations of γ and I^* studied, as illustrated in Figure 6.6. In the case of square plates,

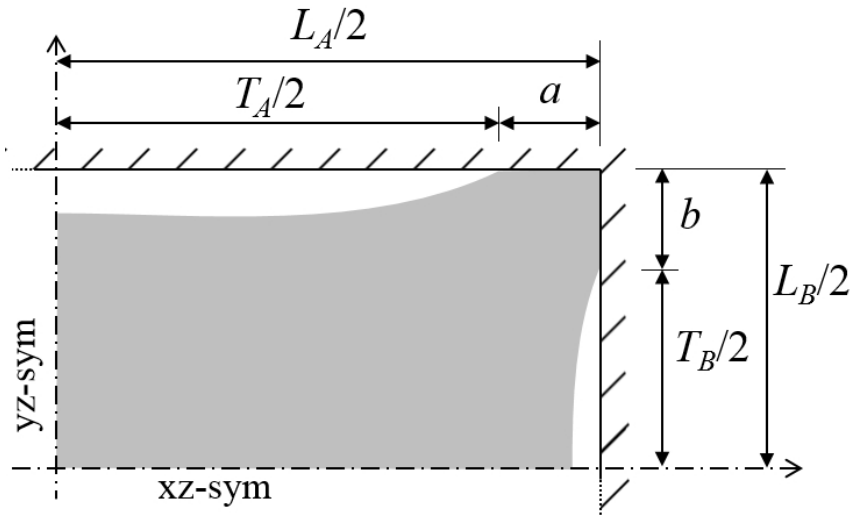

Figure 6.5: Top view of a thin rectangular plate with fully-constrained boundary conditions. One quarter of the plate is modelled, constrained with symmetry boundary conditions on the internal edges. The tear lengths on the longer and shorter sides are indicated with T_A and T_B, respectively.

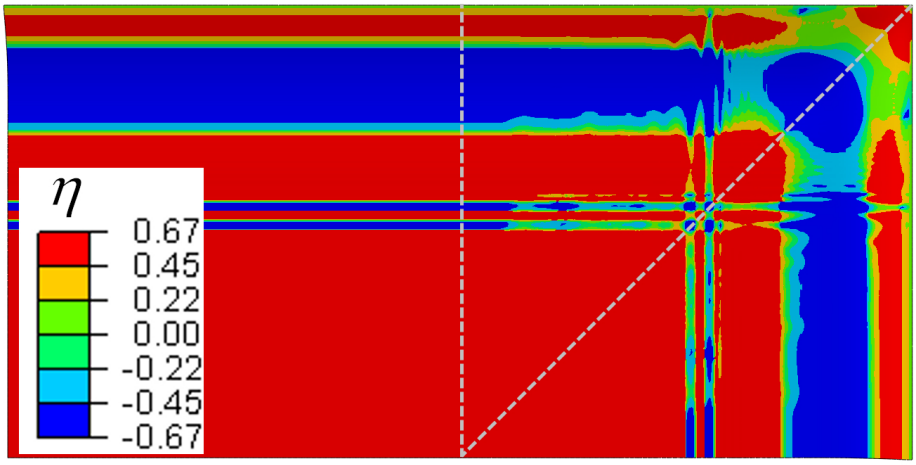

(a) Prior to rupture, $t = 0.4\text{e}{-5}$ s

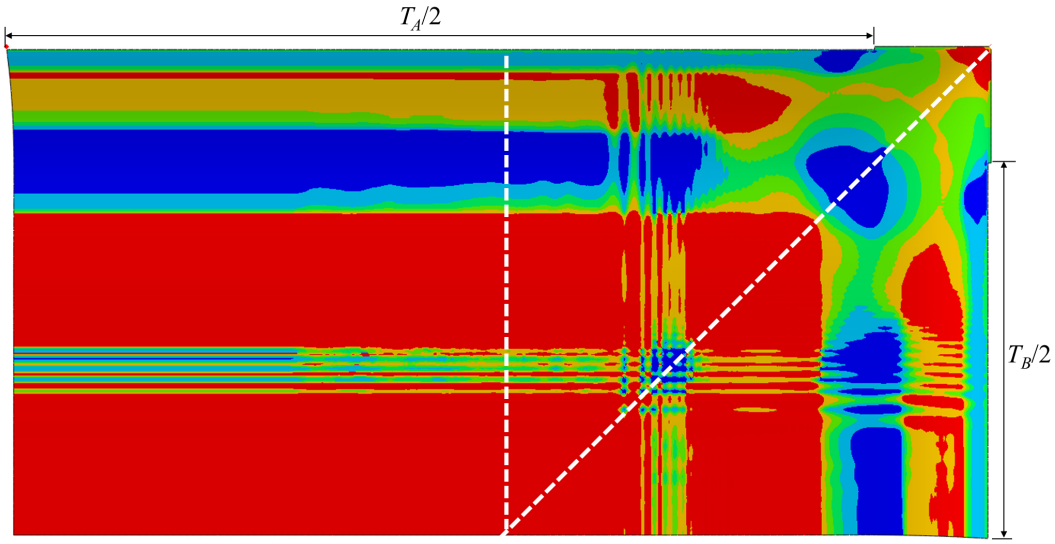

(b) After rupture, $t = 0.8\text{e}{-5}$ s

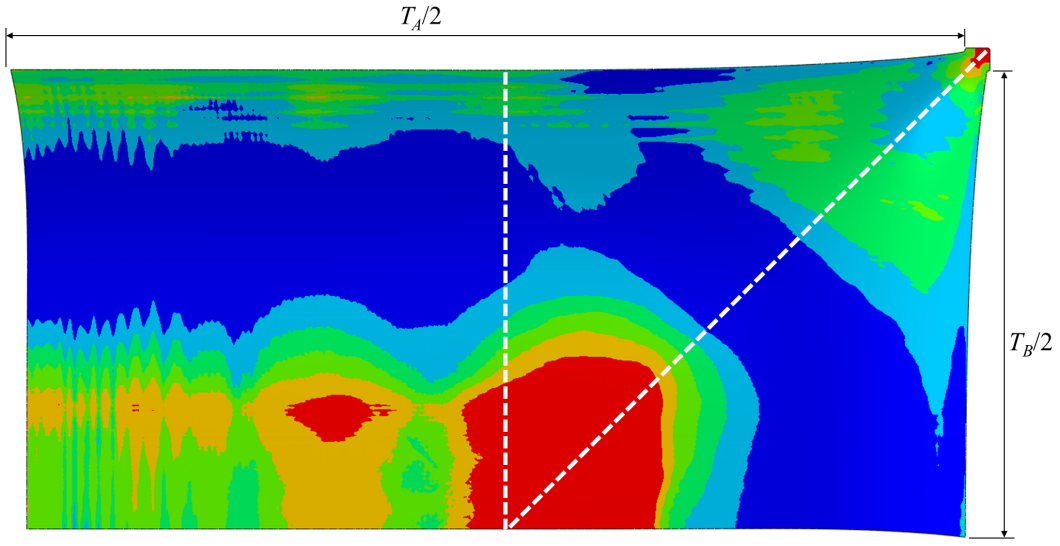

(c) Detachment, $t = 2.8\text{e}{-5}$ s

Figure 6.6: Time evolution of stress triaxiality η distribution for a rectangular plate with $\gamma = 2$ deforming in mode II ($I^* = 2.7$).

a and b were obviously equal because of the symmetry of the geometry. The reason why $a \approx b$ for rectangular plates is found by looking at the distribution of $\bar{\varepsilon}$ and η before fracture. It can be seen from Figure 6.6 that, because of the deformation profile assumed by rectangular plates [90, 91], the distribution's axis of symmetry does not coincide with the plate diagonal, but with a line inclined at 45° from the plate corner.

The predictions of permanent dimensionless deflection W/H for rectangular plates are shown in Figure 6.7. In mode I, W/H depends linearly on I^* for any γ, as expected, and decreases with increasing γ. The onset of mode II* occurs at $I^* \approx 1$, as in the case of the square plates, marking a sharp deviation from linearity. The deviation reaches maximum values at the onset of mode II ($I^* \approx 1.1$). In the figure, the failure modes are not marked on the curves to reduce cluttering on the plot. When γ increases, the peak height raises and its position shifts rightward to slightly higher values of impulse. A further increase of I^* corresponds to a rapid decrease of W/H, and the plates tend to the same amount of final deflection, regardless of the aspect ratio, for higher impulses, until negligible deflection is observed.

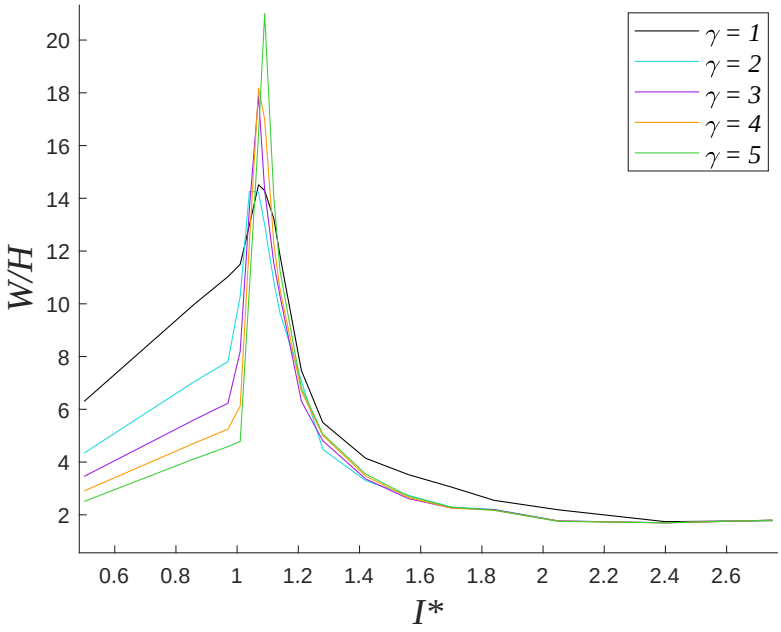

Figure 6.7: Numerical predictions of W/H for rectangular plates with fully-constrained boundary conditions and different aspect ratios $\gamma =$ 1-5.

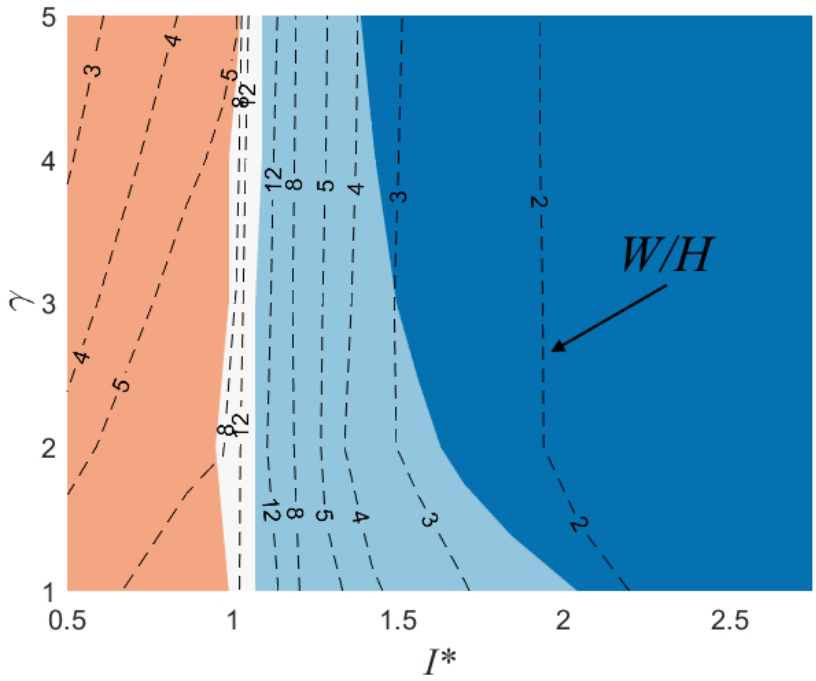

Figure 6.8: Failure map of predicted W/H for fully-constrained rectangular plates with different aspect ratios γ. Colours indicate failure mode I, mode II*, mode II, and mode III.

The boundaries between failure modes are displayed in the failure map of Figure 6.8. The narrow region of mode II* has almost vertical boundaries, which means γ has a negligible effect on the impulse threshold at the mode I-II* and II*-II transition. Furthermore, changing the aspect ratio shows no effect on the measured time to rupture and time to detachment, which remain constant. However, increasing γ correspond to increasing L_A, which determines a growth of the crack propagation velocity measured on L_A and, therefore, an enlargement of the mode III region. Figure 6.9 shows the failure map of the residual length on the long edge, T_A, divided by L_A. For all instances where detachment occurs (modes II and III), $T_A/L_A > 0.93$ and the residual length is negligible on both edges. Then, since $T_A \approx L_A$ and $T_B \approx L_B$, it is found that $T_A/T_B \approx \gamma$.

6.5 Failure of simply supported plates

Previous studies demonstrated that the failure modes can be affected significantly by changes in the boundary conditions [52]. For instance, Bonorchis and Nurick [57]

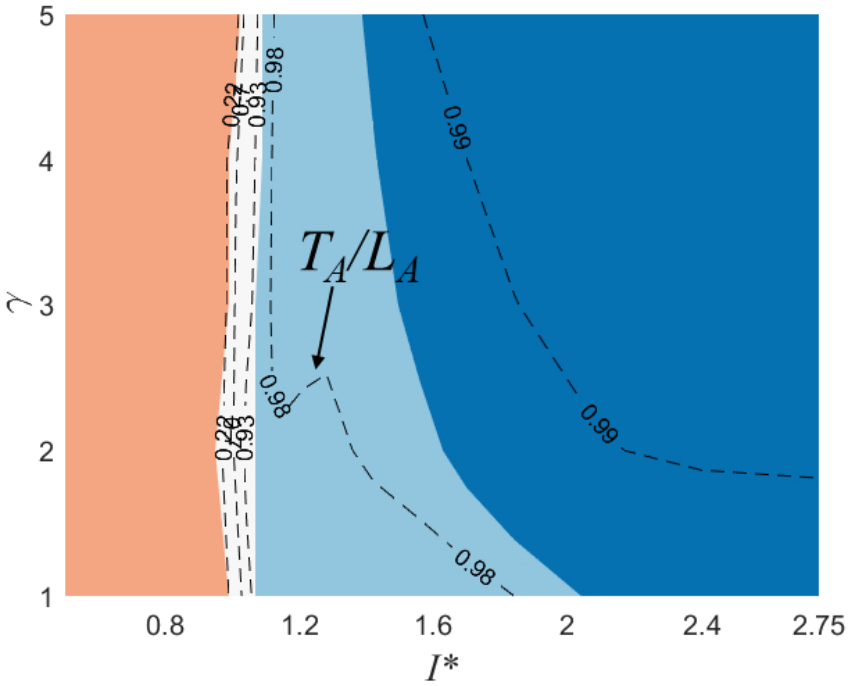

Figure 6.9: Failure map of predicted T_A/L_A for fully-constrained rectangular plates with different aspect ratios γ. Colours are used to identify failure mode I, mode II*, mode II, and mode III.

and Thomas [60] showed that plates with built-in or welded boundaries experience earlier failure, compared to fully-clamped plates, due to the increased rigidity of the boundary, which limits the in-plane displacement of the plate at its supports. In the literature, little attention has been given to the case of less rigid boundary conditions. For this reason, numerical studies were conducted to analyse the response of impulsively loaded metal plates with simply-supported boundary conditions, when the rotation of the plate at the supports is allowed.

It is expected that the additional rotational degrees of freedom affect the sequence of failure modes of quadrangular plates, influencing the impulse range for each mode, the amount of deformation, and the position of rupture. Starting from mode I, Figures 6.10 (a, b) compare the deformation profiles predicted numerically for square plates with different boundary conditions. In the case of fully-constrained boundary conditions, the profile resembles a uniform dome shape, whereas a more complex profile is observed for simply-supported boundary conditions, with a small central dome superimposed atop the global dome, joined by an inflection point. This

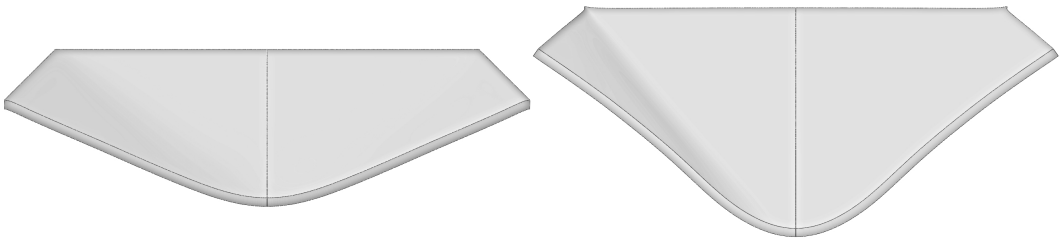

(a) Fully-constrained plate **(b)** Simply-supported plate

Figure 6.10: Comparison of the deformation profiles of square plates subjected to blast loadings deforming in mode I: (a) fully-constrained boundary conditions and (b) simply-supported boundary conditions.

behaviour resembles that observed experimentally for plates subjected to localised blast loadings [92, 52, 58, 61] which are characterised by a similar profile, as a consequence of a non-uniformly distributed velocity field.

The other failure modes found for simply-supported square plates are depicted in Figure 6.11. Increasing the impulse intensity, mode I is followed by a failure mode, different from the mode II* of fully clamped plates, characterised by partial tearing in the central region, labelled as mode II*c in Figure 6.11 (a). This is then followed by complete tearing in the central area, labelled as mode IIc Figure 6.11 (b), a response that is also known as 'capping' [52], which is normally observed for locally loaded plates. The amount of deformation and the capping area grow with the impulse intensity. Increasing the impulse further, complete tearing occurs along crack paths that run parallel to the plate edges, resembling failure mode II and III, respectively.

A different sequence of failure modes was observed for simply-supported rectangular plates ($\gamma = 2$–5), as displayed in Figure 6.12. By increasing the impulse intensity, mode I is followed by mode II*A, where partial tearing occurs on a path that runs parallel to the long edge, but no rupturing is observed along the short edge.

At higher impulses, the rupture mechanism deviates from its original path with a sharp angle and propagates towards the opposite edge, rather than towards the corner. Complete failure occurs when two crack path from opposite edges meet, causing the detachment of a large section of the plate. To the best of the authors'

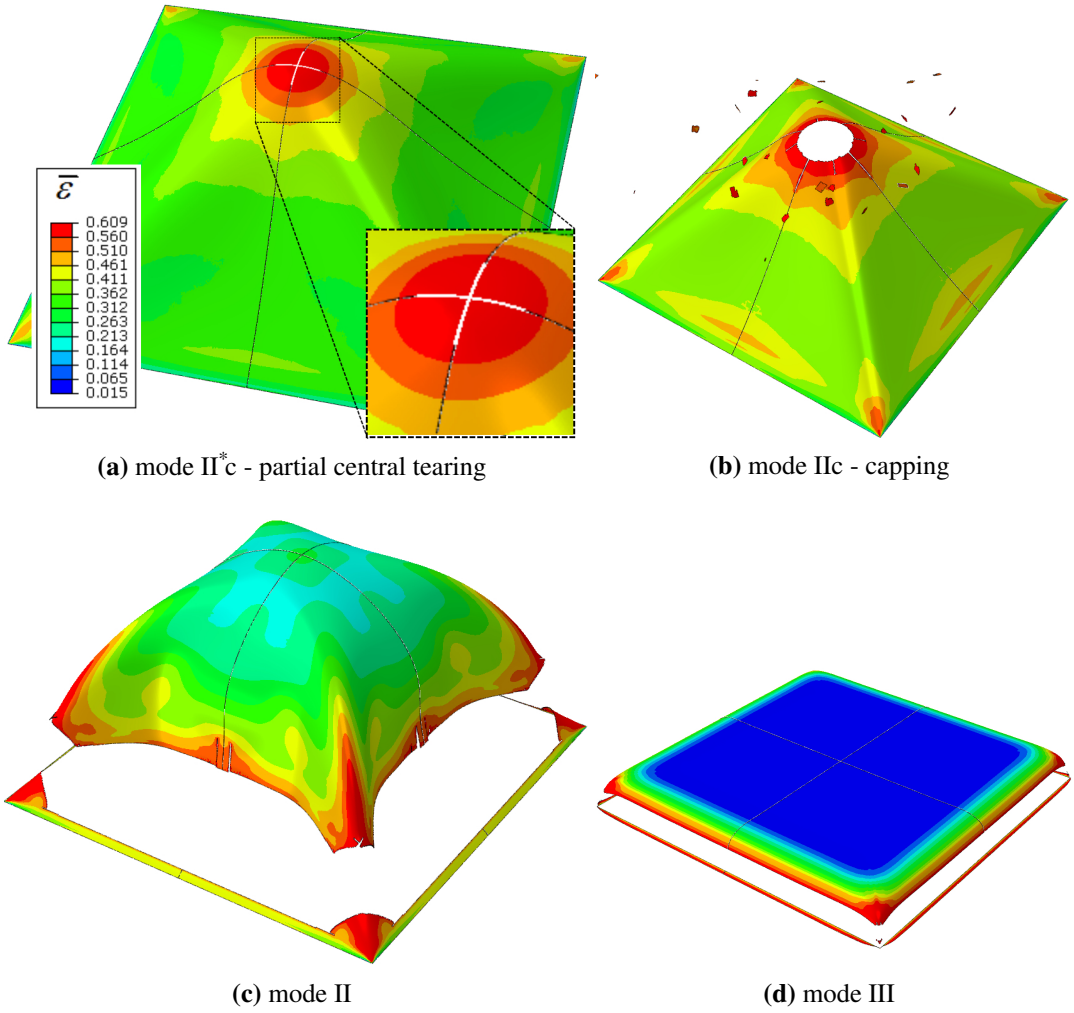

(a) mode II*c - partial central tearing

(b) mode IIc - capping

(c) mode II

(d) mode III

Figure 6.11: Failure modes of simply-supported square plates. Contour plots of true plastic strain $\bar{\varepsilon}$ are used to highlight regions of maximum strain, where failure occurs.

knowledge, this failure mode has not been described previously in the literature and will be here referred to as mode IIr or 'ripping'. In the range of impulses where mode IIr is observed, partial or complete detachment can be encountered, depending on whether the crack stops in its propagation.

At higher I^*, mode IIr is followed by modes II and III, where rupture occurs simultaneously on four paths parallel to the plate edges. It is observed that the distance of the crack path from the support is negligibly affected by the aspect ratio γ and the impulse intensity. One distinguishing feature of the detachment path for simply-supported plates consists in the multiple ramifications that form along the tears, compared to the straight fracture without ramifications that characterises the

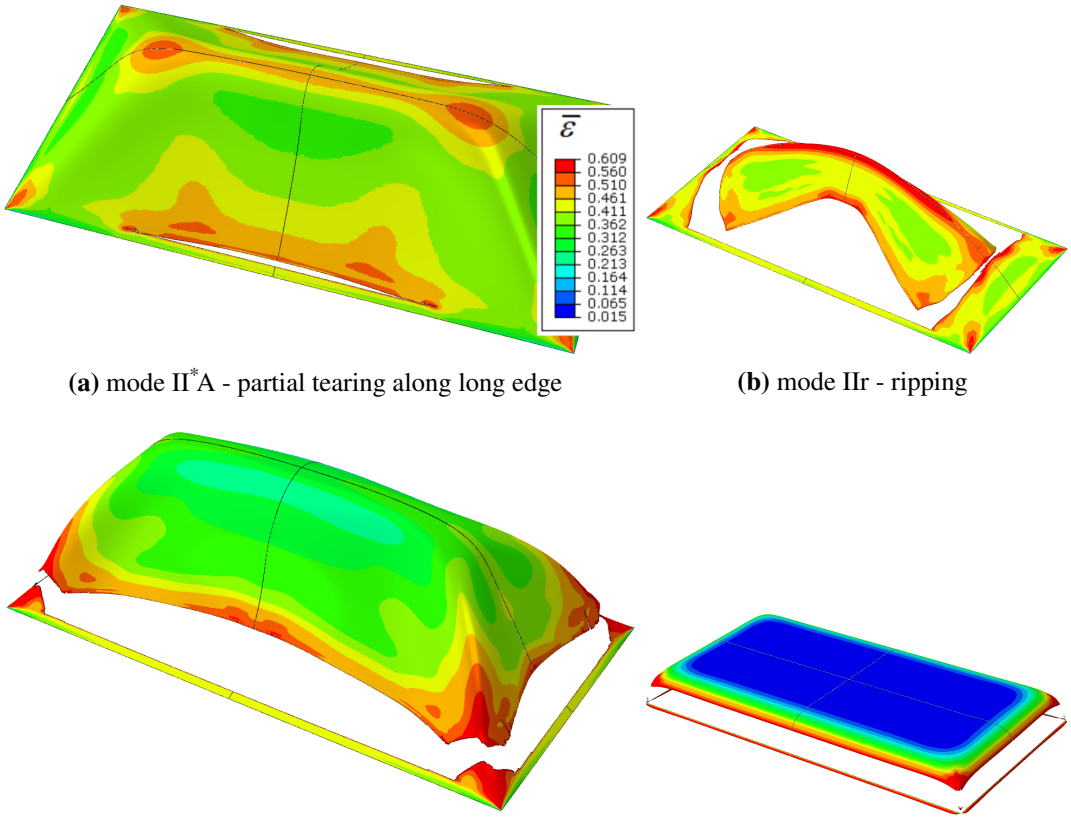

(a) mode II*A - partial tearing along long edge

(b) mode IIr - ripping

(c) mode II

(d) mode III

Figure 6.12: Failure modes of simply-supported rectangular plates with $\gamma = 2$. Contour plots of true plastic strain $\bar{\varepsilon}$ are used to highlight regions of maximum strain, where failure occurs [68].

fully-constrained plates.

The measured dimensionless central deflection W/H and the sequences of failure modes are reported in Figure 6.13. It is observed that the increased mobility of the boundaries reduces the strain in the peripheral regions, and mode I occurs in a wider range of impulses, compared to fully-constrained plates. Consistently with previous studies, deviation from linearity coincides with the initiation of rupture mechanisms: mode II*c for square plates (Figure 6.13a), and mode II*A for rectangular plates (Figure 6.13b). Peak values of deflection are always reached at the onset of mode II, followed by a rapid drop at higher impulses. Based on the criterion proposed on the crack propagation velocity, equation (5.20), the transition between mode II and III occurs at impulses higher than $I^* = 3.5$, although the horizontal asymptote typical of fully-constrained plates was not observed in the range

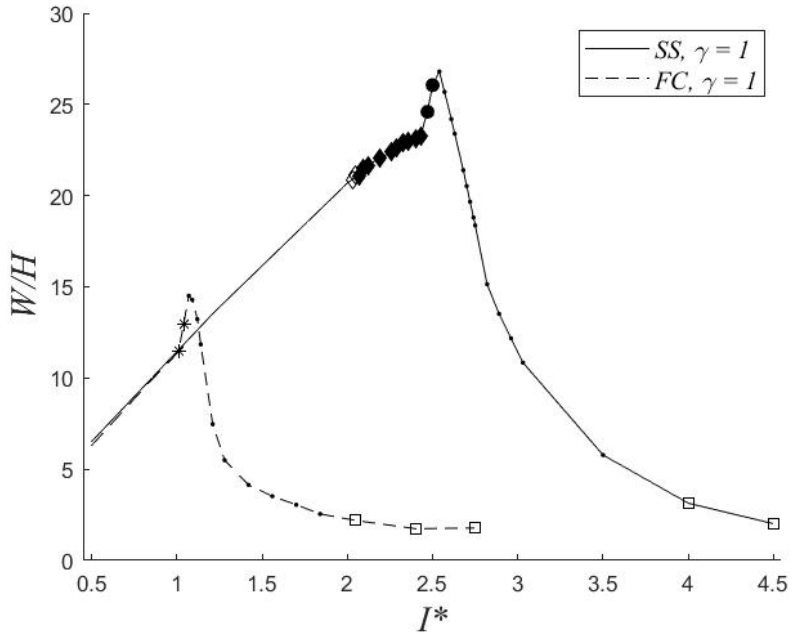

(a) Square plates

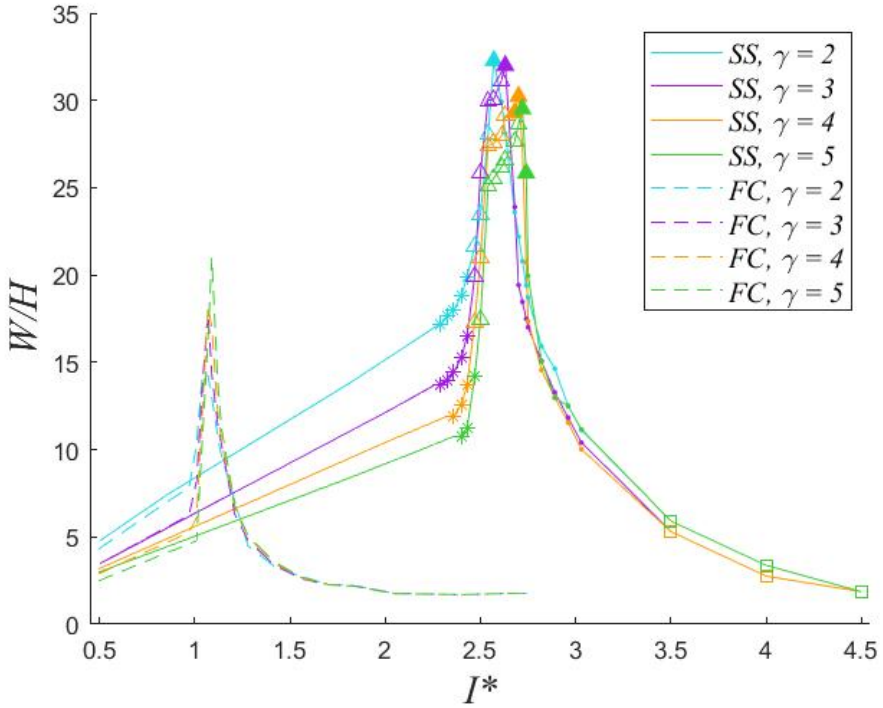

(b) Rectangular plates

Figure 6.13: Comparison of dimensionless deflection W/H for plates with simply supported (SS) or fully-constrained (FC) boundary conditions: (a) square plates and (b) rectangular plates. Symbols are used to highlight failure modes as follows: ✳ mode II*, • mode II and □ mode III; (a) ◇ mode II*c, ◆ mode IIc - capping and ● interposition of capping and mode II; (b) mode II*A and mode IIr with △ partial ripping and ▲ complete ripping [68].

of impulses analysed.

The measurements of tear lengths T_A for rectangular plates from this study is reported in the failure map of Figure 6.14. Analogously to the fully-constrained plates, the greatest variation of T_A occurs in the impulse range of mode II*. The variation of T_A increases slowly with the impulse in the ranges of mode II and III. Furthermore, even for simply-supported rectangular plates it was observed that $a \approx b$ and that $T_A/T_B \approx \gamma$, for any value of γ and I^*.

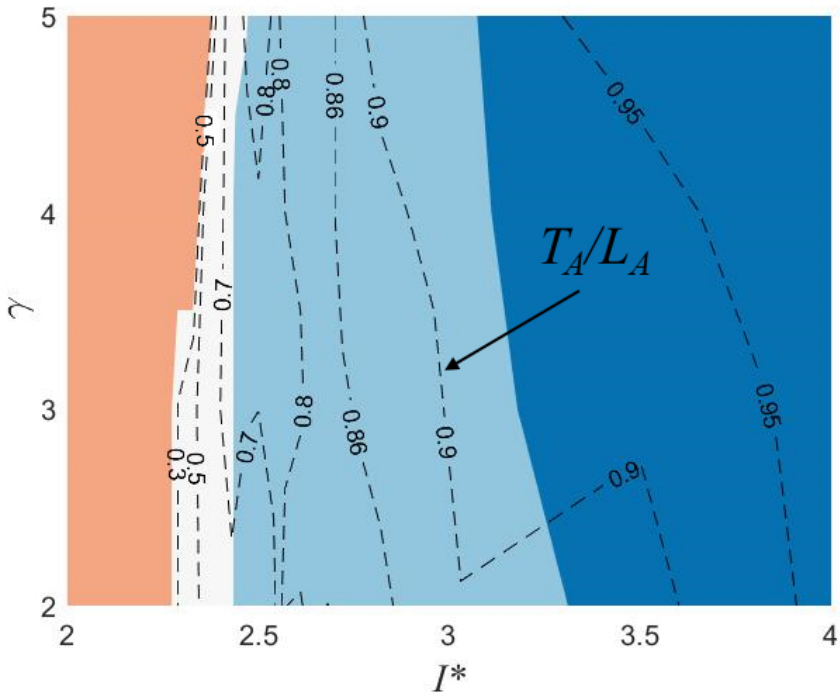

Figure 6.14: Dimensionless tear length T_A/L_A failure map for simply-supported rectangular plates. Different colours identify failure mode I, mode II*A, mode II and IIr, and mode III.

6.6 Summary

The numerical model established in Chapter 5 has been employed in the prediction of the dynamic response of quadrangular plates with fully-constrained or simply-supported boundary conditions. The new results indicate that simply-supported plates subjected to uniform blast loading display failure modes that are different from those of fully-clamped panels. The observed behaviour is similar to that of plates subject to localised blast, with the development of a non-uniform deforma-

tion profile and ‘capping’ failure [58, 61]. In addition, a previously unobserved ‘ripping’ failure mode has been discovered numerically for simply-supported rectangular plates, where detachment occurs due to the joining of crack paths propagating from opposite sides, rather than from contiguous edges.

Finally, dimensionless failure maps have been developed, elucidating the influence of plate topology, boundary conditions and amount of material on the inelastic response. The maps represent a valid aid in the design of impulsively loaded plates since they indicate the correlation between failure modes, the tear length and the residual lengths, and the maximum expected deformation as a function of the impulse intensity.

Chapter 7

Conclusions and future research

7.1 Conclusions

Numerical analyses offer an invaluable tool for solving engineering problems. Thanks to the capability to predict the behaviour of materials and structures, finite element models are useful in the study of problems involving structural failure. The research work discussed in this thesis presents the development and validation of two FE models for investigating the mechanical behaviour of thin-walled pipes and plates undergoing large deformation and failure under dynamic loading conditions.

Firstly, a beam element code was developed to study the response of pressurised pipes deforming in a whip-like motion under the influence of an intense force generated by the escape of fluids following a sudden guillotine break. The element employs a corotational kinematic formulation to obtain a low computational cost, and a constitutive relationship that idealises the cross-sectional collapse mechanisms of tubes in bending.

Secondly, a shell element model was developed to investigate the failure modes of steel plates hit by explosive blasts. The model employs comprehensive constitutive laws to capture accurately the damage mechanisms of metal components due to ductile and shear failure. A thorough approach was followed, combining numerical analyses with experimental tests (tensile and shear tests on steel specimens, grade S235), to achieve mesh insensitivity of the damage mechanisms. The main findings from these two investigations are summarised below.

Moment-curvature master curves for pipes

In Chapter 2 numerical tests of pipes in bending were performed to obtain moment-curvature relations for steel pipes with various combinations of external diameters and wall thickness. The simulations had the scope of identifying for each combination the values of bending moment and curvature corresponding to the initiation of cross-sectional collapse, which were necessary for developing a comprehensive constitutive law for pipe whips. Through a dimensional analysis, it was found that the M-k relations obtained were completely identified by three dimensionless groups of equation (2.31):

$$\pi_1 = \frac{D}{H},$$

$$\pi_2 = \frac{M_c}{\sigma_Y H D^2},$$

$$\pi_3 = \frac{k_c D^2}{H}.$$

The group π_1 allows to distinguish between relatively thick $D/H < 20$ and thin $D/H > 20$ pipes. The groups π_2 and π_3 allow to manipulate the M-k relations, obtaining two dimensionless master curves, unique for thick and thin pipes, reported in Section 2.5. These findings, which shed new light in understanding the flexural behaviour of thin-walled structural elements, has no prior mentions in the literature. Thanks to their simplicity, the master curves and the dimensionless groups hold a great potential for any future study aimed at analysing the response of pipes in bending. Future studies should be considered to analyse members with different profiles (e.g. square tubing, I sections or T sections) and experimental bending tests should be performed for validation purposes.

Prediction of the hazard zone for pipe whips

In Chapter 3, the beam element code developed in Chapter 2 has been used to investigate the effect of cross-sectional dimensions and loading conditions on the collapse mechanism and on the extent of the hazard zone in pipe whips. The numerical

results, collected in dimensionless diagrams, have led to the development of phenomenological equations to predict the pipe behaviour. Equations (3.20) and (3.21), here reported,

$$\frac{1}{3} \leq \lambda_1^{\text{thick}} \leq \frac{\sqrt{3}}{2\pi},$$

$$\frac{1}{4} \leq \lambda_1^{\text{thin}} \leq \frac{\sqrt{2}}{2\pi},$$

allow to identify the initiation of self-intersecting collapse in thick and thin pipes, respectively. Their use in the design of a piping system would permit to predict if the pipes are likely to fail with this particularly hazardous mechanism. Equation (3.22)

$$\zeta = \frac{3}{f_0 - a_1 \gamma^{a_2}} + b_1 \gamma^{b_2}.$$

can be used to predict the hazard zone of pipe whips bearing a heavy flange on the free end, whereas equation (3.5)

$$Z = \frac{3M_P}{F_0} = \frac{3M_P}{c_T P_0 A},$$

requires the knowledge of the cross-sectional dimensions, the fluid pressure and the strength of the pipe material to predict the hazard zone of pipe whips. These equations, together with the diagrams developed in Chapter 3, are useful assets in the design of piping systems.

Computational efficiency of corotational elements

The simulations performed in the Chapters from 2 to 4 employ element codes here developed in the corotational framework. Simulations employing the VUEL BM2D code for the simulation of in-plane pipe whips had a significantly increased computational speed (up to 88 times faster) than analogous simulations employing shell elements, without sacrificing any accuracy.

Simulations using the VUEL BM3D code, developed for the simulation of out-of-plane pipe whips, proved to be only 5 times faster than their shell element

analogous. However, the VUEL BM3D element presents still noticeable improvements when compared to traditional beam elements, and the optimisation of the code subroutines offers the potential to achieve smaller computational costs.

Plates failure mode II-III threshold

As discussed in Chapter 5, despite the numerous efforts made in previous research works, the physical phenomenon leading to the transition between failure modes II and III in impulsively loaded metal plates is still poorly understood. Analysing our numerical predictions, we believe that the transition point can be identified by comparing the crack propagation speed with the propagation velocity of pressure waves in the plate. Predictions based on this criterion are in close agreement with the limited experimental observations available, and further investigations are recommended, employing digital image correlation techniques to monitor in detail the crack growth.

Ripping failure modes of plates

In Chapter 6, the numerical investigation on simply-supported rectangular plates has led to the discovery of a previously unobserved failure mode, named 'ripping', where fracture initiates at the centre point of the longer sides, but then propagates toward the interior of the plate, rather than along the supports. This phenomenon has no precedent in the literature, and further experimental studies are required to verify this novel finding, with the combinations of loading intensity and plate topology suggested by the dimensionless diagrams presented.

7.2 Future research

The research work presented in this thesis has addressed several aspects of the investigation of the modes of deformation and failure of pipe whips and impulsively loaded plates, leading to advancements in their modelling techniques. During the research, some aspects were identified worthy of further investigation, paving the way to future research works as follows:

1. **Force pulse subroutine for pipes** — Simulations using the VUEL BM2D

and VUEL BM3D element codes employed a pre-determined pulse shape to model the dynamic load generated by the escape of pressurised fluids in pipe whips. Experimental evidence suggests that the intensity of the load pulse is tightly connected to the deformation of the pipe, and that the loading reduces drastically when the cross-section collapses. Therefore, a natural improvement to the element code would be the development of a force pulse subroutine where the transient load intensity is determined by the current inner area of the cross-section, which in turn is a function of the curvature.

2. **Interactive yield surface for pipes** — The completion of the VUEL BM3D code requires the implementation of a more realistic constitutive model for torsion and an interactive yield surface between axial forces, bending moment and twisting moment. Numerical studies have shown that the deformation of in-plane pipe whips has a negligible dependence on the strain rate. Similar conclusion in the case of out-of-plane pipe whips have yet to be reached, and we anticipate that the rate of deformation might greatly influence the pipe response when simultaneous tension, bending and twisting occur, due to the well-known sensibility of the tensile strength to the strain rate.

3. **Damage model for plates** — Despite its numerous features, the damage model employed in the simulation of plates makes several simplifying assumptions, for example neglecting the dependence of damage initiation on the Lode angle [72], the decrease in plasticity at high strain rate, and the effect of the heat generated by the explosion. More comprehensive versions of the MMC criterion exist, which take into account the Lode angle [82], requiring the execution of tensile and shear test of specimens with varying thickness. Furthermore, performing experiments at different strain rate is necessary to successfully incorporate this phenomenon in the material model.

4. **Blast experiments on plates** — As previously discussed, repeating the experiments on blast loaded plates while measuring the crack propagation velocity (for example using novel digital image correlation techniques) is necessary

to completely verify the soundness of the criterion here developed to identify the mode II-III threshold. Moreover, new experimental investigations are required to confirm the discovery of the 'ripping' failure mode predicted numerically for simply-supported rectangular plates for certain combinations of loading and topology.

Appendix A

Kinematic hardening subroutine for VUEL BM2D and BM3D

Subroutine for the kinematic hardening constitutive model employed in the VUEL BM2D and VUEL BM3D element codes for the analysis of pipe whips. In the application of the plastic model $\bar{\sigma}^H$, the conversion between nominal and plastic quantities through (2.26) is implied.

```
% initialise
σ_max = 0,  ε_max = 0,  σ_0 = 0
if sign(ε)(ε − ε_max) ≥ 0
% evaluate
σ* = Eε
if |σ*| − σ_Y ≤ 0 % elastic loading
σ = σ*
else % plastic loading
σ̄ = σ̄^H(ε̄)
end
% update
σ_max = σ,  ε_max = ε
else
% evaluate
σ* = σ_max + E(ε − ε_max)
```

$\sigma_{-Y} = |\sigma_{\max} - 2\mathtt{sign}(\varepsilon)\sigma_Y|$

`if` $|\sigma^* - \sigma_{\max}| - |\sigma_{\max}| - \sigma_{-Y} \leq 0$ `% elastic unloading`

$\sigma = \sigma^*$

`else % kinematic plasticity`

$\varepsilon_0 = \varepsilon_{\max} - \mathtt{sign}(\varepsilon)\varepsilon_Y$

$\sigma_0 = \sigma_{\max} + E(\varepsilon_0 - \varepsilon_{\max})$

$\bar{\sigma} = \bar{\sigma}_0 + \sigma^H(\bar{\varepsilon} - \bar{\varepsilon}_0)$

`end`

`end`

Appendix B

Moment-curvature subroutine for VUEL BM2D and BM3D

Subroutine for the hardening-softening moment-curvature (M-K) constitutive model employed in the VUEL BM2D and VUEL BM3D element codes for the analysis of pipe whips.

```
% initialise
M_max = 0,  k_max = 0,  M_0 = 0
if sign(k)(k − k_max) ≥ 0
% evaluate
M* = EIk
if |M*| − M_Y ≤ 0 % elastic loading
M = M*
else % plastic loading
M = M^HS(k)
end
% update
M_max = M,  k_max = k
else
% evaluate
M* = M_max + EI(k − k_max)
M_−Y = |M_max − 2sign(k)M_Y|
```

```
if  |M* − M_max| − |M_max| − M_−Y ≤ 0 % elastic unloading
M = M*
else % kinematic plasticity
k_0 = k_max − sign(k) k_Y
M_0 = M_max + EI(k_0 − k_max)
M = M_0 + M^HS (k − k_0)
end
end
```

Appendix C

Torsional subroutine for VUEL BM3D

Subroutine for the torsional constitutive model employed in the VUEL BM3D element code for the analysis of pipe whips.

```
% initialise
T_max = 0,  k_max = 0
if sign(k_1)(k_1 − k_max) ≥ 0
% evaluate
T* = GI_p k_1
if |T*| − T_p ≤ 0 % elastic loading
T = T*
else % plastic loading
T = T^H
end
% update
T_max = M,  k_max = K
else
% evaluate
T* = T_max + GI_p(k_1 − k_max)
T_−p = |T_max − 2T^p|
if  |T* − T_max| − 2T_p| ≤ 0 % elastic unloading
```

$T = T^*$

`else % kinematic plasticity`

$k_0 = k_{\max} - \mathtt{sign}(k_1) k_p$

$T_0 = T_{\max} + GI_p(k_0 - k_{\max})$

$T = \mathtt{sign}(k_1 - k_0)\,(T_0 + G_U I_p |k_1 - k_0|)$

`end`

`end`

Bibliography

[1] G. Lu, T. Yu. *Energy Absorption of Structures and Materials*. CRC Press, nov 2003.

[2] S. R. Reid, T. X. Yu, J. L. Yang, G. G. Corbett. Dynamic elastic-plastic behaviour of whipping pipes: Experiments and theoretical model. *Int. J. Impact Eng.*, 18(7-8):703–733, oct 1996.

[3] X. Luo, W. Du, C. Wang, C. Liu, J. Yang, P. Li, J. Zhang. Experimental study of u-bolt pipe whip restraint: Deformation process and energy absorbing. In *ASME Int. Mech. Eng. Congr. Expo. Proc.*, volume 14-2015, page V014T08A007. ASME, nov 2015.

[4] A. R. Telford. Impact assessment in the UK nuclear power industry: An overview of the R3 impact assessment procedure. *Int. J. Press. Vessel. Pip.*, 87(9):520–529, 2010.

[5] K. Fullard, D. Thomas, S. Wicks. The R3 impact assessment procedure for nuclear power plant structures. In *Trans. SMiRT 11 Conf.*, volume J05, pages 81–86, 1991.

[6] D. S. Queener. Reports, standards, and safety guides. *Nucl. Saf.*, 37(4):391–395, 1996.

[7] M. R. Baum. The rupture of high pressure pipework: The influence of pipeline geometry on in-plane pipewhip. *J. Loss Prev. Process Ind.*, 9(2):147–159, 1996.

[8] W. J. Stronge, T. Yu. *Dynamic Models for Structural Plasticity*. Springer London, London, 1993.

[9] S. R. Reid, B. Wang. Large-deflection analysis of whipping pipes. I: Rigid, perfectly-plastic model. *J. Eng. Mech.*, 121(8):881–887, aug 1995.

[10] S. R. Reid, T. Yu, J. L. Yang. Response of an elastic, plastic tubular cantilever beam subjected to a force pulse at its tip-Small deflection analysis. *Int. J. Solids Struct.*, 32(23):3407–3421, dec 1995.

[11] S. R. Reid, B. Wang, M. Aleyaasin. Structural modelling and testing of failed high energy pipe runs: 2D and 3D pipe whip. *Int. J. Press. Vessel. Pip.*, 88 (5-7):189–197, 2011.

[12] I. Micheli, P. Zanaboni. An Analytical Validation of Simplified Methods for the Assessment of Pipe Whip Characteristics. In *Trans. 17th Int. Conf. Struct. Mech. React. Technol. (SMiRT 17)*, pages 1–8, 2003.

[13] S. R. Reid, M. Aleyaasin, B. Wang. Out-of-plane pipe whip for a bent cantilever pipe: Comparison between experiment and FEM models. *J. Appl. Mech. Trans. ASME*, 79(1):011005, 2012.

[14] S. R. Reid, Y. L. Hua, J. L. Yang. Development of double hinge mechanisms in a bent cantilever subjected to an out-of-plane force pulse. *Int. J. Impact Eng.*, 9(4):485–502, jan 1990.

[15] S. R. Reid, B. Wang, Y. L. Hua. Triple plastic hinge mechanism for a bent cantilever beam subjected to an out-of-plane tip force pulse of finite duration. *Int. J. Impact Eng.*, 16(1):75–93, 1995.

[16] 3DS Dassault Systèmes. *SIMULIA Abaqus 2017 Documentation*. Dassault Systèmes, Providence, RI, 2016.

[17] L. Zeng, L. G. Jansson, Y. Venev. On Pipe Elbow Elements in ABAQUS and Benchmark Tests. In *Proc. ASME 2014 Press. Vessel. Pip. Conf.*, number 10. American Society of Mechanical Engineers, jul 2014.

[18] S. R. Reid, T. Yu, J. L. Yang. Hardening-softening behaviour of circular pipes under bending and tension. *Int. J. Mech. Sci.*, 36(12):1073–1085, dec 1994.

[19] Y. Jialing, S. R. Reid. Approximate estimation of hardening-softening behaviour of circular pipes subjected to pure bending. *Acta Mech. Sin.*, 13(3): 227–240, aug 1997.

[20] T. Wierzbicki, M. V. Sinmao. A simplified model of Brazier effect in plastic bending of cylindrical tubes. *Int. J. Press. Vessel. Pip.*, 71(1):19–28, apr 1997.

[21] S. R. Reid, J. L. Yang. Pipe Whip: In-Plane Whipping of Bent Cantilever Pipes. *J. Press. Vessel Technol.*, 120(2):170, 1998.

[22] C. A. Felippa, B. Haugen. A unified formulation of small-strain corotational finite elements: I. Theory. *Comput. Methods Appl. Mech. Eng.*, 194(21-24 SPEC. ISS.):2285–2335, jun 2005.

[23] T. Belytschko, B. J. Hsieh. Non-linear transient finite element analysis with convected co-ordinates. *Int. J. Numer. Methods Eng.*, 7(3):255–271, 1973.

[24] T. Belytschko, L. W. Glaum. Applications of higher order corotational stretch theories to nonlinear finite element analysis. *Comput. Struct.*, 10(1-2):175–182, 1979.

[25] M. A. Crisfield. A consistent co-rotational formulation for non-linear, three-dimensional, beam-elements. *Comput. Methods Appl. Mech. Eng.*, 81(2):131–150, aug 1990.

[26] M. A. Crisfield, G. F. Moita. A unified co-rotational framework for solids, shells and beams. *Int. J. Solids Struct.*, 33(20-22):2969–2992, aug 1996.

[27] J.-M. Battini. *Co-rotational beam elements in instability problems*. PhD thesis, KTH Royal Institute of Technology, Stockholm, Sweden, 2002.

[28] J.-M. Battini, C. Pacoste. Plastic instability of beam structures using co-rotational elements. *Comput. Methods Appl. Mech. Eng.*, 191(51-52):5811–5831, dec 2002.

[29] M. A. Crisfield, U. Galvanetto, G. Jeleni? Dynamics of 3-D co-rotational beams. *Comput. Mech.*, 20(6):507–519, nov 1997.

[30] J. C. Simo. A finite strain beam formulation. the three-dimensional dynamic problem. part i. *Computer methods in applied mechanics and engineering*, 49 (1):55–70, 1985.

[31] M. Crisfield, J. Shi. A co-rotational element/time-integration strategy for non-linear dynamics. *International Journal for Numerical Methods in Engineering*, 37(11):1897–1913, 1994.

[32] U. Galvanetto, M. Crisfield. An energy-conserving co-rotational procedure for the dynamics of planar beam structures. *International journal for numerical methods in engineering*, 39(13):2265–2282, 1996.

[33] T.-N. Le. *Nonlinear dynamics of flexible structures using corotational beam elements*. PhD thesis, KTH Royal Institute of Technology, Stockholm, Sweden, 2013.

[34] T.-N. Le, J.-M. Battini, M. Hjiaj. Efficient formulation for dynamics of corotational 2D beams. *Comput. Mech.*, 48(2):153–161, aug 2011.

[35] T.-N. Le, J.-M. Battini, M. Hjiaj. A consistent 3D corotational beam element for nonlinear dynamic analysis of flexible structures. *Comput. Methods Appl. Mech. Eng.*, 269:538–565, 2014.

[36] R. Alsafadie, M. Hjiaj, J.-M. Battini. Corotational mixed finite element formulation for thin-walled beams with generic cross-section. *Comput. Methods Appl. Mech. Eng.*, 199(49-52):3197–3212, dec 2010.

[37] R. Alsafadie, J.-M. Battini, M. Hjiaj. Efficient local formulation for elasto-plastic corotational thin-walled beams. *Int. J. Numer. Method. Biomed. Eng.*, 27(4):498–509, apr 2011.

[38] R. Alsafadie, M. Hjiaj, H. Somja, J.-M. Battini. A comparative study of displacement and mixed-based corotational finite element formulations for

elasto-plastic three-dimensional beam analysis. *Eng. Comput.*, 28(7):939–982, oct 2011.

[39] R. Alsafadie, J.-M. Battini, H. Somja, M. Hjiaj. Local formulation for elasto-plastic corotational thin-walled beams based on higher-order curvature terms. *Finite Elem. Anal. Des.*, 47(2):119–128, feb 2011.

[40] R. Alsafadie, M. Hjiaj, J.-M. Battini. Three-dimensional formulation of a mixed corotational thin-walled beam element incorporating shear and warping deformation. *Thin-Walled Struct.*, 49(4):523–533, apr 2011.

[41] P. Areias, J. Garção, E. B. Pires, J. I. Barbosa. Exact corotational shell for finite strains and fracture. *Comput. Mech.*, 48(4):385–406, oct 2011.

[42] V. Longva. *Formulation and Application of Finite Element Techniques for Slender Marine Structures Subjected to Contact Interactions*. PhD thesis, Norvegian University of Scinece and Technology, 2015.

[43] L. L. Yaw. Co-rotational Meshfree Formulation For Large Deformation Inelastic Analysis Of Two-Dimensional Structural Systems. Technical report, 1992.

[44] L. L. Yaw, N. Sukumar, S. K. Kunnath. Meshfree co-rotational formulation for two-dimensional continua. *Int. J. Numer. Methods Eng.*, 79(8):979–1003, aug 2009.

[45] E. G. Parker, J. F. O'Brien. Real-time deformation and fracture in a game environment. *Proc. 2009 ACM SIGGRAPH/Eurographics Symp. Comput. Animat. - SCA '09*, page 165, 2009.

[46] H. Courtecuisse, H. Jung, J. Allard, C. Duriez, D. Y. Lee, S. Cotin. GPU-based real-time soft tissue deformation with cutting and haptic feedback. *Prog. Biophys. Mol. Biol.*, 103(2-3):159–168, dec 2010.

[47] N. Jones. *Structural Impact*. Cambridge University Press, Cambridge, 1990.

[48] C. Yong, Y. Wang, P. Tang, H. X. Hua. Impact characteristics of stiffened plates penetrated by sub-ordnance velocity projectiles. *J. Constr. Steel Res.*, 64(6):634–643, 2008.

[49] J. N. Marinatos, M. S. Samuelides. Towards a unified methodology for the simulation of rupture in collision and grounding of ships. *Mar. Struct.*, 42: 1–32, jul 2015.

[50] B. C. Cerik. Damage assessment of marine grade aluminium alloy-plated structures due to air blast and explosive loads. *Thin-Walled Struct.*, 110 (October 2016):123–132, 2017.

[51] R. G. Teeling-Smith, G. N. Nurick. The deformation and tearing of thin circular plates subjected to impulsive loads. *Int. J. Impact Eng.*, 11(1):77–91, jan 1991.

[52] S. Yuen, G. N. Nurick, G. S. Langdon, Y. Iyer. Deformation of thin plates subjected to impulsive load: Part III – an update 25 years on. *Int. J. Impact Eng.*, 107:1339–1351, sep 2017.

[53] G. N. Nurick, J. B. Martin. Deformation of thin plates subjected to impulsive loading-A review. Part I: Theoretical considerations. *Int. J. Impact Eng.*, 8(2): 159–170, jan 1989.

[54] G. N. Nurick, M. D. Olson, J. R. Fagnan, A. Levin. Deformation and tearing of blast-loaded stiffened square plates. *Int. J. Impact Eng.*, 16(2):273–291, 1995.

[55] G. N. Nurick, G. C. Shave. The deformation and tearing of thin square plates subjected to impulsive loads - An experimental study. *Int. J. Impact Eng.*, 18 (1):99–116, jan 1996.

[56] M. D. Olson, G. N. Nurick, J. R. Fagnan. Deformation and rupture of blast loaded square plates-predictions and experiments. *Int. J. Impact Eng.*, 13(2): 279–291, jan 1993.

[57] D. Bonorchis, G. N. Nurick. The effect of welded boundaries on the response of rectangular hot-rolled mild steel plates subjected to localised blast loading. *Int. J. Impact Eng.*, 34(11):1729–1738, nov 2007.

[58] N. Jacob, G. N. Nurick, G. S. Langdon. The effect of stand-off distance on the failure of fully clamped circular mild steel plates subjected to blast loads. *Eng. Struct.*, 29(10):2723–2736, oct 2007.

[59] K. Ramajeyathilagam, C. Vendhan. Deformation and rupture of thin rectangular plates subjected to underwater shock. *Int. J. Impact Eng.*, 30(6):699–719, jul 2004.

[60] B. M. Thomas. *The effect of boundary conditions on the failure of thin plates subjected to impulsive loading*. PhD thesis, University of Cape Town, 1995.

[61] G. S. Langdon, S. C. K. Yuen, G. N. Nurick. Experimental and numerical studies on the response of quadrangular stiffened plates. Part II: Localised blast loading. *Int. J. Impact Eng.*, 31(1):85–111, jan 2005.

[62] N. S. Rudrapatna, R. Vaziri, M. D. Olson. Deformation and failure of blast-loaded stiffened plates. *Int. J. Impact Eng.*, 24(5):457–474, 2000.

[63] V. Aune, E. Fagerholt, K. O. Hauge, M. Langseth, T. Børvik. Experimental study on the response of thin aluminium and steel plates subjected to airblast loading. *Int. J. Impact Eng.*, 90:106–121, apr 2016.

[64] V. Aune, G. Valsamos, F. Casadei, M. Larcher, M. Langseth, T. Børvik. Numerical study on the structural response of blast-loaded thin aluminium and steel plates. *Int. J. Impact Eng.*, 99:131–144, jan 2017.

[65] N. Jones. Dynamic inelastic response of strain rate sensitive ductile plates due to large impact, dynamic pressure and explosive loadings. *Int. J. Impact Eng.*, 74:3–15, dec 2014.

[66] T. Mirzababaie Mostofi, H. Babaei, M. Alitavoli. Theoretical analysis on the effect of uniform and localized impulsive loading on the dynamic plastic behaviour of fully clamped thin quadrangular plates. *Thin-Walled Struct.*, 109: 367–376, dec 2016.

[67] T. Mirzababaie Mostofi, A. Golbaf, A. Mahmoudi, M. Alitavoli, H. Babaei. Closed-form analytical analysis on the effect of coupled membrane and bending strains on the dynamic plastic behaviour of fully clamped thin quadrangular plates due to uniform and localized impulsive loading. *Thin-Walled Struct.*, 123:48–56, feb 2018.

[68] D. Schiano Moriello, F. Bosi, R. Torii, P. Tan. Failure and detachment path of impulsively loaded plates. *Thin-Walled Struct.*, 155:106871, oct 2020.

[69] N. S. Rudrapatna, R. Vaziri, M. D. Olson. Deformation and failure of blast-loaded square plates. *Int. J. Impact Eng.*, 22(4):449–467, 1999.

[70] Y. Yuan, P. Tan. Deformation and failure of rectangular plates subjected to impulsive loadings. *Int. J. Impact Eng.*, 59:46–59, sep 2013.

[71] V. Aune, G. Valsamos, F. Casadei, M. Langseth, T. Børvik. On the dynamic response of blast-loaded steel plates with and without pre-formed holes. *Int. J. Impact Eng.*, 108:27–46, 2017.

[72] Y. Bai, T. Wierzbicki. Application of extended Mohr-Coulomb criterion to ductile fracture. *Int. J. Fract.*, 161(1):1–20, jan 2010.

[73] M. Pavlović, Z. Marković, M. Veljković, D. Bucrossed D Signevac. Bolted shear connectors vs. headed studs behaviour in push-out tests. *J. Constr. Steel Res.*, 88:134–149, 2013.

[74] M. Imachi, S. Tanaka, T. Q. Bui, S. Oterkus, E. Oterkus. A computational approach based on ordinary state-based peridynamics with new transition bond for dynamic fracture analysis. *Eng. Fract. Mech.*, 206:359–374, feb 2019.

[75] T. H. Nguyen, T. Q. Bui, S. Hirose. Smoothing gradient damage model with evolving anisotropic nonlocal interactions tailored to low-order finite elements. *Comput. Methods Appl. Mech. Eng.*, 328:498–541, jan 2018.

[76] C. T. Wu, T. Q. Bui, Y. Wu, T. L. Luo, M. Wang, C. C. Liao, P. Y. Chen, Y. S. Lai. Numerical and experimental validation of a particle Galerkin method for metal grinding simulation. *Comput. Mech.*, 61(3):365–383, mar 2018.

[77] R. M. Brannon. Frame indifference. In *Rotation, Reflection, and Frame Changes*, 2053-2563, pages 19–1 to 19–49. IOP Publishing, 2018.

[78] N. Y. Gnedin, V. A. Semenov, A. V. Kravtsov. Enforcing the Courant–Friedrichs–Lewy condition in explicitly conservative local time stepping schemes. *J. Comput. Phys.*, 359:93–105, apr 2018.

[79] R. Courant, K. Friedrichs, H. Lewy. On the Partial Difference Equations of Mathematical Physics. *IBM J. Res. Dev.*, 11(2):215–234, mar 1967.

[80] N. K. Prinja, N. R. Chitkara. Finite-element analyses of post-collapse plastic bending of thick pipes. *Nucl. Eng. Des.*, 91(1):1–12, 1986.

[81] American Society of Mechanical Engineers. *Standard ASME B36. 19M-2004: Stainless Steel Pipe*. American Society of Mechanical Engineers, 2004.

[82] Y. Li, M. Luo, J. Gerlach, T. Wierzbicki. Prediction of shear-induced fracture in sheet metal forming. *J. Mater. Process. Technol.*, 210(14):1858–1869, nov 2010.

[83] M. Luo, T. Wierzbicki. Ductile fracture calibration and validation of anisotropic aluminum sheets. In *Soc. Exp. Mech. - SEM Annu. Conf. Expo. Exp. Appl. Mech. 2009*, volume 1, pages 302–312, 2009.

[84] M. Brünig, O. Chyra, D. Albrecht, L. Driemeier, M. Alves. A ductile damage criterion at various stress triaxialities. *Int. J. Plast.*, 24(10):1731–1755, oct 2008.

[85] S. Yan, X. Zhao. A fracture criterion for fracture simulation of ductile metals based on micro-mechanisms. *Theor. Appl. Fract. Mech.*, 95:127–142, jun 2018.

[86] L. Driemeier, M. Brünig, G. Micheli, M. Alves. Experiments on stress-triaxiality dependence of material behavior of aluminum alloys. *Mech. Mater.*, 42(2):207–217, feb 2010.

[87] A. C. Faralli. *Large deformation of T-stub connection in bolted steel joints*. PhD thesis, UCL (University College London), 2019.

[88] A. C. Faralli, P. Tan, G. J. McShane, P. Wrobel. Deformation Maps for Bolted T-Stubs. *J. Struct. Eng. (United States)*, 146(5), 2020.

[89] H. Hooputra, H. Gese, H. Dell, H. Werner. A comprehensive failure model for crashworthiness simulation of aluminium extrusions. *Int. J. Crashworthiness*, 9(5):449–464, sep 2004.

[90] N. Jones. A theoretical study of the dynamic plastic behavior of beams and plates with finite-deflections. *Int. J. Solids Struct.*, 7(8):1007–1029, 1971.

[91] T. Yu, F. L. Chen. The large deflection dynamic plastic response of rectangular plates. *Int. J. Impact Eng.*, 12(4):605–616, 1992.

[92] N. Mehreganian, L. A. Louca, G. S. Langdon, R. J. Curry, N. Abdul-Karim. The response of mild steel and armour steel plates to localised air-blast loading-comparison of numerical modelling techniques. *Int. J. Impact Eng.*, 115:81–93, may 2018.